DIRECTLY COMPRESSIBLE HYDROXYPROPYL METHYLCELLULOSE (HPMC) TO SUPPORT CONTINUOUS MANUFACTURING

By

CARL ALLENSPACH

A dissertation submitted to the
School of Graduate Studies
Rutgers, The State University of New Jersey
In partial fulfillment of the requirements
For the degree of
Doctor of Philosophy
Graduate Program in Pharmaceutical Sciences
Written under the direction of
Professor Tamara Minko, Ph.D
And approved by

New Brunswick, New Jersey

October 2020

ABSTRACT OF THE DISSERTATION

Directly Compressible Hydroxypropyl Methylcellulose (HPMC) to Support Continuous Manufacturing

By CARL THOMAS ALLENSPACH

Dissertation Director:
Professor Tamara Minko

This work was undertaken to evaluate a novel hydroxypropyl methylcellulose excipient used in the manufacture of hydrophilic matrix tablets for oral controlled release. This material was coprocessed with a small amount of silicon dioxide to provide improvements over the standard material and was shown to have better flow, compactability and less triboelectric charging demonstrating an improved performance in a loss-in-weight feeder. As a result, this material is preferred for use in continuous manufacturing via direct compression which would be problematic for the standard grade. Finally, a methodology was developed to calibrate the material properties for a computer simulation of the loss-in-weight feeder using the discrete element method which was shown to have good correlation with the experimental results.

ACKNOWLEDGEMENT AND DEDICATION

This work is dedicated to my loving family who have made this journey possible. To my parents, Mary and Tom Allenspach, who guided me through many challenges early in life and instilled the values that I hold dear to me even now. To my in-laws, Dorothy and William Traylor, whose joy of life makes our time together pass too quickly. To my beautiful daughters, Lauren and Natalie, who were small children when I started and have grown to be amazing young ladies who have already accomplished more than I could have hoped for them. I can't wait to see what they will do next. They have taught me many things along the way and I cherish our time together. Most importantly to my loving wife and best friend, Dr. Louise Traylor, whose constant encouragement and support made this possible. Her good nature, sense of adventure and strength to take on life with a positive attitude regardless of the significant challenges inspired me every day to accomplish as much as I could. It's not always the destination that is important, or the journey…sometimes it is who you travel with, and I couldn't have dreamed up a better companion.

This work would not have been possible without many people who have supported me over the years via close collaborations, challenging discussions, and research opportunities. Opening their equipment, laboratories, software, and sometimes even their homes and families. I have thoroughly enjoyed all of these interactions and experiences that have made this work both memorable and enjoyable. I am forever indebted to my respected advisor, Dr. Tamara Minko. Her support, encouragement, understanding and patience balanced with expectations made this possible. On two separate occasions she talked me out of giving up on the program and settling for less. She was always available for input and her attention to detail improved this work dramatically. She will always be an inspiration and role model for me in my career and in life.

I would like to thank my committee members, Dr. Tamara Minko, Dr. Guofeng You, Dr. Arash Hatefi, and Dr. Olga Garbuzenko for taking the time to provide their guidance.

I would like to thank my managers who have supported my efforts to complete this research while balancing a full time job. Dr. Sreekant Nadkarni who spent many hours in the lab teaching me about pharmaceutical equipment and processes which set the groundwork and gave me the confidence and responsibility to make many achievements in my career. Dr. Madhu Puddipeddi with whom I had many exciting scientific conversations that inspired me to keep learning. Dr. Colleen Ruegger, who helped me start the journey. When I told her I could be 50 years old before I finished, she replied “you will be 50 years old either way, do you want to be 50 with a PhD or not?” Dr. Erika Zannou who encouraged me to set challenging goals and work hard to achieve them, becoming a mentor and friend. Dr. Dafni Bika who opened many doors and showed me how to be an inspirational leader and make the most out of every situation. Dr. Amir Razaghi who taught me to look at all sides of a situation and make the most of out of life. I appreciate our friendship regardless of the miles. Brian Boland who has shown me that great achievements come from hard work and dedication. And my most recent manager, Neil Martin who helped me the most to balance my work so that I could finish what I started.

There were also many colleagues and collaborators to whom I owe thanks. Dr. Peter Timmins whose scientific understanding around HPMC was invaluable and whose mentorship has continued throughout this work. Gary D’Alonzo for the encouragement and paper reviews. Jeffrey Katz, Shasad Sharif and Steven Chan who supported some of the early characterization work. My co-authors who provided valuable input and critical reviews which improved the quality of this work: Geoffroy Lumay, James Holman, Anton Kulchitsky, Jerome Johnson, Dmytro Cherepakha.

In addition, this work could not have happened without access to materials and testing equipment. Tom Durig and Susan McHugh Lally at

Ashland provided the HPMC materials that were critical to this work. Filip Francqui at GranuTools provided access and training on their excellent powder characterization equipment. Jessica Zombek, Erica Anderson, Tyron Lunn and Andrew Berkmire at GEA supported the loss-in-weight feeder experiments which Richard Steiner and Joshua Egan were instrumental in arranging. Barbara Fretter and Rob Lammens at Solids Development Consultants (SDC) provided access to their advanced StylOne Compaction Simulator to aid the compression work. I appreciated their flexibility and welcoming me into their wonderful work and home environment. Jean LeFloch, whose contacts and connections helped me to find my way to Anton Kulchitsky, Jerome Johnson, and Dmytro Cherepakha at Coupi who supported me with the Polyphisica software and knowledge around the challenging DEM computer modeling work.

I would like to thank Rutgers University and the Department of Pharmaceutics at the Ernest Mario School of Pharmacy for providing the education and giving me the opportunity to do my PhD in the part-time program.

You are only limited by what you are willing to do.

Life is what you make of it, so make it the best you can.

TABLE OF CONTENTS

Contents

LIST OF TABLES

LIST OF FIGURES

INTRODUCTION

Hydroxypropyl methylcellulose (HPMC, hypromellose) is frequently utilized to create hydrophilic matrix tablets for modified release dosage forms. The popularity of these tablets is due to their simple formulation, good safety profile, reproducible release profiles, global acceptability, and cost effectiveness along with well understood diffusion and erosion mechanisms (1-4). Patients have benefited from having controlled release dosage forms by reducing the required dosing frequency since the drug is released over time which also improves patient compliance leading to more efficacious medicines. A clinical benefit with extended release dosage forms is the reduced peak plasma concentrations which can allow higher doses and sustained exposure while minimizing adverse safety events compared to immediate release (5-7).

HPMC has a long history of use in modified release tablets for almost 60 years (8) with significant research occurring early on (9-11). One of the greatest challenges with HPMC when used without being granulated is the poor flow due to the long, fiber like particle morphology (12). The poor flow of HPMC negatively impacts charging of materials, Loss-in-Weight (LIW) feeding, blending and compression weight variability. Recent material science advances for HPMC have resulted in co-processed materials which have improved flow and compactability. These direct compression (DC) HPMC materials were designed for direct compression and are better suited for use in the LIW feeders which is required for use in continuous manufacturing.

Continuous manufacturing is seeing an increased utilization in pharmaceutical manufacturing since the first product was approved in July 2015 (Orkambi®, Vertex Pharmaceuticals, Boston, USA). There have been a significant number of journal articles, books (13-16), and draft guidance from the FDA (17, 18) which encouraged many pharmaceutical companies to explore continuous manufacturing approaches (19). Development of continuous processes is well suited to the Quality by Design (QbD) approaches already being implemented and facilitated by the advances in Process Analytical Technology (PAT) for continuous monitoring of the product (20). Some of the advantages of continuous manufacturing include the following: reduced manual handling of materials (leading to improved safety and reduced human error), shorter processing times, improved efficiency, smaller physical footprint, eliminated need for process scale-up, and overall improved product quality (21, 22). One of the cornerstones of continuous manufacturing is the implementation of modeling approaches. Models can be used during operation to control the process, set limits on excursions, and determine if material needs to be diverted during excursions and for how long. Models can also be used during development to simulate the process providing additional knowledge into the process.

Process modeling of pharmaceutical processes via mechanistic models is advantageous as they capture the underlying physical phenomena through application of fundamental first principles of particles and surfaces such as mass, momentum and energy. They have been shown to have good predictability and are often preferred as they can provide additional scientific insight into modeled operations (23-25).

There are different approaches to modeling pharmaceutical processes including computational fluid dynamics (CFD), finite element method (FEM), discrete element method (DEM) and combinations of those being the most widely utilized (26). The discrete element method also referred historically as distinct element method, is not a new approach to simulate the motion and path of each particle. In fact, an early publication on a discrete numerical model for granular assemblies (27) which introduced DEM concepts, has been referenced over 16,000 times. It describes how motion and momentum are solved for each particle three dimensionally with normal and tangential contact forces included.

While DEM models are computationally intense they can provide more process insight compared to CFD models (24). Utilization of DEM has become significantly more valuable in recent years as computational speed has increased and modeling approaches become optimized. Research in this area has also increased with an increase in the number of journal publications in recent years. There are also a number of books dedicated to the subject of DEM and applications (28-34). Increased computer processing power has allowed for an increased number of particles to be simulated (35), improved commercially available software has made it easier to model processes. Novel calibration techniques (36) and the improved process and modeling understanding have led to more accurate results of the simulations. DEM in particular provides detailed information into granular flows allowing for increased process knowledge (37). Powder systems are typically represented by spherical particles to reduce the computational load and extrapolation of results to nonspherical particle systems is highly challenging (38, 39). For this reason an alternative approach to spheres was required for simulating the elongated HPMC particles.

LIW feeding has the potential to directly impact the homogeneity of the powder mixture resulting in potential impact to the content uniformity of the drug in the final dosage form (40-42) and as such it is considered a critical process in continuous manufacturing. This work will look at combining the challenging particle morphology and flow properties of HPMC into the first component of a continuous manufacturing line, the LIW feeder system, utilizing a DEM approach accounting for the nonspherical morphology of HPMC. The different aspects of this work include:

1) Characterization of three different standard HPMC grades and the equivalent three direct compression grades for particle properties including size, morphology, surface area, many techniques to evaluate powder flow and tablet compression studies.
2) Loss-in-weight feeder studies of the same six materials and additional characterization studies including triboelectrification, powder flow in a drum, angle of repose and bulk and tap density
3) Modeling of the LIW Feeder for HPMC
    a. Creation of a DEM model material that represents the HPMC K100M DC excipient with appropriate geometrical characteristics.
    b. Creation of DEM models for multiple characterization tests to facilitate calibration of the DEM material using measured data for HPMC.
    c. LIW feeder DEM simulations with different particle sizes, rates and amounts of material.

CHAPTER 1: CHARACTERIZATION OF A NOVEL HYDROXYPROPYL METHYLCELLULOSE (HPMC) DIRECT COMPRESSION GRADE EXCIPIENT

1 BACKGROUND

Controlled Release formulations continue to be of importance for oral drug delivery providing for customizable release of a drug over a predetermined time. A prolonged release allows for slower absorption of the drug, offering advantages over immediate release by reducing the maximum concentration of the drug (C_{max}) thereby reducing adverse side effects associated with high blood concentrations. Additionally, by extending times between doses it can also lead to improved patient compliance to dosing schedules resulting in improved overall efficacy (43). Instead of patients being required to remember to take multiple doses of a drug at various intervals throughout the day a single controlled release dose could be provided.

While there are many different types of delivery systems that can provide for controlled release oral dosing, hydrophilic matrix tablets are one of the most popular, representing more than 75% of modified release oral dosage forms (44) with those based on hydroxypropyl methylcellulose (hypromellose, HPMC) being one of the most widely used type of controlled release formulations (4, 45) and multiple books and book chapters are dedicated to the pharmaceutical use of HPMC (1, 46-50). This widespread use can be attributed to their global regulatory acceptance, utilization of common excipients and simple formulations, applicability to both high and low doses, good chemical compatibility, ease of development and standard manufacturing processes to create controlled release tablets (4, 51-53). The drug needs to be well distributed in the matrix tablet to ensure uniform and consistent release (54) and common processes such as direct compression, dry granulation / roller compaction, and wet granulation are typically utilized along with tablet compression and film coating.

More recently, cost pressures and competition within the pharmaceutical industry have resulted in the need for reduced development time and efficient manufacturing processes enabling short product manufacturing times to deliver new medicines to patients. While the availability of new excipients are limited, excipient manufacturers have responded to this need by improving on existing materials to help reduce development time and bring down manufacturing costs. HPMC has benefited from recent improvements with the availability of multiple directly compressible (DC) grades for use in formulating controlled release matrix tablets. Typically, a granulation step is required to ensure the drug is well distributed in the matrix and improve the flow and compactability of HPMC for use in high speed tableting (55). The poor flow of standard HPMC grades can be problematic for direct compression where it can result in high tablet weight variability leading to content uniformity issues (56) It is also important for dry granulation with roller compactors which are not able to convey poorly flowable material into the compaction area between the rolls.

Drugs which have water induced degradation cannot be used with wet granulation processes (57). A directly compressible version of hydroxypropyl methylcellulose allows for the drug to be mixed directly with the excipients, avoiding a granulation step completely. Not only does this reduce manufacturing equipment and cycle times significantly, but it also reduces the amount of the drug (active pharmaceutical ingredient, API) required and the development work needed to establish the process parameters, design space and scale up of the granulation processes because there are fewer processes steps to characterize and optimize. This cuts down on development costs and time, which in the end helps to deliver important medicine to patients faster.

For an excipient to work well in a direct compression process it must have sufficient flow to avoid problems during high speed compression. These properties also make directly compressible HPMC appealing for use in continuous manufacturing formulations (58). Many companies are beginning to utilize continuous manufacturing processes for drug development and commercialization to reduce the time it takes to develop and scale up new formulations and provide them to patients (19, 59-61). One of the advantages of continuous manufacturing is the wider applicability of direct compression to drugs and drug loads that would have resulted in segregation with batch processes. Since small amounts are being blended/ transferred continuously there is limited potential for segregation to occur (62).

This current research was undertaken to better understand and characterize directly compressible HPMC grades for use in controlled release matrix tablets.

2 MATERIALS AND METHODS

2.1 Materials

Six different Benecel^{TM} Hypromellose lots of HPMC were sourced from Ashland Inc., consisting of three standard grades of K100M, K15M, K4M and the respective three directly compressible (DC) grades. The standard grades are referred to as controlled release (CR) grades by the manufacturer as they were the first improvements to HPMC for use as an excipient. The ‘K’ defines it as a Hypromellose 2208 type which indicates a specific range of ratios of hydroxypropyl and methyl substitution and determines the overall performance in hydrophilic matrix systems. K-chemistry HPMC has the highest ratio of hydroxypropoxyl to methoxyl substitution and establishes the gel barrier the quickest. This fast rate of hydration followed by quick gelation is needed for the polymer to form a protective gelatinous layer around the matrix to delay the release of the drug. This gel layer prevents the tablet from immediately disintegrating and is especially critical with water-soluble drugs and water-soluble excipients (63) as shown in **Figure 1**.

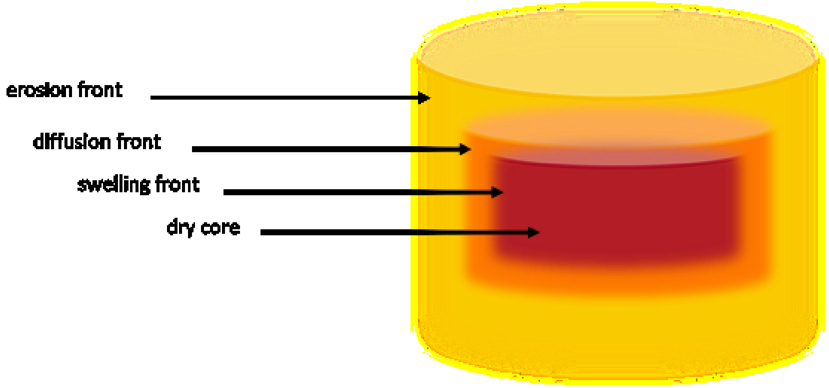

Figure 1 Diagram of the evolving fronts within a hydrating hydrophilic matrix tablet a little time after immersion in an aqueous environment when the fronts are properly established. Colored for emphasis and shown as if able to "see into" the tablet.

The 'M' indicates viscosity x1000 (e.g. K100M = viscosity of 100,000 cPs). These grades represent a range of viscosities that can be used for controlled released hydrophilic matrix tablets and are currently the only three that are also available as DC grades. The DC grades are co-processed with silica at <1 weight percent to improve flow and compactability. Material properties for the six materials are provided in **Table 1**.

Table 1 Benecel^{TM} Hypromellose lots and properties used in this study. Data provided by supplier.

HPMC Material Grade	Abbreviated as	Vendor Lot	Weight Average Molecular Weight	Nominal Viscosity of 2% solution (mPa*S)
Benecel K100M PH CR	K100M CR	1671853	1,000,000	75,000 - 140,000
Benecel K15M PH CR	K15M CR	1474337	575,000	13,500 - 25,200
Benecel K4M PH CR	K4M CR	1530285	400,000	2,700 - 5,040
Benecel K100M PH DC	K100M DC	140501	1,000,000	75,000 - 140,000
Benecel K15M PH DC	K15M DC	140202	575,000	13,500 - 25,200
Benecel K4M PH DC	K4M DC	140720	400,000	2,700 - 5,040

2.2 Powder Characterization Methods

2.2.1 Sample Preparation

Received samples were separated into representative sample portions for powder testing using a spinning riffler (Retsch GmbH PT-100). Spinning rifflers are preferred over other techniques (64) to take representative portions of free flowing powders and work by slowly presenting a sample stream to a rotating set of containers to collect the samples over time (65). They have been shown to be especially good at taking representative sub-samples of a large initial sample (66). The received sample was split and some of those samples were further subdivided using the spinning riffler to prepare multiple small samples to allow for repeat measurements for characterization. This ensured a new representative sample was used for repeat measurements instead of retesting the same material, avoiding potential errors if the sample was altered by the characterization tests.

2.2.2 Bulk Density, Tapped Density and True Density

Multiple techniques were utilized to determine the density for each of the materials. Room humidity was between 51-53% and room temperature was 21-23°C for all measurements.

The powder bulk density for each of the materials was measured using a volumetric bulk density tester (Scott Volumeter). Weight of the 16.4 mL empty sample cell was measured and placed under the volumeter. Powder was gently poured in until the sample cell was completely full. Excess material above the sample cell was removed using a flat spatula. The mass of material added to the sample cell was measured and the bulk density was calculated according to the formula:

$$\text{Bulk Density} = \left(\frac{Mass\ of\ material}{Volume\ of\ sample\ cell}\right).$$

All measurements were made in triplicate using new samples each time.

The conditioned bulk density was measured using a Powder Rheometer (FT4, Freeman Technology) with a 25 mm X 25 mL split vessel, 23.5 mm blade and 25 mm vessel base. The split vessel with base was tared and the sample added to a volume above the split level. A standard conditioning cycle was used so that the powder flowed around the blade resulting in gentle displacement in order to loosen and slightly aerate the powder. The top of the split vessel was then slid off to remove any excess material from the vessel and the mass of remaining material was determined. All measurements were made in triplicate using new samples each time and the sample vessel and blade were cleaned and dried between each measurement.

The bulk and tapped density were measured using a tap density tester (Vankel Model: 50-1000) with a 100 mL graduated cylinder. Approximately 80 mL of sample was gently poured into the cylinder and the volume and mass of the sample were recorded without leveling the powder (e Silva et al., 2013). The sample was tapped 1250 times and the tapped volume was recorded as per recommended procedure for Method I (67). The measurements were made in triplicate using new samples each time. The bulk density was determined using the formulas:

$$\text{Bulk Density} = \left(\frac{Mass}{Starting\ volume}\right) \text{ and Tapped Density} = \left(\frac{Mass}{Final\ volume}\right).$$

The powder true density was measured using a helium pycnometer (AccuPyc II 1340, Micromeritics Instruments) which has been shown to have good accuracy and reproducibility since helium is able to penetrate into crevices and pores to determine the real volume (68). Care was taken to dry the material completely and limit the environmental exposure prior to testing since HPMC can uptake water from the atmosphere, especially after all the moisture is removed as is the case with most pharmaceutical powders. To prevent any error resulting from moisture, each sample was dried at 50°C for 48 hours and placed in a desiccator to cool before testing. A standard steel sphere was used to check the accuracy of the pycnometer before measurements were made. The sample cell was tared and filled with material until it was approximately 75% full. The mass of the material was determined to 0.0001 g. The target pressure of ultra-high pure helium was 19.8 psig for 3 minutes purge with 3 cycles performed for each sample. Each test was repeated two more times with new samples.

2.2.3 Particle Size

The particle size distribution of the samples were determined using a vibrating sieve analyzer (ATF Sonic Sifter) with the following 3 inch diameter sieve screen sizes: 150 µm, 106 µm, 90 µm, 75 µm, 53 µm, 38 µm and the standard collecting pan representing 0 µm which collects any material that passes through the 38 micron sieve. Approximately 5 grams of sample was added to the top of the sieve stack. Testing parameters were: sift setting of 5, pulse setting of 5 and run time of 5 minutes. After sieving, each screen including the pan was weighed to determine the mass of material collected on each of the sieve screens.

Particle size was also measured using dynamic image processing instead of typical laser diffraction due to the elongated nature of HPMC particles. Laser diffraction methods have the disadvantage of assuming spherical particles while image analysis is independent of the particle orientation with a large number of measurements (> 10^7 particles) and low error (69). Image analysis also provides information on shape as well as the particle size. The particle size was measured via image analysis (Sympatec QicPic GRADIS) using the GRADIS Method M6 lens with a measuring range of 2.8 µm – 5.6 mm and at a frame rate of 400 Hz. Approximately 2 grams of material was added to the vibrating feeder set to 15% feed vibration at 4 mm using a run time of 120 seconds resulting in approximately 1-2 million particles being measured. Each test was performed in duplicate with fresh samples.

The calculation mode used for the particle size was the volume EQPC (EQuivalent Projection area of a Circle) which is based on the diameter of a circle with the same area as the area of the actual particle from image analysis. The aspect ratio was also determined, which gives an indication of the elongation of the particles. It is calculated as the ratio of the minimum to the maximum feret diameter as shown in **Figure 2**. The aspect ratio is the shortest and longest extension of the particle based on the distance between two parallel tangents of the particle after evaluation at different angles and has values ranging between 0 and 1 (70). Lower numbers indicate more elongated particles and a completely spherical particle would have an aspect ratio of 1.

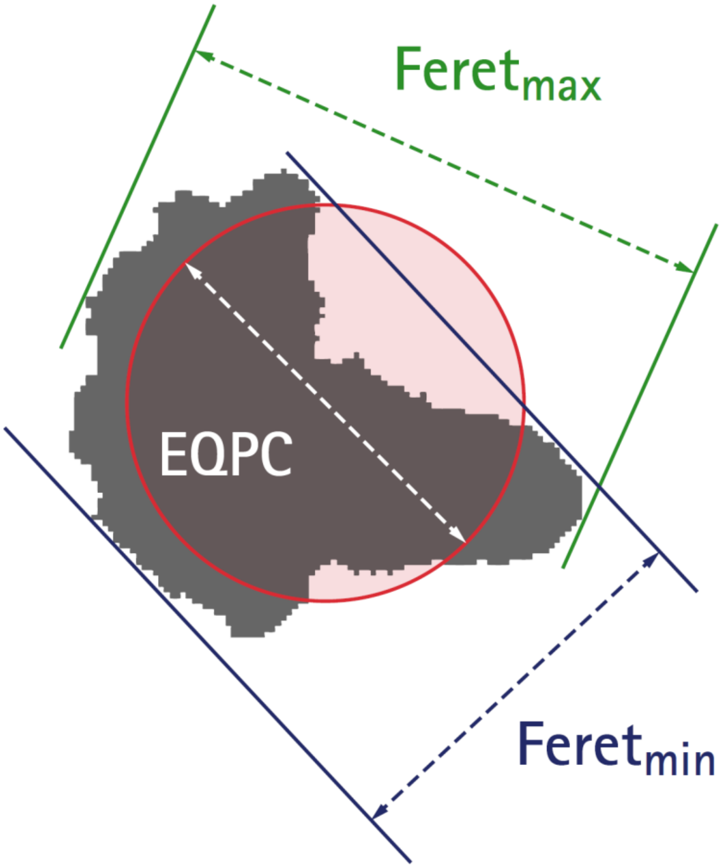

Figure 2 Depiction of EQPC (EQuivalent Projected area of a Circle) and feret diameters used to calculate the aspect ratio (Sympatec, 2019).

2.2.4 Morphology

Scanning electron microscopy (FEI XL30 ESEM, FEI Company) was performed to determine the particle morphology. Images were collected on samples mounted on aluminum stubs to which adhesive carbon conductive tabs had been applied. They were sputter coated using a Cressington 208 HR Auto Sputter Coater equipped with a platinum target (Ted Pella, Inc.). Secondary electron images were acquired at 3 kV at magnifications of 50x, 100x, 250x, 500x and 1000x.

2.2.5 Surface Area

Specific surface area was measured via volumetric gas adsorption using krypton adsorption (B.E.T. volumetric method) at 77 K, using a Quantachrome ASiQ2 autosorp volumetric gas sorption apparatus (Quantachrome Instruments, Boynton Beach, FL, USA). The samples for the first set Trial 1 were between 1.4-1.8 g sample weights and were out gassed and dried under vacuum at 50°C for 672 hours. The samples for the second set Trial 2 were between 2.7-3.4 g sample weights and were out gassed and dried under vacuum at 50°C for 797 hours. The B.E.T. program used 11 pressure points in a relative pressure range of 0.05 to 0.30 and 20.5 Å^2 was used as the cross-sectional area of krypton (71).

2.2.6 Powder Flow

Due to the importance of powder flow in tableting and continuous feeding as one of the main benefits in using the directly compressible grades of HPMC, multiple techniques were utilized to characterize the powder flow. Since powder flow is multifaceted attribute it requires multiple techniques to evaluate flow under different conditions. Room humidity was measured between 51% and 53% and room temperature was 21-23°C during all tests described below.

A common technique used to characterize powder flow is the Carr's Index. Relative changes in density can be indicators of changes in the structural strength of a loosely compacted powder and hence of its flow characteristics in many process operations (72). The index was calculated using the following equation:

Carr's Index = $100 * (\frac{\rho\text{tap} - \rho\text{tbulk}}{\rho\text{tap}})$ where ρ_{bulk} is the bulk density and ρ_{tap} is the tapped density.

Additional flow measurements were made using a flow tester (Erweka GT Flow Tester) equipped with an 11.3 mm nozzle using a stirrer setting of 2. Approximately 30 g of material was poured into the 200 mL hopper. An empty container was placed underneath the funnel and tared. Material was allowed to flow from the funnel while measuring the change in weight over time to determine the mass flow. Each sample measurement was repeated in triplicate.

Powder flow under dynamic conditions was studied using an avalanche tester (API AeroFlow, Amherst Process Instruments Inc.) to determine the length of time for material to avalanche in a rotating drum via a light absorption sensor. Material was placed in a transparent disc with a photocell array located behind the disc which collected information on the quantity of light passing through. As the disc rotated, the photocell array recorded light variations during the cyclic formation of avalanches from the flowing powder. The results are expressed as the total number of avalanches and time between each avalanche, which represents the duration of a complete cycle (73). A sample of 50 mL was used with the rotation set at 180 seconds per rotation using a 5 Hz sampling rate. The data were collected and analyzed using the instrument's data acquisition software.

2.2.7 Shear Cell

Material was added to the shear cell (i–Shear Powder Flow Rotational Split Level Shear Tester, E & G Associates) to prevent any void space and excess powder above the consolidation ring was leveled and removed. The sample was then pre-consolidated using a consolidation plug and an Automated Consolidation Bench (E & G Associates) at a pressure below the intended consolidation pressure. Weights were placed on the top shaft to produce an effective normal consolidation pressure on the powder bed for five minutes. When the powder bed had been critically consolidated at the normal stress, a critical shear stress was determined. A set of five different consolidation pressures of 5, 10, 15, 20, and 25 g/cm^2 were used to produce five shear stresses in order to determine the yield locus. When sufficient data had been obtained at steady state to define the yield locus, two Mohr circles were drawn tangential to the envelope to obtain the two pertinent flow parameters, which are the uni-axial compressive strength and the flow function coefficient.

2.2.8 FT4 Powder Rheometer

The powder flow was also determined using a Powder Rheometer (FT4, Freeman Technology) which uses an instrumented impeller to measure the torque, force and distance while traversing through the powder sample. The tests were performed using a 25 mm X 25 mL split vessel, 23.5 mm blade and 25 mm vessel base. The same procedure described above for bulk density measurements was used, but after powder conditioning the recommended methodologies were run to determine the Basic Flowability Energy, Stability Index, Flow Rate Index and Specific Energy (74). All measurements were made in triplicate using new samples each time and the sample vessel and blade were cleaned and dried as per manufacturer recommendations between each measurement.

2.3 Tablet Compaction Studies

Tablet compaction studies were performed using a high speed compaction simulator (StylOne, Medel'pharm) along with the data acquisition software (Analis). The equipment utilizes symmetrical compaction from both the upper and lower tablet punches at speeds representative of industrial rotary tablet presses while using small amounts of material. Compaction simulators have been demonstrated to be useful in determining the compaction behavior of pharmaceutical materials (75-78). Machine and tooling deformation under variable pressures was determined for the punches and used to correct the linear variable differential transformers (LVDT) which measure punch displacement during compression for increased accuracy.

The precompression was removed and the compression was run at a speed of 100 msec compression and 100 msec decompression giving dwell times around 15 msec which reflects typical high speed compression for a commercial rotary tablet press. A sampling rate for data acquisition of 2000 Hertz (measurements per second) was used for this study. The compression forces were measured with calibrated strain gauges located on the upper and lower punch holders with an accuracy of 10 Newtons. The punch displacement for upper and lower punches were measured using displacement transducers with an accuracy of 0.01 mm.

Standard Euro-B flat-face round punches with a 10 mm diameter were used to compress tablets weighing approximately 200 mg at different compression pressures to target four different pressures with solid fractions ranging from 0.80–0.90. The solid fraction (SF) = 1-porosity where tablet porosity $\varepsilon = 1 - \frac{\rho_{tablet}}{\rho_{true}}$ where ρ_{true} is the measured true density and ρ_{tablet} is the calculated tablet density based on the measured tablet weight, thickness and diameter. The tablet density can be calculated from $\rho_{tablet} = \frac{M}{\pi\left(\frac{D}{2}\right)^2 t}$ where M = tablet mass (g), t = tablet thickness (cm), and D = diameter of tablet (cm). A solid fraction of 0.85 is commonly used in comparing materials since that is typical for tablets (79, 80). Tablets were compressed individually such that individual tablet measurements could be related to the compaction event. External die lubrication using magnesium stearate was used to ensure the materials did not stick to the tooling surfaces and was preferred over blending the material with magnesium stearate which would impact the compaction results and to minimize the impact of die wall friction on the powder property measurement. External lubrication was achieved by lightly brushing the punch faces and the inside of the die before every other compression event with a magnesium stearate covered swab after tapping to remove excess material. Ten tablets were manufactured at each set of parameters.

2.3.1 Moisture Sorption studies

It was observed that both the powder and tablets picked up moisture upon exposure to the atmosphere which can impact testing results (81-84). The material was transported as 250 g of each material in an amber glass jar with external desiccant in a 10 gallon fiber drum. Before the powder for each tablet was weighed the jar was rotated three times to ensure a new, unexposed powder sample was weighed for each tablet. After the powder for the tablet was weighed, the lid was replaced immediately while the tablet was compressed and tested. If this procedure was not followed the tablets would pick up moisture which would then impact the tablet weight, thickness, diameter and hardness. As a result, the tablet properties were measured immediately after each tablet compression to differentiate the materials without being confounded by changes due to moisture absorption from varying room environmental conditions and testing time.

To evaluate the impact of moisture, two powder samples of 700 g of HPMC K15M DC were left in a weight boat for 24 hours where the temperature ranged from 22-24 °C and relative humidity 46-50%. Powder from those samples were used to make two tablets and compared to two tablets manufactured with fresh powder samples. All of the tablets were then left to sit and tested intermittently for weight, thickness, and diameter at different time points. After six hours the tablets were also tested for hardness and compared to tablets made with fresh powder samples and tested immediately.

In addition to exposing the powder to the environmental conditions before compressing the tablets, a comparison of change in tablet properties over a short period of time using fresh powder was performed using K100M CR and DC material. It is well established that there may be an impact to tablet hardness / tensile strength for many different pharmaceuticals materials and that effect can vary between increasing and decreasing tensile strength of the tablets based on the material and the amount of moisture (83, 85-88). Five tablets at each of the four different compression forces were manufactured for both HPMC K100M CR and HPMC K100 DC using fresh powder and then tested after open dish exposure for two hours in room conditions of 22°C and 44-45% relative humidity and compared to tablets tested immediately after compression.

2.3.2 Tablet Testing

The tablet weight (Kern ABJ-NM/ABS-N), diameter and thickness (Mitutoyo C125XB gauge) were measured after ejection of the tablet to determine the out of die dimensions. The tablet hardness was measured using a tablet hardness tester (Erweka TBH-325) and the diametrical tensile strength was calculated using the following equation: $\sigma_{\text{tensile}} = \frac{2P}{\pi * D * t}$ where $\sigma_{\text{tensile}} =$ diametrical tensile strength (MPa), P = tablet hardness or breaking force (N), t = tablet thickness (mm) and D = diameter of tablet (mm).

2.4 Calculation and comparison of p-values

The data was analyzed with Minitab (version 17) statistical software using a two sample t-test to compare the population means of all of the CR grades to all of the DC grades to determine whether they are significantly different at a p-value of $p < 0.05$. Data was also analyzed and graphed using software tools including Excel (version 2016), JMP (SAS version 13), and Spotfire (TIBCO Analyst Version 7.11.1 LTS).

3 RESULTS AND DISCUSSION

3.1 Density

Density is important characteristic for excipients impacting both the powder flow as well as the potential for segregation with other excipients or drug and can be problematic for pharmaceutical manufacturing when the density is at either extreme. Not only is the bulk density important for the fill volumes of bins and blenders but it can also impact the tablet compaction process. Filling of the powder into the tablet die during tableting is one of the reasons for adding a granulation step to increase density and improve flow.

The powder bulk density can depend on many different properties especially particle size and overall size distribution, the particle shape and surface texture, the cohesive/adhesive forces between particles, as well as electrostatics. A table of all density results from the different testing techniques is provided in **Table 2**.

The conditioned bulk density as determined using the FT4 powder rheometer has the benefit of using an automated procedure to reproducibly condition the powder to ensure a low stress, homogeneous packed state free of excess air. Testing indicated that the directly compressible grades of HPMC had higher bulk density than their standard counterparts as shown in **Figure 3**. While the standard grades had variable bulk densities in the order of K100M CR < K15M CR < K4M CR, the DC grades had only slight differences and did not indicate a trend. As such, the improvement in density for the DC grades was the most significant for K100M. Since the particle size, shape and morphology are similar, this result although small in magnitude is unexpected, but also apparent in the other bulk density tests. This may be a result of different particle interactions with the DC grades allowing for more settling of the material.

The bulk densities determined from the graduated cylinder method showed a similar trend but were lower overall when compared to the FT4 conditioned bulk density. This method is known to have measurement errors due the difficulty in determining the volume accurately using a visual assessment of a sloped powder (72) but the measurements still had good reproducibility with relative standard deviations less than 1% for the measurements. The DC grades had higher bulk density than the CR grades and K100M CR exhibited the lowest bulk density as shown in **Table 2**. Results from the Schott's Volumeter indicated a similar trend. The tapped density values were only used for the Carr's Index calculation reported later, but the DC grades also had higher tapped densities.

The true density is the mass of material divided by its volume at zero porosity and is useful in studying particle behavior under pressure during compaction. The true density was measured on triplicate samples with good reproducibility with the average of the three measurements provided in **Table 2**. The true density was slightly higher for the DC grades.

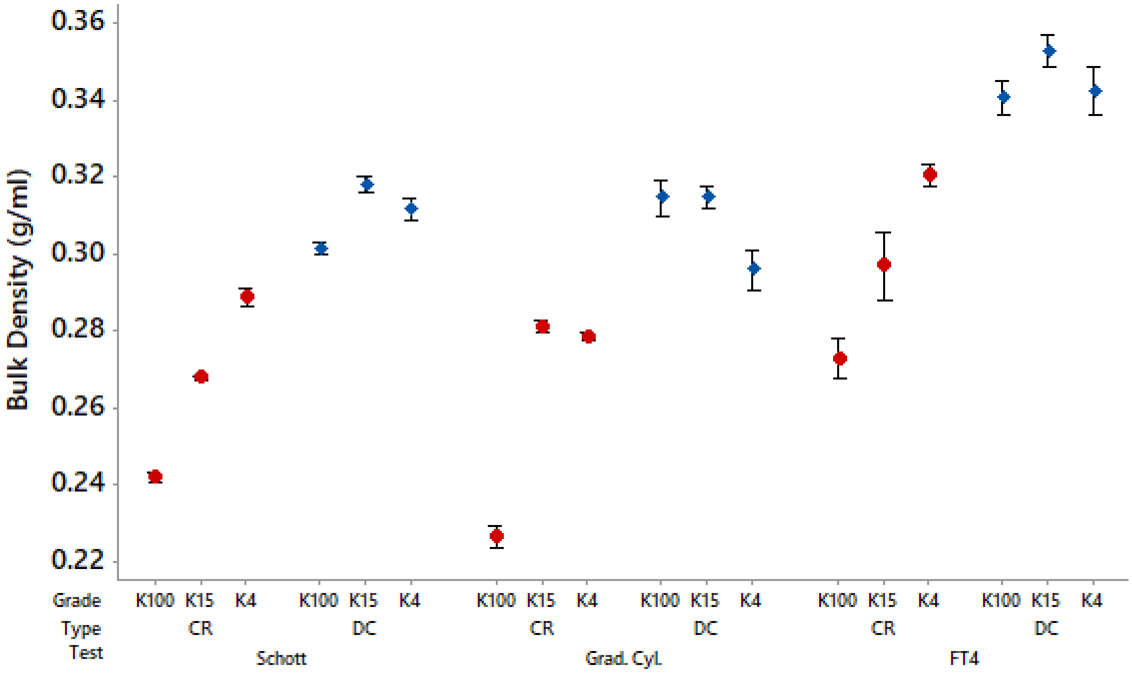

Figure 3 Bulk density from three different tests. Red circles indicates CR and Blue diamonds indicates DC Type.Standard deviations are alsoaslo shown for each measurement.

Table 2 Bulk density, tapped density and true density.

	Average Bulk Density (Standard Deviation)				
Grade	Schott Volumeter (g/mL)	Graduated Cylinder (g/mL)	FT4 Conditioned (g/mL)	Average Tapped Density (g/ml)	Average True Density (g/mL)
K100M PH CR	0.242 (0.001)	0.226 (0.001)	0.273 (0.003)	0.430 (0.002)	1.301 (0.003)
K15M PH CR	0.268 (0.000)	0.281 (0.001)	0.297 (0.004)	0.466 (0.004)	1.307 (0.003)
K4M PH CR	0.289 (0.001)	0.279 (0.000)	0.320 (0.001)	0.478 (0.000)	1.285 (0.002)
K100M PH DC	0.302 (0.001)	0.315 (0.003)	0.341 (0.003)	0.494 (0.006)	1.315 (0.004)
K15M PH DC	0.318 (0.001)	0.315 (0.001)	0.353 (0.002)	0.505 (0.003)	1.315 (0.004)
K4M PH DC	0.311 (0.001)	0.296 (0.002)	0.343 (0.003)	0.492 (0.002)	1.309 (0.002)
p-value (CR vs DC)	0.000	0.001	0.005	0.001	0.000

3.2 Particle Size

The results from the image analysis are provided in **Table 3**, **Figure 4** and **Figure 5**. The aspect ratios were nearly identical which indicates that the material shapes are similar and supported with a non-statistically significant p-value ($p > 0.05$) when comparing CR to DC. Particle size showed a mean size (D_{50}) around 100 µm with the DC grades being slightly smaller in size than the CR grades and the distributions were very similar within each of the grades. The average size differences between the CR and DC grades were D_{10} = 5 µm smaller, D_{50} = 16 µm smaller and D_{90} = 37 µm smaller for the DC grades. This is counter to expectations for better flowing material. Typically, powder flowability increases with the increase in particle size if other properties are kept similar (89). The particle size showed very reproducible results between the duplicate measurements. The maximum difference for all samples in repeat testing was low for D_{10} < 1.2% (0.7 µm), D_{50}< 1.3% (1.6 µm) and D_{90} < 1.8% (3.9 µm).

Table 3 Average particle size and aspect ratio (indicates shape) as measured by QICPIC image analysis. Standard Deviation of the Aspect Ratio was 0 for all calculated values.

Grade	Average Particle Size (µm) and SD			Average Aspect Ratio		
	D_{10}	D_{50}	D_{90}	D_{10}	D_{50}	D_{90}
K100M PH CR	59 (0.0)	116 (0.8)	220 (2.8)	0.36	0.56	0.79
K15M PH CR	62 (0.2)	125 (0.4)	209 (1.1)	0.37	0.57	0.79
K4M PH CR	64 (0.4)	125 (1.1)	223 (1.1)	0.38	0.58	0.80
K100M PH DC	57 (0.1)	107 (0.1)	184 (0.2)	0.37	0.57	0.80
K15M PH DC	56 (0.5)	106 (0.4)	191 (0.5)	0.37	0.58	0.80
K4M PH DC	56 (0.3)	105 (0.5)	182 (0.7)	0.37	0.58	0.80
p-value (CR vs. DC)	0.003	0.000	0.000	N/A*	0.153	N/A*

* Means are identical = no difference for comparison

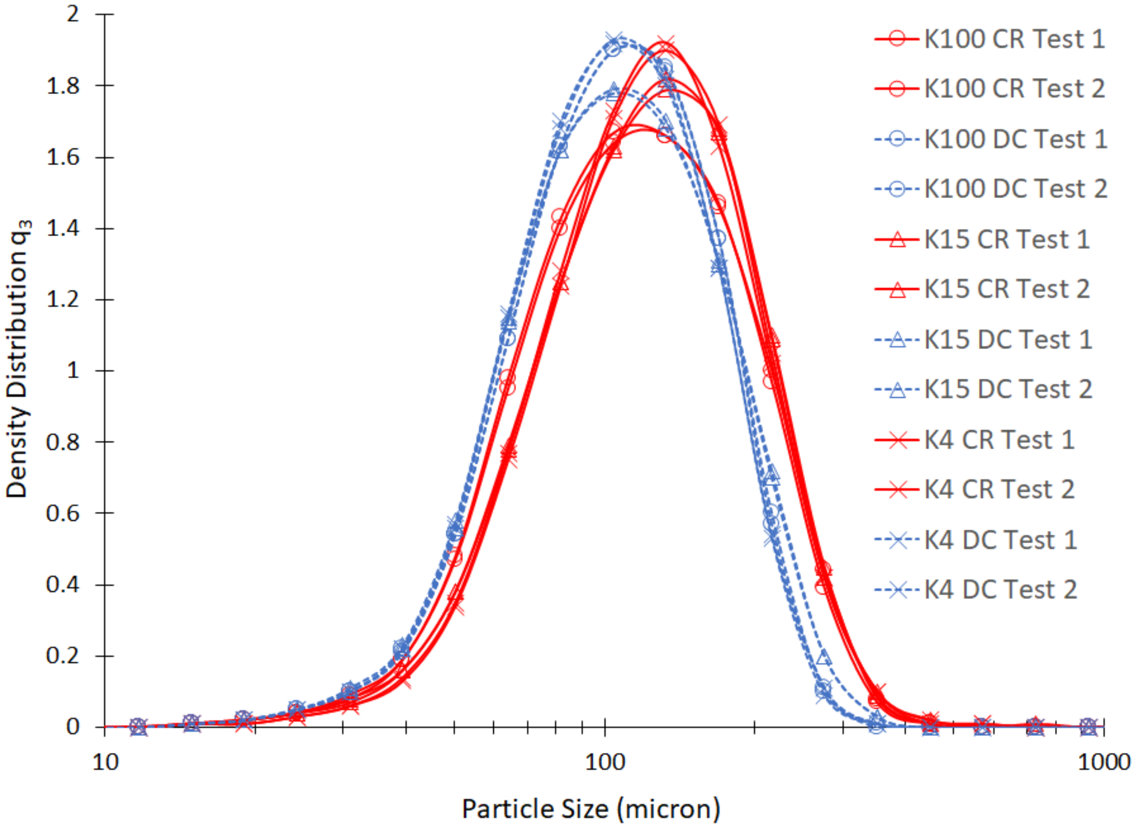

Figure 4 Individual particle size density distribution from QICPIC image analysis for CR grades (red solid line) and DC grades (blue dotted line). K100M circle, K15M triangle and K4M shown as cross.

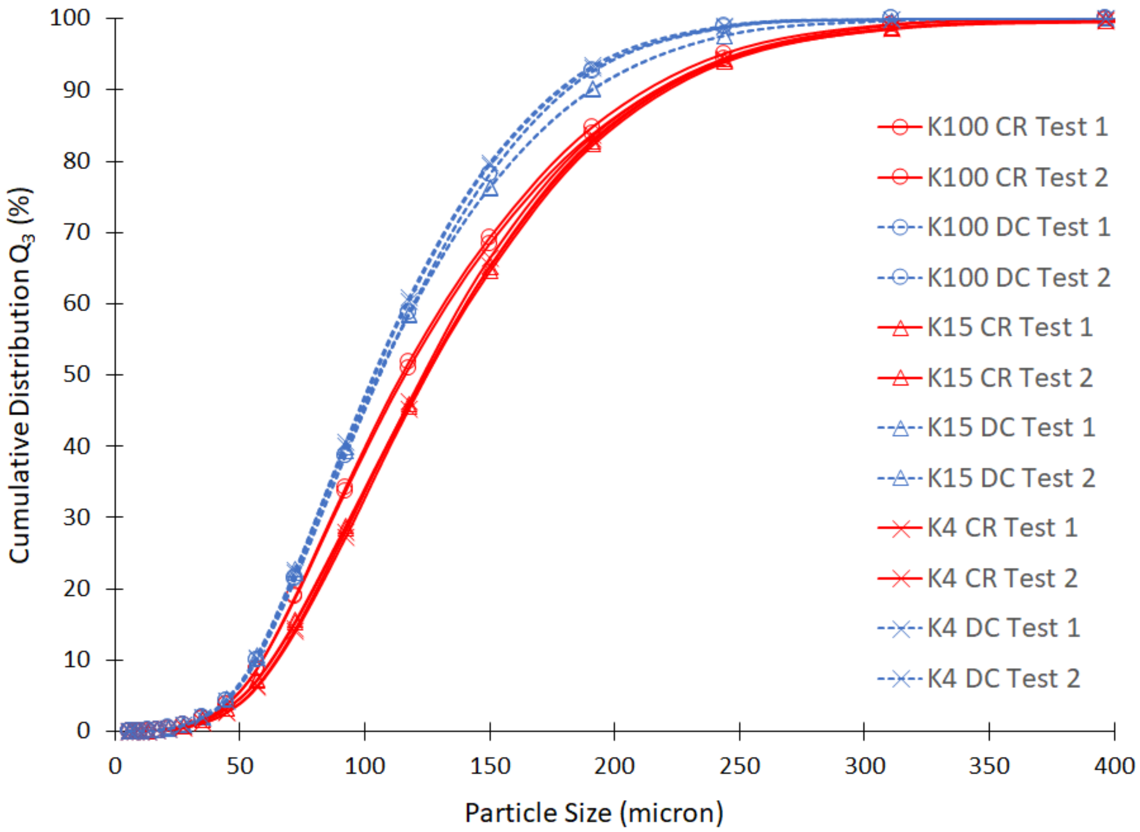

Figure 5 Individual particle size cumulative distribution from QICPIC image analysis for CR grades (red solid line) and DC grades (blue dotted line). K100M circle, K15M triangle and K4M shown as cross.

Because of the elongated shape of the HPMC particles it is expected that the results of sieve testing may not yield accurate results because the elongated HPMC particles can pass through the sieve openings based on their smallest cross-sectional diameter. For instance, a needle like particle could pass through a smaller hole when standing on end than it could lying horizontally. However, the particle size measurements exhibited a similar trend as the image analysis with the DC grades being slightly smaller in size than their CR counterparts. **Figure 6** shows the DC grades having more material collected in the fines collector (passing through 38 µm screen) after the sieve test compared to the equivalent standard grade.

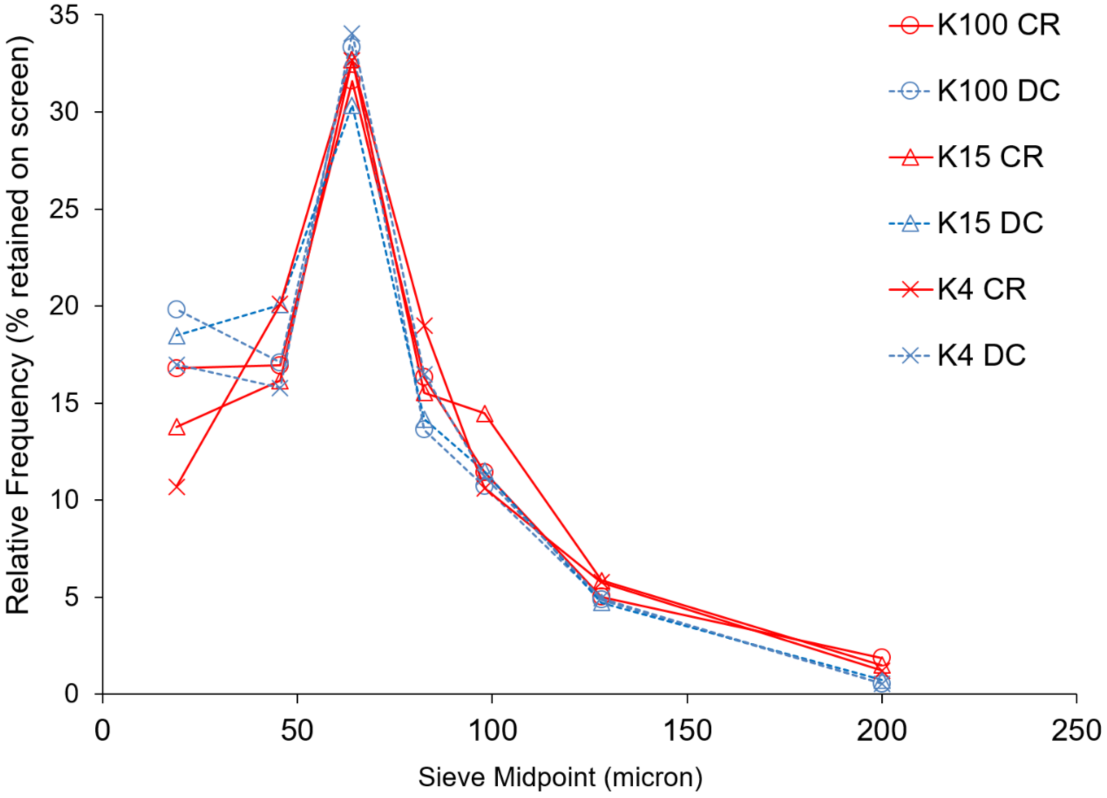

Figure 6 Particle size distribution as measured by sieve analysis for CR grades (red solid line) and DC grades (blue dotted line). K100M circle, K15M triangle and K4M shown as cross.

3.3 Particle Morphology

Scanning electron microscopy (SEM) was performed at magnifications of 50x, 100x, 250x, 500x and 1000x to compare the particle morphology. While interpretation of SEM photographs can be somewhat qualitative and subjective, both grades of polymer appear to be made of agglomerates of fiber-like particles which have combined to form larger, elongated particles. The surface of all of the DC grade material appears to be smoother that the standard CR grades with less noticeable occlusions under higher magnification. Only magnifications of 100x and 500x are shown in **Figure 7** to provide examples with the remaining included in the **Appendix**.

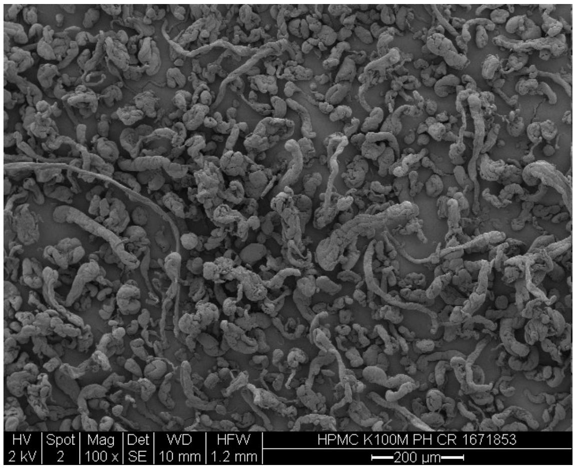

a) K100M CR 100x

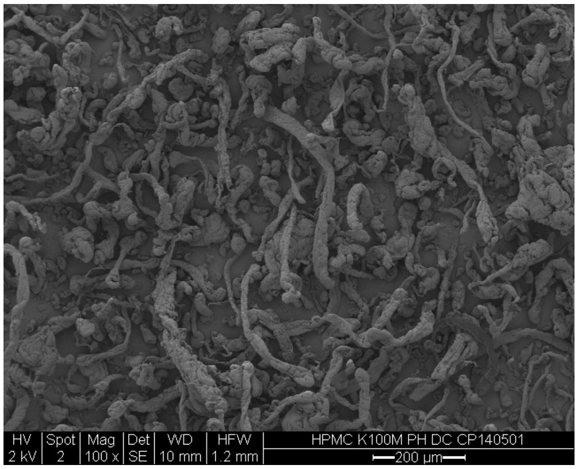

b) K100M DC 100x

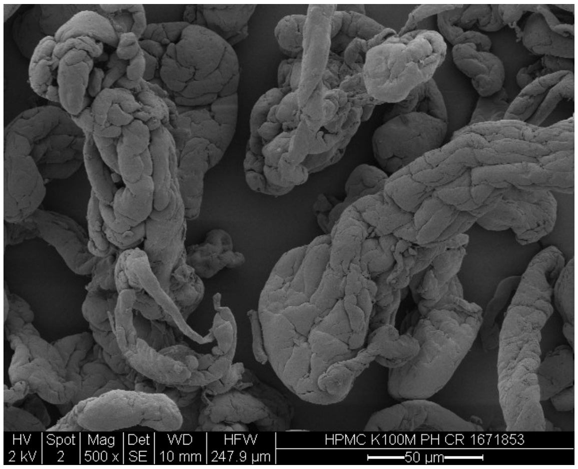

c) K100M CR 500x

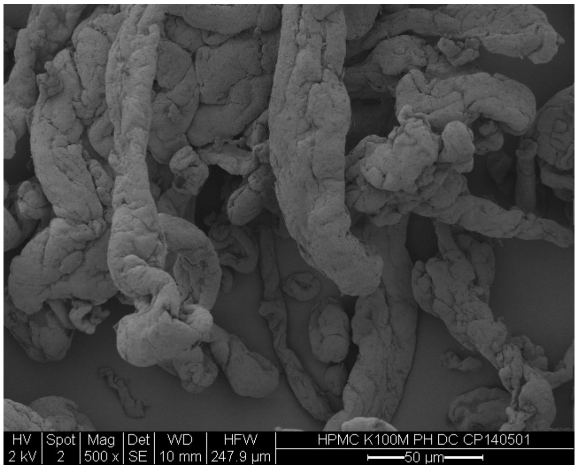

d) K100M DC 500x

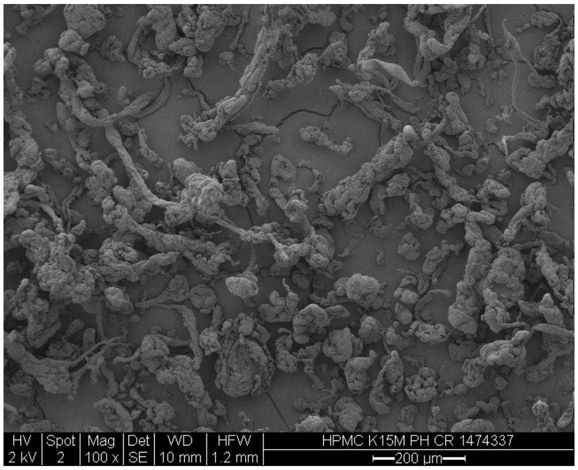

e) K15M CR 100x

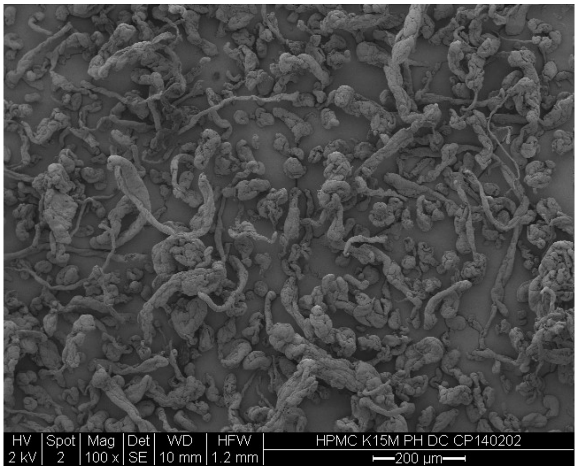

f) K15M DC 100x

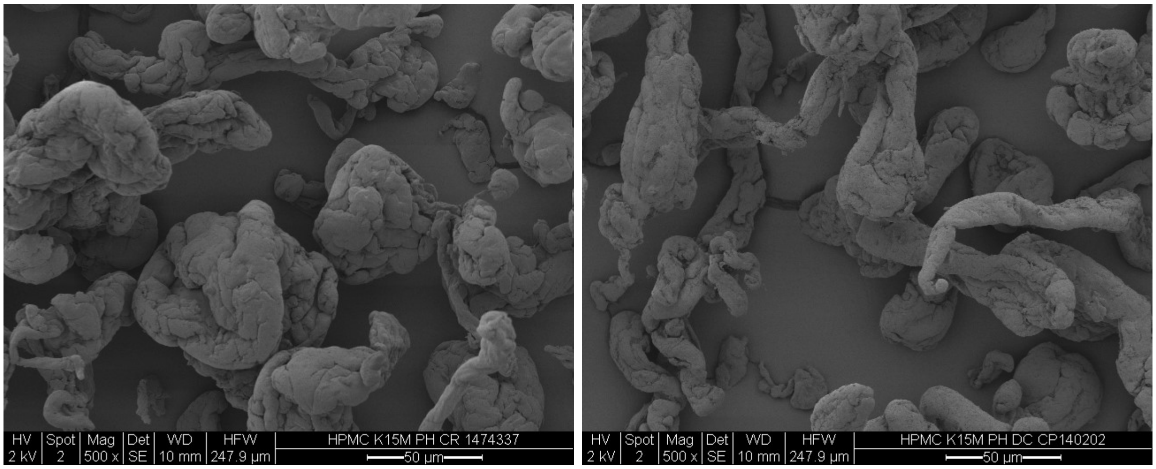

g) K15M CR 500x h) K15M DC 500x

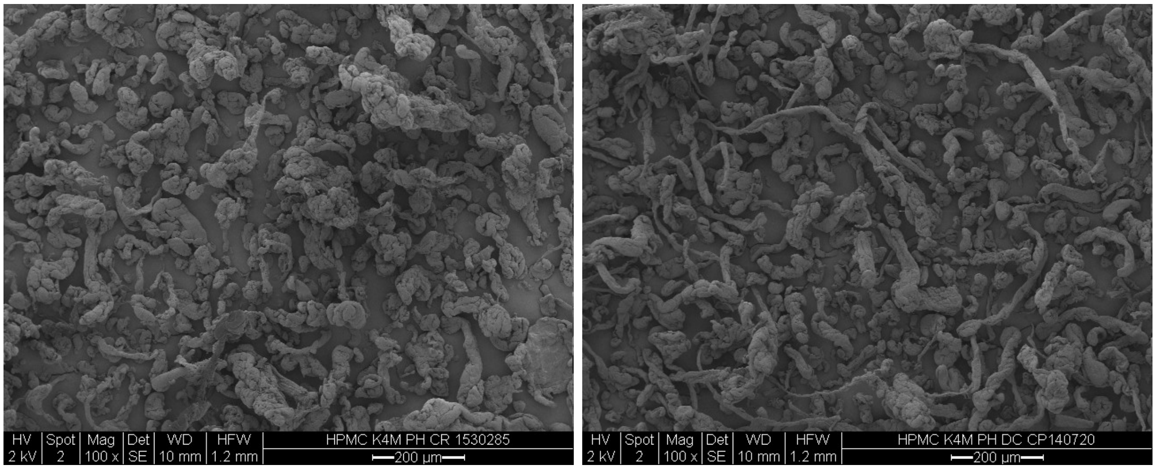

i) K4M CR 100x j) K4M DC 100x

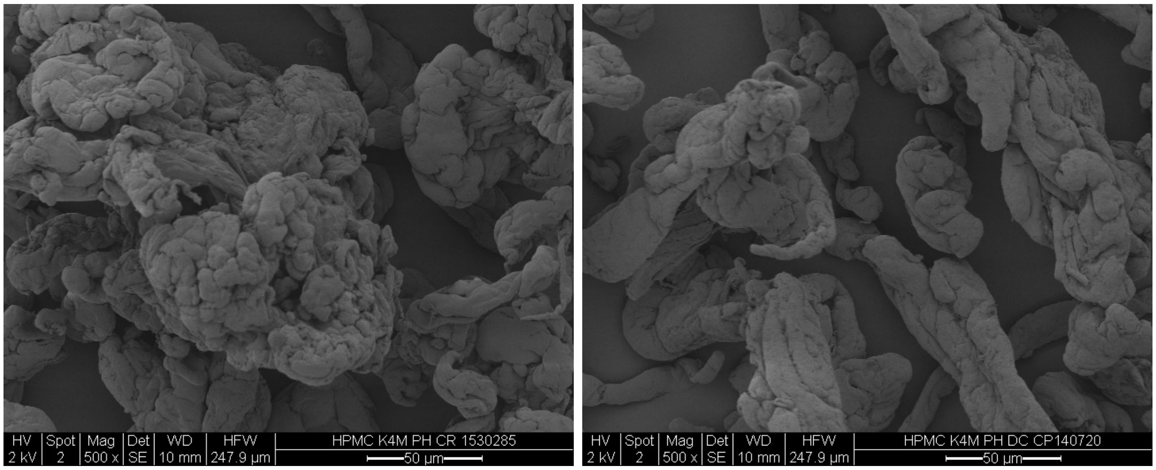

k) K4M CR 500x l) K4M DC G500x

Figure 7 *a-l) Representative SEM images for K100M, K15M and K4M comparing CR grade and DC grades at 100x and 500x magnification.*

3.4 Particle Surface Area

There was some analytical variability for surface area measurements between the different sample sizes and outgas times, but overall good agreement as pictured in **Figure 8**. The correlation coefficients were above 0.999 within each test for the surface area measurements. Interestingly, the surface area for the DC grades were three times higher than the corresponding CR grades. This increase in surface area cannot be attributed to the small difference in particle size, shape, or morphology since they were very similar between the grades. The increased surface area is likely due to the incorporation of a small amount of silica in the DC grade material. Silicon dioxide (SiO_2) itself has a very high surface area around 200 g/m^2 (90) and a similar phenomenon was observed for silicified microcrystalline cellulose where the surface area increased by a factor of three to twenty depending on the level of SiO_2 and method in which it was incorporated (91, 92).

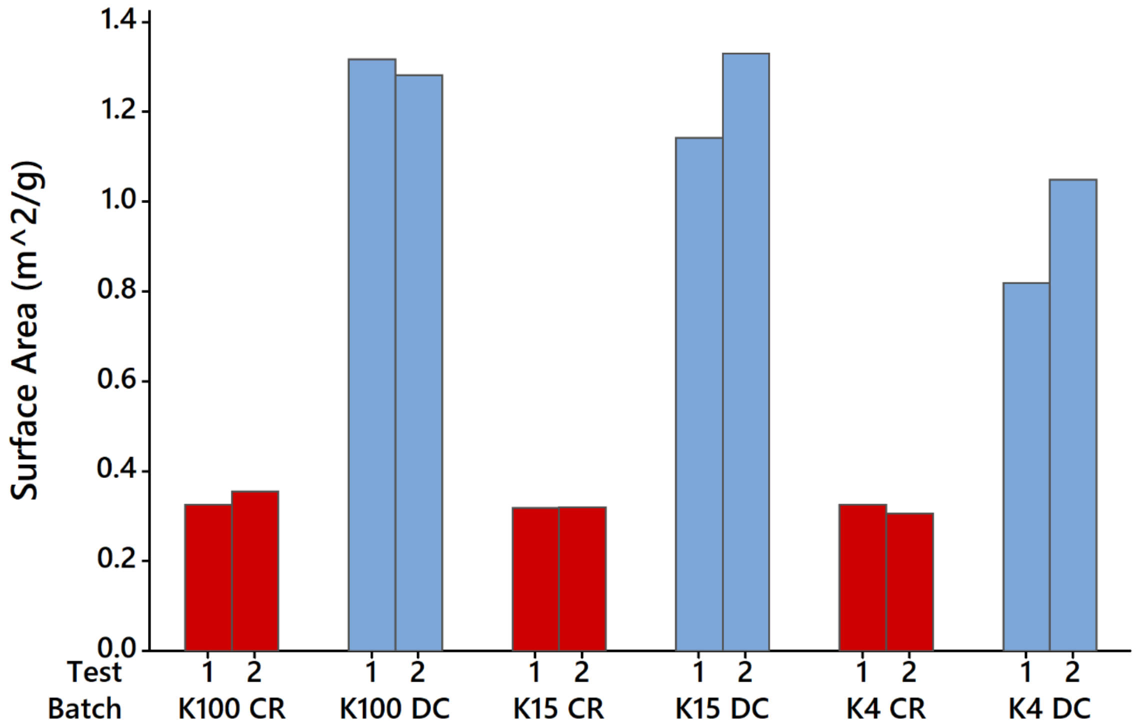

Figure 8 Individual surface area for CR grades (red) and DC grades (blue) measured by B.E.T. krypton adsorption.

3.5 Powder Flow

The Carr's Index is a simple technique for predicting powder flow based on comparing the bulk density to the density after tapping the bulk powder until there is no further change in density. Lower values of the Carr's Index predict better flow of the powder (93). The Erweka flow rate measures the speed at which a powder is able to flow through an orifice with higher values indicating improved flowability. Values for both are shown in **Table 4**. Both a lower Carr's index and a higher Erweka flow rate indicate improved flowability of the DC grade material. Typically, material with larger particle size has better flow especially with materials less than 100 microns (94). However, in this case, the DC grade is slightly smaller in size but had better flow, which is likely attributed to the incorporation of silica.

Table 4 Average powder flow as determined by Carr's index and Erweka flow rate.

	Average Flow Values (and Standard Deviation)	
Grade	Carr's Index	Erweka Flow (g/s)
K100M PH CR	47.4 (0.5)	1.29 (0.08)
K15M PH CR	39.7 (0.5)	4.37 (0.40)
K4M PH CR	41.7 (0.1)	3.75 (0.36)
K100M PH DC	36.4 (0.4)	4.82 (0.64)
K15M PH DC	37.7 (0.2)	4.49 (0.49)
K4M PH DC	39.8 (0.5)	5.87 (0.34)
p-value (CR vs. DC)	0.002	0.004

The FT4 powder rheometer is capable of measuring multiple parameters that relate to powder characteristics which impact powder flow. Results for all of the FT4 tests shown below are provided in **Table 5**. The SI (Stability Index) is a measure of how the powder changes after multiple repeat testing with a combination of seven conditioning and test cycles. For example, if a material segregated, had attrition during testing or moisture uptake, the results may change on repeated testing. Both CR and DC grades had SI close to 1 which is considered robust with $0.9 > SI < 1.1$ being typical values for pharmaceutical powders. The materials were not statistically different.

The FRI (Flow Rate Index) measures the difference in testing energy at varying blade tip speeds. FRI > 3 is considered high and is usually indicates cohesive material while FRI around 1 being considered flow rate insensitive. Most powders have $1.5 < FRI < 3.0$ which was the case with the CR grades. The FRI was slightly lower for the DC grades, but the difference was statistically significant p-value = 0.000, indicating that they may have less sensitivity to differences in flow rate.

The BFE (Basic Flowability Energy) reflects the energy required to create a compressive (high stress) flow pattern in the powder. It is calculated from the work done when moving the blade downward through the powder after conditioning. The DC grades had significantly higher BFE than the CR grades with the p-value = 0.000. The BFE is dependent on a number of properties of the bulk powder such as density, compressibility, packing state in addition to the particle properties of size and shape. The bulk density of the DC grades was shown to be higher such that the better packing of the DC grades contributed to the higher BFE values. This could be due to more particles within the vessel resulting in a low compressibility and high transmissibility of forces from particle to particle. This is because a higher proportion of the sample volume moves and more work is done than with a cohesive powder which contains more entrapped air and is therefore more compressible (74).

The SE (Specific Energy) is a measure of how the powder flows in an unconfined or low stress environment and is calculated from the energy required to establish an upward flow pattern in the conditioned powder which creates a lifting and low stress flow of the powder. As a result, the powder compressibility is less influential (unlike the BFE test) and cohesion forces between particles such as inter-particulate frictional forces and inter-particulate rolling frictional forces are more important. The SE is calculated from the work done in moving the blade upwards through the powder and normalized for the sample mass. In general SE < 5 indicates low cohesion, 5 < SE < 10 indicates moderate cohesion and SE > 10 shows high cohesion. All samples had moderate cohesion with CR grades having slightly lower values than DC grades with the p-value = 0.000. Similar to the BFE, this is contrary to expectations of the DC grades having better flow and also contrary to the results from the avalanche tester which tests the powder flow under low stress. The FT4 offers additional test methodologies around aeration, permeability, and compressibility using different equipment add-ons that could provide more insight into this phenomena.

Combining all of the data available from the FT4's Stability Index and Variable Flow rate test, we can conclude that all of the materials tested were stable during the testing (SI close to 1). The DC grades are likely to be less cohesive, as given by a lower FRI. The higher BFE and SE are likely due to the better packing of the DC grades (higher bulk density) taking more energy to move the material.

Table 5 FT4 rheometer powder flow measurements.

	Average Values and (Standard Deviations)			
Grade	Stability Index	Flow Rate Index	Basic Flowability Energy (mJ)	Specific Energy (mJ/g)
K100M PH CR	0.92 (0.15)	1.51 (0.31)	328 (5)	6.68 (0.17)
K15M PH CR	0.97 (0.02)	1.77 (0.15)	262 (7)	5.91 (0.26)
K4M PH CR	0.92 (0.09)	1.66 (0.02)	229 (7)	5.65 (0.09)
K100M PH DC	1.01 (0.20)	1.15 (0.08)	710 (47)	7.62 (0.13)
K15M PH DC	0.99 (0.09)	1.18 (0.07)	700 (43)	7.21 (0.37)
K4M PH DC	0.94 (0.06)	1.24 (0.02)	574 (20)	6.47 (0.18)
p-value (CR vs DC)	0.383	0.000	0.000	0.000

The avalanche tester measured the overall number of avalanches as well as the mean time, scatter (the standard deviation of the times between avalanches) and maximum time between subsequent avalanches and is shown in **Table 6**. Material that is non-cohesive, which has good flow, will exhibit short and reproducible avalanche times with low scatter. Poor flowing, cohesive material will stick together more and travel up the side of the wall resulting in longer and more variable avalanche times with less scatter (73). The DC grades had more avalanche events with a shorter time between avalanches and less scatter compared to the standard CR grades indicating the DC grades have improved flowability with K4M DC standing out as the best flowing material. However, with the high variability within the types, especially due to the very good avalanche flow from K4M DC, the p-values did not come out as significant when comparing CR to DC because of the variability in the measurements.

Table 6 Avalanche flow testing.

	Time Between Avalanches (sec)			
Grade	Mean	Scatter	Maximum	Number of Avalanches
K100M PH CR	6.65	4.26	16	538
K15M PH CR	7.02	4.48	18	511
K4M PH CR	6.28	3.91	17	571
K100M PH DC	4.34	2.68	13	828
K15M PH DC	4.56	2.68	12	790
K4M PH DC	1.58	0.92	8	2277
p-value (CR vs. DC)	0.060	0.073	0.085	0.262

A visual assessment of the strange attractor graphs for the materials in **Figure 9** demonstrates the improved flow of the DC grade material. The graphs indicate the relative timing of avalanche events from the time in seconds for one avalanche to occur (x-axis) vs. the time for the next avalanche (y-axis). The graphs were scaled from 0 to 15 seconds for direct comparison. The DC materials show smaller, tighter strange-attractor plots indicating shorter and more reproducible time for avalanche events and hence improved flow.

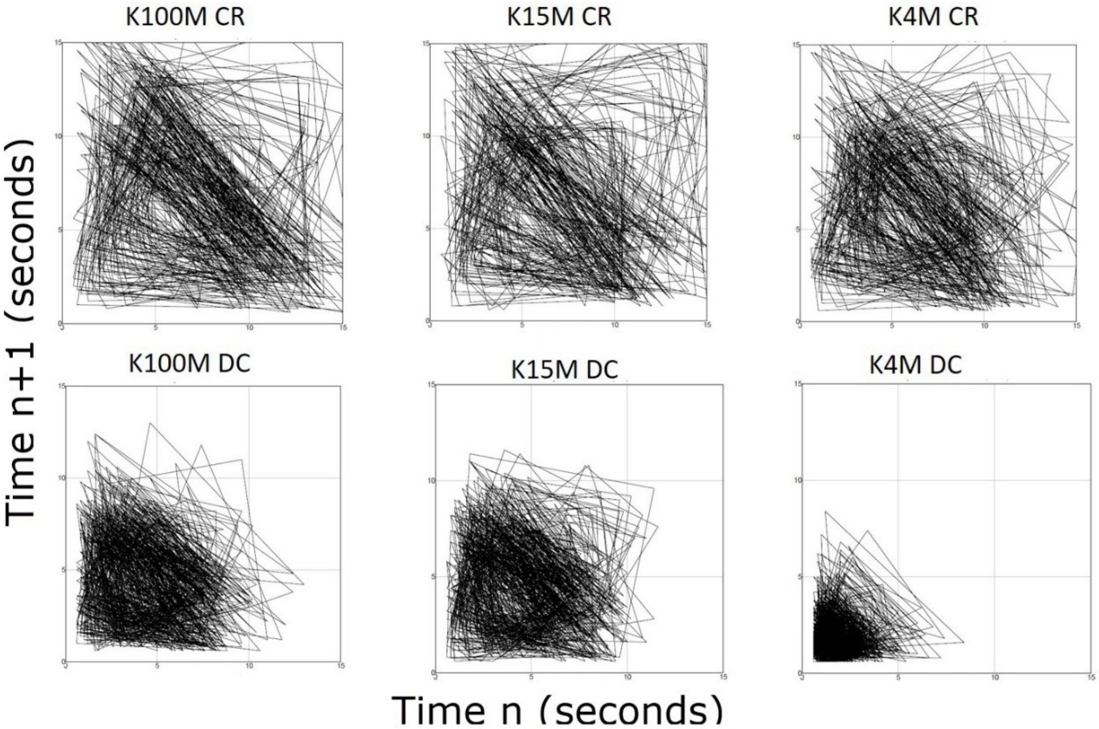

Figure 9 Representative strange attractor graphs for avalanche testing. X and Y axis range 0 – 15 seconds for all.

Shear cell testing is also a common technique for predicting powder flow. The uni-axial compressive strength is defined as the major principal stress that causes an unconfined bulk material to fail in shear. All of the DC grades had significantly lower uni-axial compressive strength values than the CR counterparts indicating less cohesive material. The flow function coefficient (FFC) is the ratio of the major consolidation stress to the uni-axial compressive strength. A higher flow function coefficient indicates more free flowing material. Results for the shear cell testing are shown in **Table 7** and indicated the DC grades had higher flow function coefficients more than double the CR grades and flow function coefficients >10 are considered free flowing (95). The shear cell testing predicts that the direct compaction grades of HPMC will flow better than the standard HPMC CR grade and overall the differences were statistically significant (p-value < 0.05).

Table 7 Shear cell results.

Grade	Uni-axial Compressive Strength (Pa)	Flow Function Coefficient
K100M PH CR	1781	4.66
K15M PH CR	1838	4.94
K4M PH CR	1337	6.06
K100M PH DC	653	12.62
K15M PH DC	476	17.60
K4M PH DC	683	12.48
p-value (CR vs. DC)	0.026	0.035

3.6 Moisture absorption studies

The two powder samples of HPMC K15M DC that were left in a weight boat for 24 hours had 4.2% and 4.6% moisture gain, which is in line with other types of HPMC where moisture sorption isotherms were measured (84, 96, 97).

These samples were used to make tablets as well as tablets made using fresh powder. After manufacturing both sets of tablets were equilibrated in the room conditions for six hours measuring the change at various time intervals. Both sets had an increase in weight (from moisture pickup) leveling off after five hours. They also had an increase in tablet thickness and diameter compared to tablets that were made with fresh powder and tested immediately. The tablets made with fresh powder and then exposed to the environment had twice as much change compared to powder that had already pickup up moisture as shown in **Figure 10**. Both sets also had a decrease in tablet hardness measured at the end of the six hour hold time, with the fresh powder experiencing 4x reduction compared to humidified powder (19.1% vs 4.9% decrease in hardness). The tablets manufactured with humidified powder had less change over time than the tablets made with fresh powder samples. For this reason, the experiments were performed with fresh powder and the tablets tested immediately after compression.

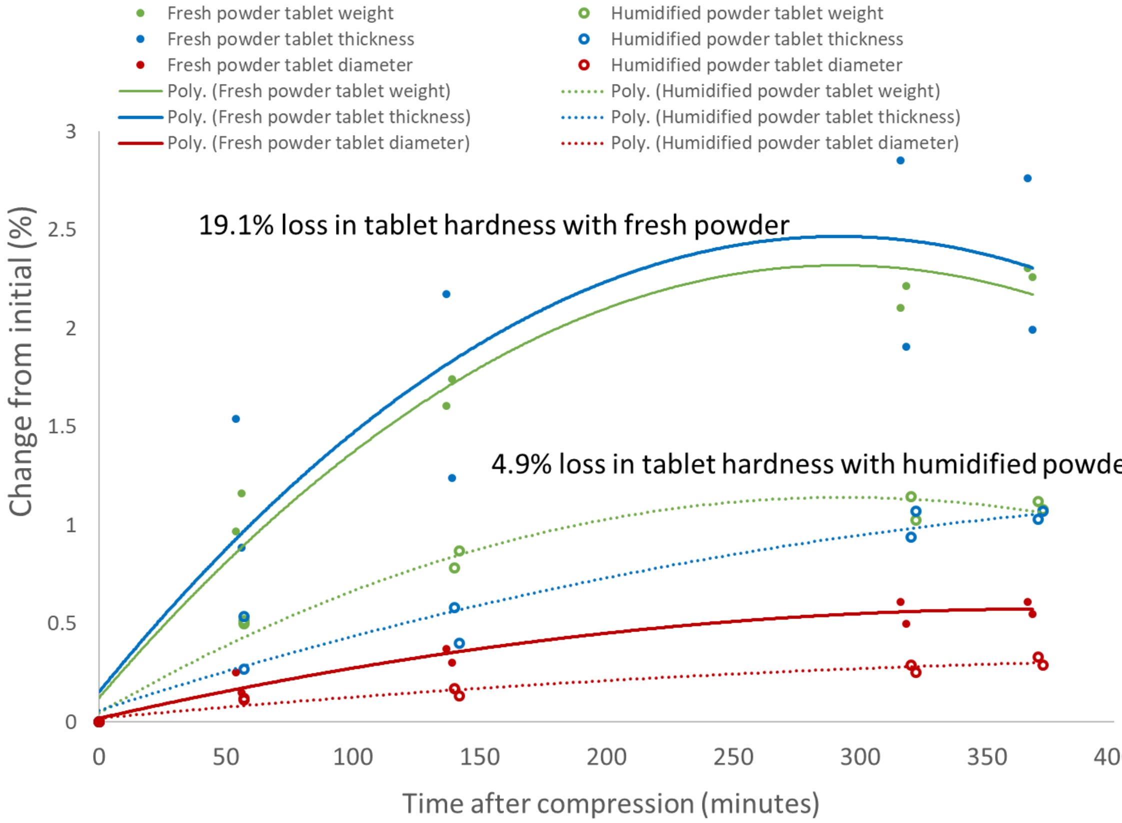

Figure 10 Impact of tablet exposure to room environment over time for HPMC K15 DC using fresh powder and pre-exposed humidified powder. Solid markers and lines for tablets manufactured using fresh powder and open markers with dashed lines for tablets manufactured with powder that had previously been exposed to the room environment for 24 hours. Blue for change in tablet thickness, green for change in tablet weight, and red for change in tablet diameter. All changes are the absolute value.

Both the K100M CR and K100M DC were tested for changes in tablet properties over a two hour hold time. Both sets of tablets had an increase in weight from absorbed moisture of approximately one percent with an increase in variability after two hours as shown in **Table 8**. The tablets also had an increase in thickness and diameter after two hours as shown in **Figure 11** and **Figure 12**. It is common for tablets to relax after compression with dimensional changes, but as they also increased in weight over that time it was not possible to differentiate the time and the moisture impact. To avoid the impact of moisture and time, the tablets were tested for weight, thickness, diameter and hardness immediately after compression for the remaining experiments.

Table 8 Change in tablet weight over two hours (n=20 tablets each).

Grade Type	Description	Mean Tablet Weight (mg)	Standard Deviation (mg)	Mean Weight Increase after 2 hours (%)
K100M CR	Tested Immediately	200.9	0.8	-
K100M CR	Tested after 2 hours	202.8	1.9	1.0%
K100M DC	Tested Immediately	201.9	0.8	-
K100M DC	Tested after 2 hours	204.3	1.6	1.2%

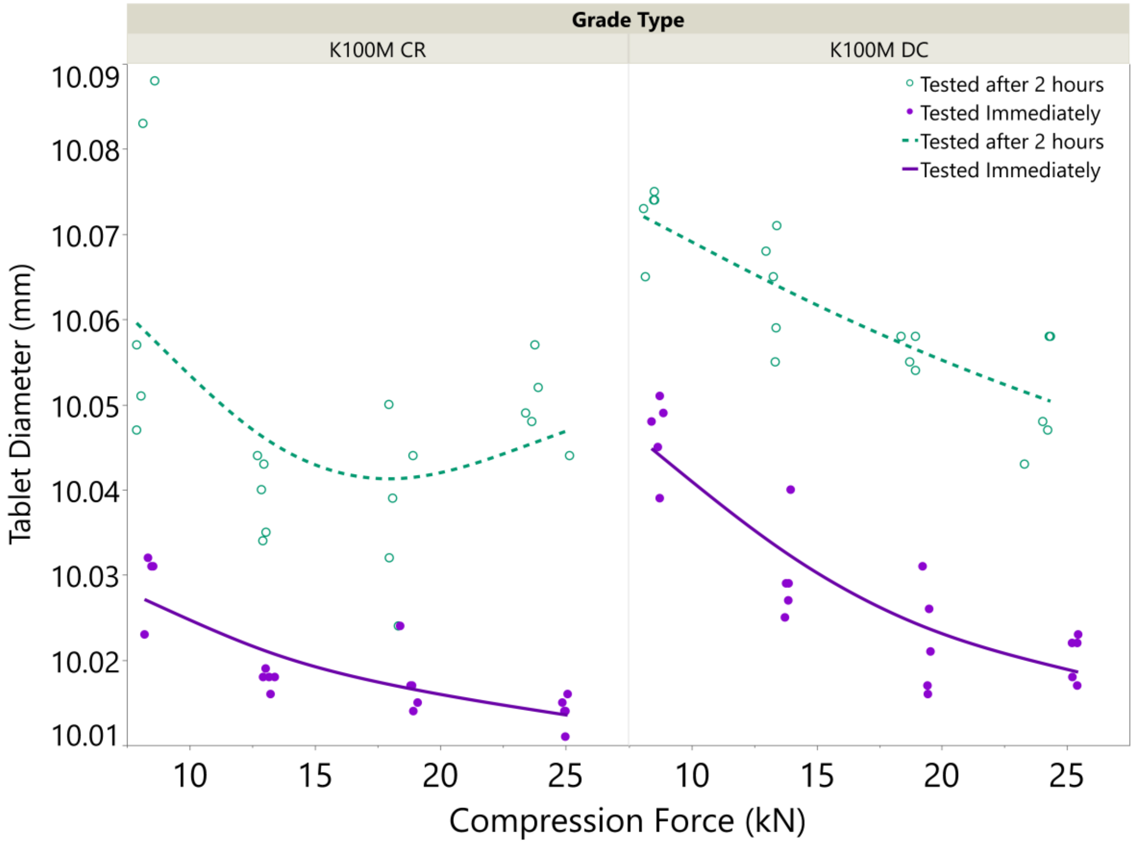

Figure 11 Tablet diameter change after two hours exposure to the room environmental conditions with K100M CR on the left and K100M DC on the right. Tested immediately in purple with solid circles and tested two hours later in green with open circles.

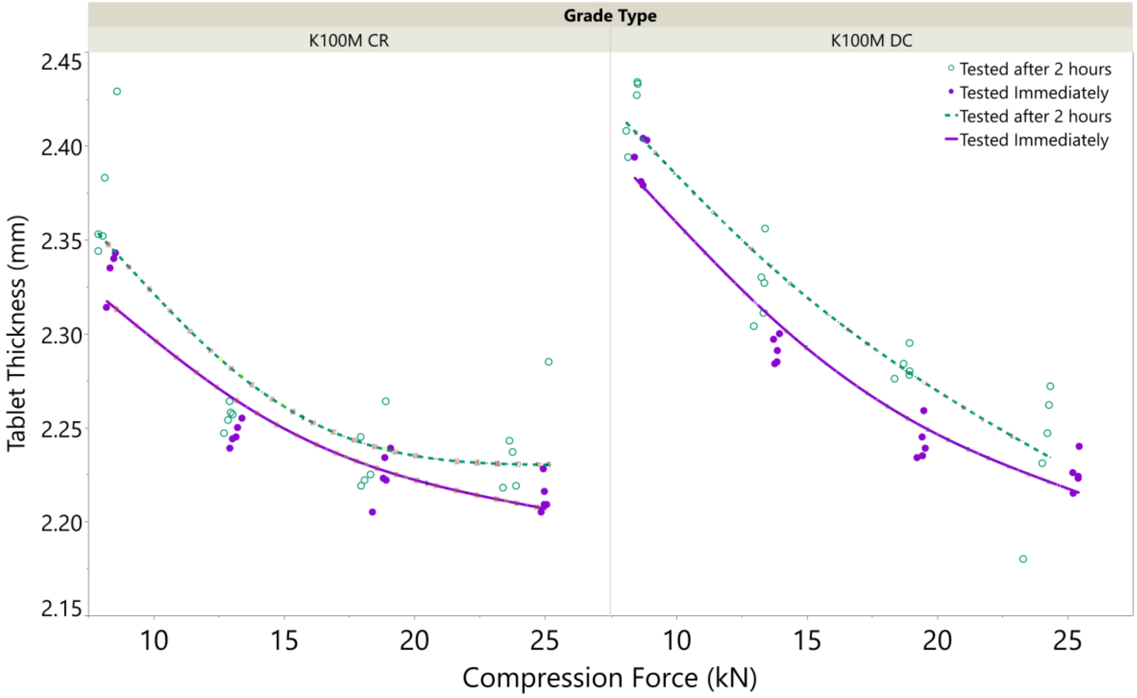

Figure 12 Tablet thickness change after two hours exposure to the room environmental conditions with K100M CR on the left and K100M DC on the right. Tested immediately in purple with solid circles and tested two hours later in green with open circles.

3.7 Compaction Studies

One important aspect of an excipient meant for use in direct compression is the ability to form a tablet with sufficient strength to withstand either the subsequent coating process or packaging and shipping in order to ensure that the tablet contains the desired dose of the drug for the patient. This is especially important for HPMC based controlled release tablets where maintaining the tablet integrity is critical because the tablet controls the release of the drug in the body. Even if both halves of a broken tablet are administered it is likely that the release rate will be affected due to an increased surface area the drug may be released more quickly. HPMC is the rate controlling polymer for hydrophilic matrix tablets and is commonly used in percentages of 10-30% of the formulation (98, 99) but can be used up to 80% or higher (100) making the powder properties of HPMC important.

Since all of the tablets were weighed by hand before compression they had very good weight control for both sets (n=120 tablets each) with low standard deviation. The mean tablet weight of the CR tablets was 201.1 ±1.6 mg and the DC type was very similar with the mean weight at 201.4 ± 1.5 mg. The results from the compression experiments are shown in **Table 9**.

Table 9 Tablet weight, thickness and diameter along with the compaction pressure and tablet tensile strength. Mean and (standard deviation) shown for n=10 tablets.

Grade Type	Tablet Weight (mg)	Tablet Thickness (mm)	Tablet Diameter (mm)	Compaction Pressure (MPa)	Tensile Strength (MPa)
K100M CR	199.6 (2.2)	2.324 (0.023)	10.031 (0.003)	25.9 (1.2)	3.28 (0.19)
	200.3 (1.0)	2.239 (0.012)	10.017 (0.002)	42.0 (0.6)	4.34 (0.26)
	200.5 (2.1)	2.211 (0.025)	10.014 (0.005)	59.7 (1.6)	4.79 (0.20)
	201.0 (1.6)	2.204 (0.017)	10.011 (0.004)	79.1 (1.3)	5.07 (0.27)
K100M DC	201.7 (1.1)	2.394 (0.009)	10.044 (0.004)	27.5 (0.5)	2.26 (0.14)
	201.7 (0.8)	2.284 (0.010)	10.029 (0.004)	43.6 (0.6)	3.42 (0.12)
	201.7 (0.8)	2.236 (0.012)	10.020 (0.005)	61.0 (1.0)	4.51 (0.27)
	199.6 (2.2)	2.203 (0.027)	10.021 (0.003)	78.4 (2.5)	4.97 (0.23)
K15M CR	202.3 (1.1)	2.417 (0.031)	10.035 (0.008)	29.1 (0.6)	2.65 (0.33)
	201.7 (1.3)	2.322 (0.021)	10.026 (0.005)	45.0 (0.9)	3.43 (0.33)
	201.5 (1.0)	2.289 (0.013)	10.021 (0.006)	62.1 (0.6)	3.76 (0.17)
	201.1 (1.6)	2.270 (0.017)	10.022 (0.004)	80.1 (0.9)	4.02 (0.17)
K15M DC	201.5 (1.5)	2.404 (0.008)	10.049 (0.011)	27.3 (0.4)	2.31 (0.23)
	201.2 (1.7)	2.297 (0.011)	10.032 (0.005)	43.2 (0.8)	3.43 (0.30)
	201.5 (1.9)	2.242 (0.014)	10.023 (0.005)	60.1 (2.5)	4.53 (0.36)
	201.5 (0.9)	2.227 (0.013)	10.019 (0.005)	79.6 (0.7)	5.22 (0.36)
K4M CR	201.6 (1.0)	2.505 (0.009)	10.048 (0.003)	29.5 (0.5)	1.99 (0.14)
	200.4 (1.6)	2.369 (0.017)	10.030 (0.005)	44.0 (0.9)	2.86 (0.25)
	201.5 (2.0)	2.328 (0.013)	10.020 (0.004)	61.5 (0.9)	3.33 (0.29)
	201.1 (0.8)	2.316 (0.009)	10.020 (0.004)	79.5 (0.5)	3.38 (0.19)
K4M DC	202.4 (0.9)	2.402 (0.007)	10.046 (0.004)	27.4 (0.2)	2.52 (0.17)
	202.1 (0.9)	2.287 (0.010)	10.031 (0.002)	43.0 (0.7)	3.72 (0.13)
	201.6 (1.0)	2.238 (0.008)	10.023 (0.005)	60.0 (0.9)	4.59 (0.11)
	201.0 (1.7)	2.211 (0.020)	10.018 (0.003)	78.0 (1.5)	5.19 (0.21)

Tabletability describes the powder's tableting performance by looking at the increase in tensile strength that is gained by the powder when it is compacted into a tablet at increasing pressures (101). The DC type HPMCs had very consistent profiles where a similar compaction pressure was required to produce tablets with similar tensile strength as shown in **Figure 13**. The CR types had significantly different tabletability profiles between the types with K100M CR > K15M CR > K4M CR. K4M CR required the most compaction pressure to reach a target tensile strength and the strength did not increase over 60 MPa. The K100M CR made stronger tablets at low compaction pressures compared to the DC types but was similar at higher pressures which are typically used in manufacturing. Overall, the DC types had more similar profiles and performed better compared to the K4M CR and K15M CR.

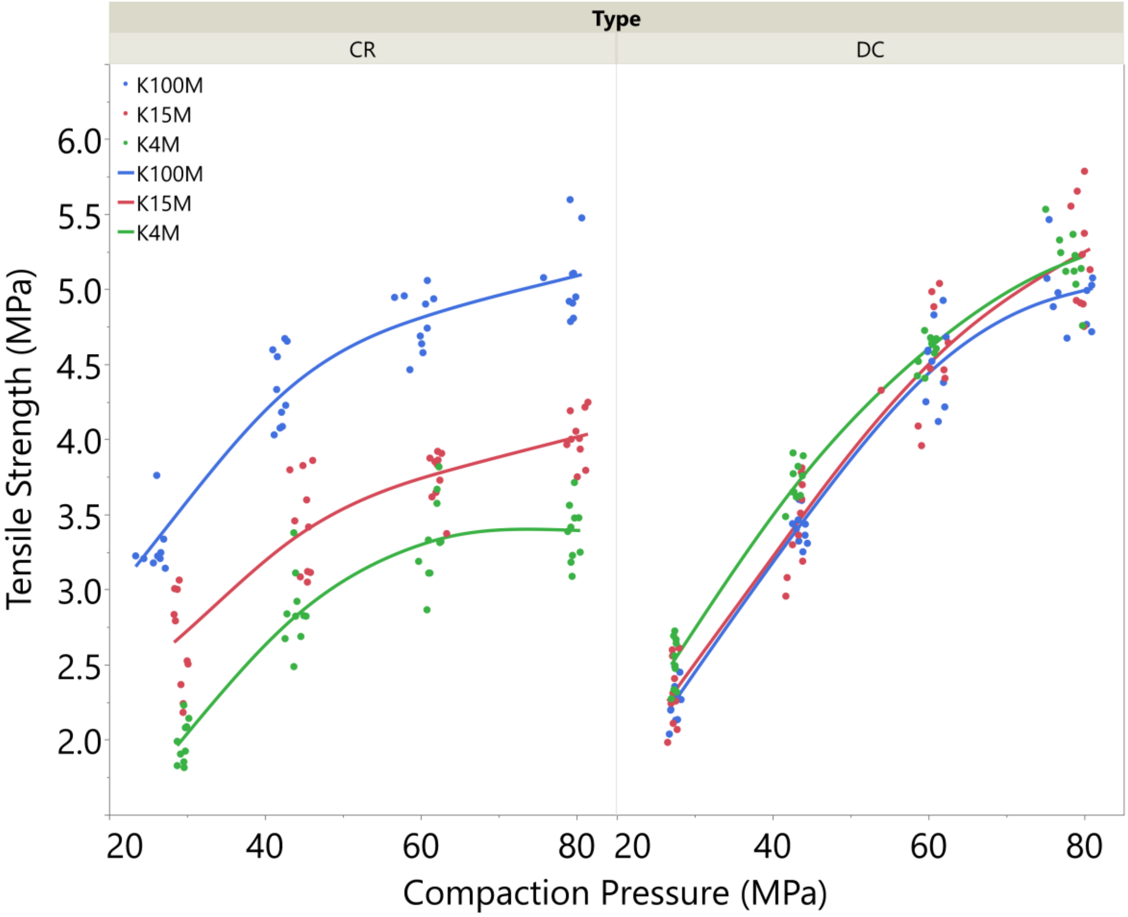

Figure 13 Tabletability of HPMC with CR type on the left and DC on the right. HPMC K4M in green, K15M in red, and K100M in blue.

The compressibility of a powder describes the relationship between the tablet solid fraction (1-porosity) and the compaction pressure. As the pressure increases the porosity decreases resulting in a larger bonding surface area in the tablet and stronger tablets (higher tensile strength) which tends to level off at higher pressures. It is preferred to have materials that can reach a target porosity and tensile strength at lower pressures to accommodate the high speed tableting process in commercial manufacturing. Materials that need to be compressed at high pressures can lead to increased wear and breakage of the tooling and tablet press used to manufacture the tablets. It is also desirable for tablets to achieve at least 0.85 solid fraction (79, 80) and not reaching the maximum achievable solid fraction so there is some room for variability in materials. **Figure 14** shows the compressibility for the HPMC. In this regard the CR type performed better only for the K100M grade while the DC types performed better for K15M and K4M.

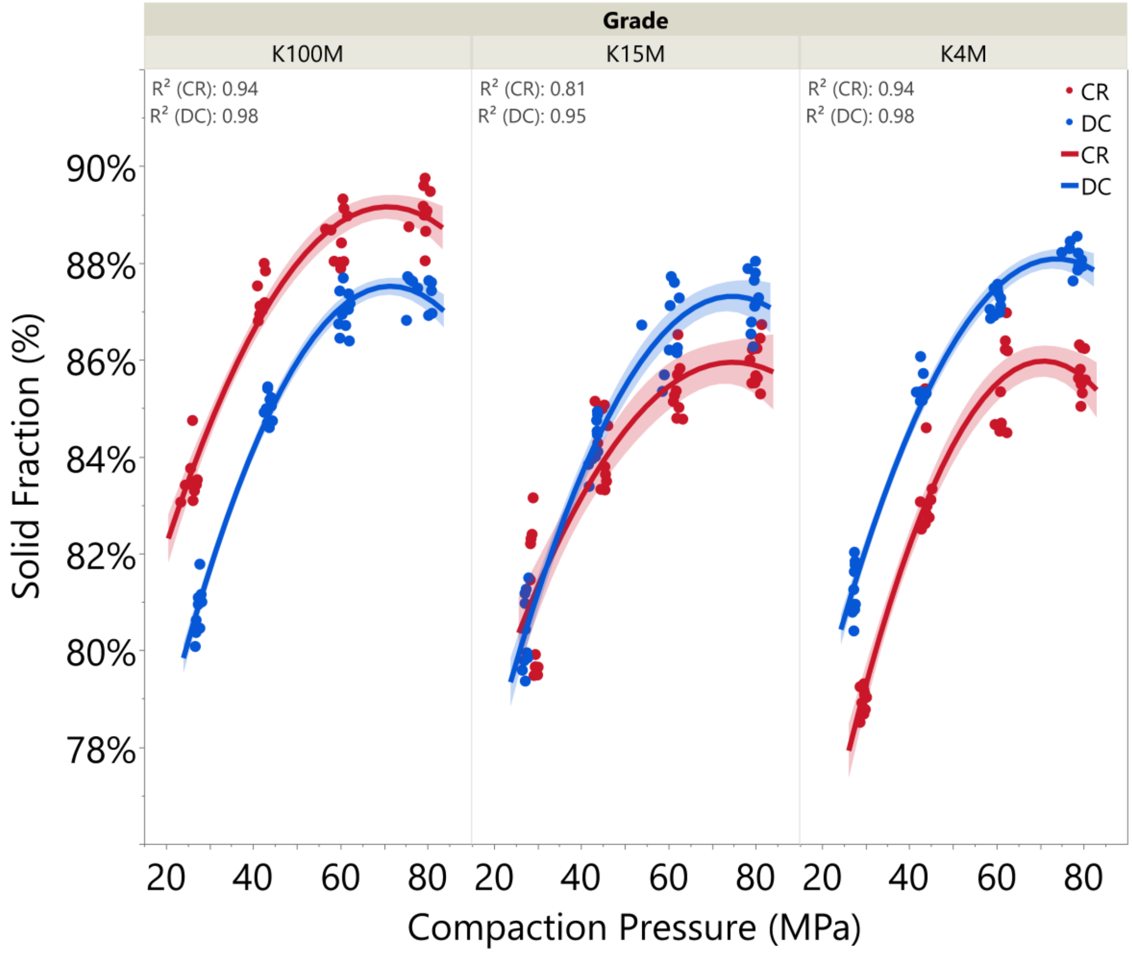

Figure 14 Compressibilty of HPMC. Quadratic fit with 95% confidence levels for the line fit shown. CR types in red and DC types in blue. K100M on the left, K15M middle, and K4M on the right.

Powder compactability describes the relationship between a tablet's tensile strength and the tablet porosity or solid fraction (SF = 1 - porosity) giving insight into the bonding strength of the powder. When comparing materials at the same porosity if one has a higher tensile strength then it has higher bonding strength of the material. The DC types all had higher compactability at higher solids fraction compared the CR types as shown in **Figure 15**.

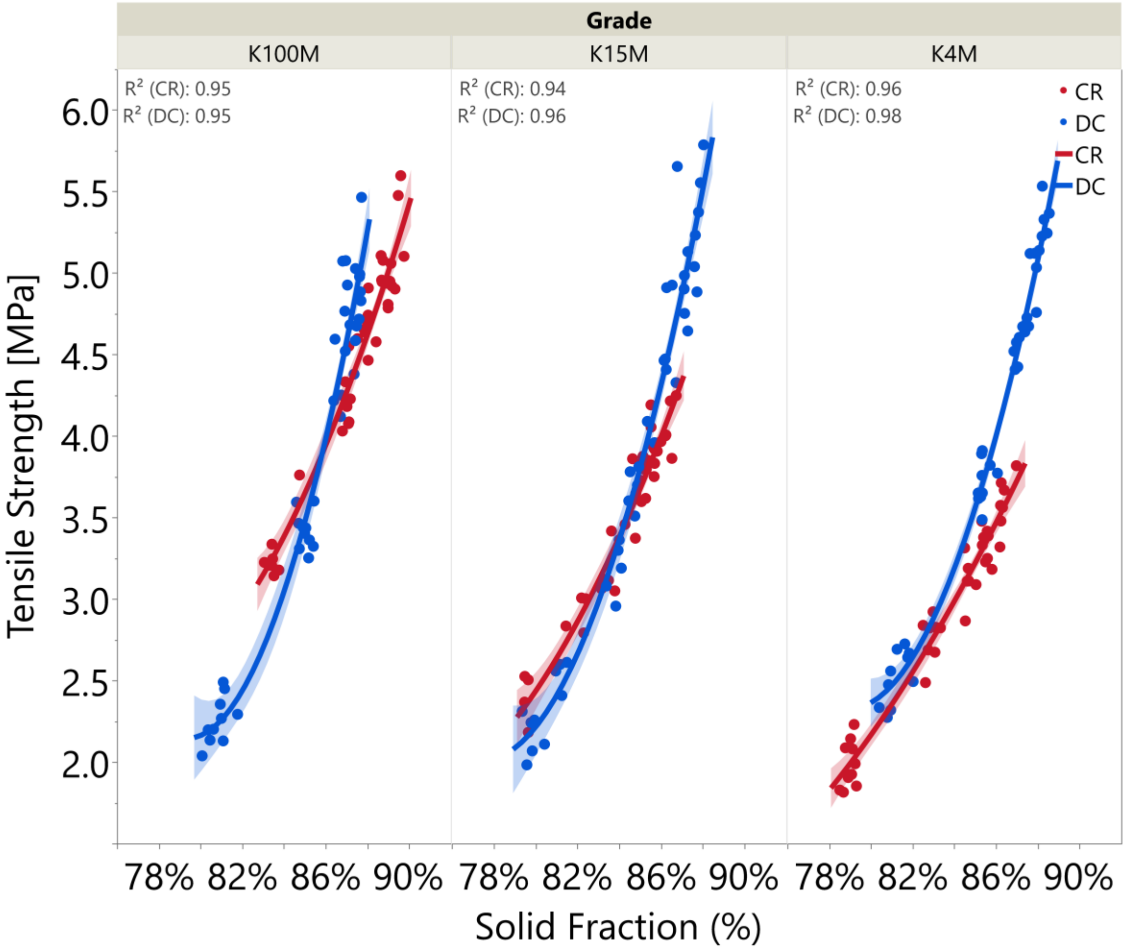

Figure 15 Compactability of HPMC. Quadratic fit with 95% confidence levels for the line fit shown. CR types in red and DC types in blue. K100M on the left, K15M middle, and K4M on the right.

4 CONCLUSIONS

The bulk densities for the DC grades were slightly higher and more consistent across the different grades than the CR ones for all of the different methods of testing bulk density. The true density also showed a slight increase for the DC grades and should be taken into consideration when performing tablet compaction analysis such as Heckel plots which utilize the material’s true density.

The particle shape of long, fibrous particles was consistent between the DC and CR grades of material, as well as within the grades, as could be seen with the SEM images. The aspect ratios were almost identical providing more evidence for the shape similarities. The DC material appeared to have a slightly smoother surface with fewer inclusions under the higher SEM magnifications. While this is a subjective measure, it is possible that the smoother surface contributes to improved flow via reduced inter-particle friction and reduced inter-particle locking.

Similar to particle shape, the particle size was also very consistent within grades with the DC material being slightly smaller in size (9-20 µm for D_{50}) when compared to the standard CR grades. While particle size has been shown to contribute to powder flow when other properties are kept the same it is typical for larger particles to flow better which is contrary to these findings. This small difference in particle size is unlikely to contribute significantly to the overall powder flow differences.

One unexpected difference in the materials was the specific surface area as measured by volumetric gas adsorption. Since the materials had similar particle size, shape and morphology it was expected that they would have similar surface area. Instead, it was found that the DC grades had surface area results that were three times that of the respective CR grades. This difference is likely due to the incorporation of a very small amount of silicon dioxide into the DC grade material. Silicon dioxide has a very high surface area and a similar effect was observed with microcrystalline cellulose.

The most important characteristic to the direct compression grades of HPMC is improved flow of the powder. Due to the poor flow of the standard CR grades of HPMC formulations typically require a granulation step. With improved flow of the DC grades these formulations may be feasible to avoid the granulation step and use the material in a direct compression process. This has the advantage of reducing the complexity of the process and decreasing the manufacturing cycle time. Multiple characterization techniques were utilized to further explore the flow characteristics of the powders. As shown in the powder flow summary table in **Table 10**, the DC grades of HPMC performed better in a majority of the powder flow tests.

The most significant differences were observed in the FT4 flow rate index, the avalanche testing for the time between avalanches and the total number of avalanches, and the shear cell uniaxial compressive strength and flow function coefficient. These test result indicate that the DC grades had significantly better flow than the standard grades.

Table 10 Overall powder flow summary and ranking for powder flow. Direct Compression (DC) in blue and Standard (CR) in red

	Carr's Index	Erweka Flow (g/s)	Flow Rate Index	Mean Avalanche Time (sec)	Avalanche Scatter	Maximum Avalanche Time (sec)	Number of Avalanches	Uni-axial Compressive Strength (Pa)	Flow Function Coefficient
↑ Better Flow	K100 DC	K4 DC	K100 DC	K4 DC	K4 DC	K4 DC	K4 DC	K15 DC	K15 DC
	K15 DC	K100 DC	K15 DC	K100 DC	K100 DC	K15 DC	K100 DC	K100 DC	K100 DC
	K4 DC	K15 DC	K4 DC	K15 DC	K15 DC	K100 DC	K15 DC	K4 DC	K4 DC
	K15 CR	K15 CR	K100 CR	K4 CR	K4 CR	K100 CR	K4 CR	K4 CR	K4 CR
	K4 CR	K4 CR	K4 CR	K100 CR	K100 CR	K4 CR	K100 CR	K100 CR	K15 CR
	K100 CR	K100 CR	K15 CR	K15 CR	K15 CR	K15 CR	K15 CR	K15 CR	K100 CR

There were two flow tests which did not follow the trend and seemed to indicate that the CR grades had better flow. Both of these were part of the FT4 powder rheometer testing and shown in **Table 11**. The specific energy (SE) is not a direct measure of powder flow and is related to the energy to lift an unconfined powder. All of the powders were classified as having moderate flow. The SE values were marginally higher for the DC grades compared to their CR counterparts. The basic flowability energy (BFE) is also an indirect measure of powder flow. It measures the energy to move the testing blade through a loosely packed powder and was more than double for the DC grades. For both of these tests it is possible that the higher bulk density of the DC grades along with the fiber-like shape exhibited more mechanical interlocking and friction providing more resistance to the impeller movement. This phenomena has been observed with other materials (74). This highlights the challenges with trying to characterize powder flow which can be very dependent on the conditions, and this is why multiple techniques are recommended to be utilized.

Table 11 Overall powder flow summary for FT4 measurements that did not follow the typical trend for powder flow. Direct Compression (DC) in blue and Standard (CR) in red.

↑ Lower Values

BFE (mJ)	Specific Energy (mJ/g)
K4 CR	K4 CR
K15 CR	K15 CR
K100 CR	K4 DC
K4 DC	K100 CR
K15 DC	K15 DC
K100 DC	K100 DC

Overall, the materials exhibited similar characteristics with improved flow for the DC grade which should allow for better performance in direct compression applications over the standard CR grades of HPMC. As the polymer chemistry has not been changed between the CR and DC type within each polymer viscosity grade and the materials have retained very similar particle size and shape, the dissolution performance is not expected to be affected. The significant differences in the surface area are attributed to the inclusion of silicon dioxide and not differences in the HPMC itself and not expected to affect the dissolution. The dissolution of the DC grades have been evaluated and shown to be similar to their CR counterparts (102). During development the type and amount of HPMC is always evaluated and optimized to achieve the desired dissolution rates such that the DC grade can be substituted where better flowing material would have an advantage.

The potential for moisture uptake in the powder and tablets and resulting impact to the tablet properties necessitated controls around weighing, compression and testing to avoid confounding the testing results. It was necessary to mix the material before weighing out a sample for compression and then each tablet was tested immediately after compression in order to have a direct comparison of the materials without the results being confounded by changes caused by moisture.

The CR types had significantly different tabletability profiles between the grades with K100M CR > K15M CR > K4M CR. The compaction profile reached a maximum for K4M CR where adding more compaction force did not result in an increase in the tensile strength. The K100M CR made stronger tablets at low compaction pressures compared to the DC types but was similar to the DC grades at higher pressures that are common for commercial manufacturing. Overall, the DC types had similar tabletability profiles between the three grades and performed better compared to the K4M CR and K15M CR grades. These differences are related to the difference in the material compressibility. At the same compaction pressure the K100M CR had a higher solid fraction compared to the

K100M DC while DC performed better for K15M and K4M. A higher solids fraction leads to increased bonding in the tablet if all other factors are equal, but from the compactability curve the DC types gave higher tensile strength at higher solids fraction indicating the bonding for the materials was slightly better for the DC types. This is beneficial for direct compression applications where the materials are not granulated prior to compression. There can be a trade off with improving the flowability of a material and ensuring sufficient tabletability which was shown to be the case with a different supplier's version of DC HPMC (103, 104) so even keeping the tabletability the same would have been beneficial.

CHAPTER 2 LOSS IN WEIGHT FEEDING, POWDER FLOW AND ELECTROSTATIC EVALUATION FOR DIRECT COMPRESSION HYDROXYPROPYL METHYLCELLULOSE (HPMC) TO SUPPORT CONTINUOUS MANUFACTURING

1 BACKGROUND

There has been significant progress made towards implementing continuous manufacturing for pharmaceutical products in research, equipment, process understanding and modeling to support its implementation. Some of the major benefits of continuous manufacturing include reduced variability, increased monitoring, improved quality, eliminated process scale-up, reduced risk of human errors, smaller physical space requirements, reduced operating costs, increased equipment utilization, improved controls, and potential to utilize modeling for process control or material diversion (22, 105). Initially, continuous processing was proposed for high volume products that were already on the market, but initial regulatory approvals have focused on smaller volume new products. Continuous manufacturing techniques have been successfully applied to chemical synthesis for Active Pharmaceutical Ingredients (API), biologics and most frequently for small molecule drug products where equipment has been designed and integrated to support various processes such as wet granulation, dry granulation, melt extrusion, compression and encapsulation. Some of these systems have been very complicated in design such that different processing modules can be inserted depending on the desired type of manufacturing, while others are designed for a specific process.

Direct compression is one area that has gained increased attention as a result of continuous manufacturing. This resurgence in interest can be attributed to the combination of advantages offered by Continuous Direct Compression (CDC) processes over batch processes, new excipients designed specifically for direct compression, and increased focus within the material science field aimed at API modifications and co-processing to improve the physical characteristics of the API and make it more amenable to direct compression. Historically, direct compression was not seen as being as robust compared to other granulation processes since it can lack processing (106), has the potential to be more impacted by variability in the raw materials (excipients and API), and prone to issues with segregation and poor flow (107).

Batch processes have had limited success in using direct compression. One of the main challenges is the potential for segregation of the API with the excipients. Due to particle size, shape, density, and other particle property differences between the API and excipients there can be difficulty in achieving a homogeneous mixture with a high propensity for the materials to segregate when flowing/transferring between equipment or during storage. This is one of the reasons that agglomeration or granulation processes such as wet granulation or roller compaction are applied. CDC processes avoid this obstacle by only processing small amounts of material in the system at any given time with minimal transfer distance between the feeders, blenders, and tablet press. CDC processes have even been shown to be viable for low dosage formulations (108).

Additional challenges for direct compression are the poor flow and compactability of most APIs and some excipients. Both of these issues can be addressed through particle engineering approaches such as API and excipient coprocessing and excipient modifications for direct compression (109-111). Excipient manufacturers have recognized the necessity and there are now several excipients designed specifically for direct compression processes (112-114).

A key challenge with continuous manufacturing is the need to feed excipients and API accurately using loss-in-weight (LIW) feeders (115). Feeding powder consistently and continuously ensures that products are manufactured with reproducible and acceptable critical quality attributes and product quality (21, 40, 41, 116). If the feeding rate of one ingredient varies from the set point for even a short period of time, or if there is a spike in material due to accumulation in any part of the system, the resulting variability in concentration could produce out of specification material downstream (117). Blenders are incorporated in the continuous manufacturing line and can offset some degree of feed variability (118), but if the process shifts from acceptable ranges it results in material rejection via the control system, impacting the overall yield or causing the continuous process to stop for correction. Many studies of LIW feeders have not sufficiently evaluated the impact of feeder refills to the overall feasibility of feeding. This study outlines the powder evaluations and feeder studies necessary to understand the material addition aspect of the continuous process, highlighting the need to execute multiple refill cycles when performing feeding evaluations since the refill process can be impacted with cohesive materials.

Particle triboelectric charging (electrostatics) is a physical effect frequently ignored but can occur with pharmaceutical powders and APIs (119-121). Factors which influence powder charging can be: type of surface material, contact area, surface roughness, surface cleanliness, chemical structure, absorbed moisture, particle size distribution, shape, roughness, crystallinity and surface area. Even environmental conditions such as contact time, temperature, and relative humidity can influence triboelectric charging (119, 121-123). Whenever particles are in contact amongst themselves or processing equipment, there is potential for charging to occur. This can happen during many different powder processing and handling operations. Specific situations include shipping in polyethylene bags, weighing with stainless steel or plastic scoops, screening/sieving, pneumatic conveying, mixing, milling, spray drying, and any transfer operations where the powder flows through tubes or out of bins or hoppers (124-129). During these processes, triboelectric charging of the particles can take place when materials contact each other through friction, sliding or impact and then separate from each other (130, 131). The time for these charges to dissipate, especially at large scale, has not been well studied and some materials like magnesium stearate continue to hold the charge even after grounding (132-134).

Triboelectric charging can have positive effects such as enhancing API blend uniformity via adhesion to larger carrier particles (135-138) but it can also disrupt pharmaceutical processes. It can impact agglomeration and the potential for jamming and segregation (139-143), punch sticking on tableting (144), die filling/ weight uniformity during tableting (145), and even general powder adhesion onto many surfaces (120). Adhesion issues due to electrostatics is often addressed in analytical testing (wet chemistry) but can also be very problematic for PAT applications relying on sensor surfaces that can become fouled if particles adhere to the window of the sensor. The triboelectric charging of some HPMC materials have been evaluated (146, 147) but the DC grades and the impact to LIW feeding have not been investigated previously.

Powder flow can impact the continuous blending of materials in various continuous mixing systems (148, 149) and the most difficult aspect of continuous mixing is the feeding of materials (150). This study will evaluate the impact of powder flow and electrostatic charge on LIW feeding systems which utilize a mass flow feedback loop to keep material fed at a set point.

2 Materials and Methods

2.1 Materials

Six different Benecel^{TM} Hypromellose lots (Ashland Inc. Wilmington, DE) consisting of three CR grades of HPMC K100M, K15M, K4M and three DC grades of HPMC K100M, K15M, K4M. Material properties for the six materials are provided in **Table 12**. These materials were previously characterized in **Chapter 1: Characterization of a novel hydroxypropyl methylcellulose (HPMC) direct compression grade excipient**.

The standard grades are referred to as controlled release (CR) grades by the manufacturer as they were the first improvements to HPMC for use as an excipient. The ‘K’ defines it as a Hypromellose 2208 type, which indicates a specific range of ratios of hydroxypropyl and methoxy group substitutions. This ratio determines the overall performance of the HPMC in hydrophilic matrix systems. K-chemistry HPMC has the highest ratio of hydroxypropyl to methoxy substitution allowing for fast gel barrier formation beneficial for controlled release tablets. The fast rate of hydration followed by quick gelation is required for the polymer to form a protective gelatinous layer around the matrix to modulate the release of the drug. This evolving gel layer develops into the tablet over time to control drug release, preventing the tablet from immediately disintegrating and is especially critical with water-soluble drugs and water-soluble excipients (1, 12, 63). The 'M' indicates viscosity x1000 (e.g. K100M = viscosity of 100,000 mPa*S). These grades represent a range of viscosities commonly employed for controlled released hydrophilic matrix tablets and are currently the only grades available as DC types. The DC grades are co-processed with silica at <1% w/w to improve flow and compactability, which results in better performance than direct blends of HPMC with silica (151).

Table 12 Benecel™ Hypromellose lots and properties used in this study. Data provided by Ashland, Inc.

HPMC Material Grade	Abbreviated as	Weight Average Molecular Weight	Nominal Viscosity of 2% solution (mPa*S)
Benecel K100M PH CR	K100M CR	1,000,000	75,000 - 140,000
Benecel K15M PH CR	K15M CR	575,000	13,500 - 25,200
Benecel K4M PH CR	K4M CR	400,000	2,700 - 5,040
Benecel K100M PH DC	K100M DC	1,000,000	75,000 - 140,000
Benecel K15M PH DC	K15M DC	575,000	13,500 - 25,200
Benecel K4M PH DC	K4M DC	400,000	2,700 - 5,040

2.2 Powder Flow Characterization

These materials were previously characterized in **Chapter 1: Characterization of a novel hydroxypropyl methylcellulose (HPMC) direct compression grade excipient** for many different particle properties such as size, morphology and especially for powder flow, which can be difficult to evaluate as flow dynamics can change under different conditions (152). This work utilized different testing methodologies such as static angle of repose, automated powder flow in a drum across different speeds, and tapped density measurements after each tap to characterize the powder flow. The powder electrostatics were also explored for the first time for the DC HPMC materials which was found to impact the feeder studies.

2.3 Static Angle of Repose

The angle of repose is a common method to evaluate granular materials with varying techniques for estimation and measurement (153). The challenge with cohesive powders is that they form irregular heaps which makes it particularly difficult to measure the angle of repose accurately compared to non- cohesive powders that form well defined heaps with consistent angles on all sides (154). The angle of repose test can be very sensitive to the method and handling used to create the heap. For this reason, the GranuHeap instrument (Granutools, Awans, Belgium) was used to measure the angle of repose of the cohesive HPMC.

The instrument consists of an automated method to create the heap along with multi-angle image analysis. Calibration consisted of measuring a 45° calibration piece. Then the initialization tube was filled with 100 ml of powder and the measurement started. The initialization tube has an internal diameter equal to the support plate and lifts slowly at a speed of 5 mm/s. The powder flows from the initialization tube to form a heap on the cylindrical test plate and the system uses a CCD camera to capture 16 images during a slow, controlled rotation of the test plate to view different heap orientations so that any asymmetric heap shapes are recorded.

The test was performed in triplicate for each material. After each test the equipment was cleaned, and a fresh sample was used for each test. The software was used to perform image analysis of the air-powder interface and provided the angle of repose for each image which is quantified as the angle of an isosceles triangle with the same surface area of the actual heap. Generally, the lower the angle of repose the better flowing the materials. The heap height is the height of the powder heap which is typically higher for more cohesive materials. The static cohesion index is derived from the difference between the measured heap interface and an ideal isosceles triangle. Non-cohesive powders will have a static cohesion index close to zero and as the heap shape deviates more from an isosceles triangle with cohesive powders, the static cohesion index increases (154).

All tests were performed with room conditions between 23.6 – 25.1°C and 34.1 - 47.2% relative humidity. The tests were alternated between samples of CR and DC to reduce any bias from environmental conditions.

2.4 Flow Angle and Cohesive Index

The GranuDrum (Granutools, Awans, Belgium) was used for powder flow in a drum in order to determine the dynamic angle of repose for the materials. The equipment has a transparent 84 mm diameter drum that is filled with 50-55 ml of powder such that the drum was approximately half full. The drum was sealed and rotated at different speeds. The rotating drum was backlit and utilized a CCD camera to capture images of the powder flowing at speeds of 2–20 rpm (every 2 rpm) and then 20-60 rpm (every 5 rpm). Varying the speed of rotation allowed for more in-depth evaluation of powder flow to evaluate shear thinning or shear thickening behavior.

The powder was conditioned for 15 seconds and then images were taken every second such that 40 images were acquired at each of the 18 speeds. The software detected the interface of the powder/air and determined average angle and standard deviations for each velocity. The flowing angle was determined from the average angle measured at the center of the powder/air interface. The cohesive index is related to the powder cohesion and is evaluated from the temporal fluctuations of the powder/air interface. A non-cohesive, excellent flowing powder would have very low fluctuations and hence cohesive index close to zero while a highly cohesive powder would have more variability of the flow and a higher cohesive index. Each test was repeated using new samples and alternating between CR and DC materials to reduce testing bias. All measurements were made between 22.7-25.5°C and 40-49% RH.

2.5 Tapped Density

The automated GranuPack (Granutoools, Awans, Belgium) removes much of the inaccuracy with traditional tapped density tests where the measurements are estimated by eye using a graduated cylinder. The interpretation of the result is especially difficult for the initial measurement since the powder surface is very erratic after pouring powder into the graduated cylinder. The GranuPack instrument also provides more information around the progression of the density change over time by taking a distance measurement after every tap and not just the final value.

The test method consisted of adding approximately 11 g of sample into a grounded metallic initialization tube. Then the initialization tube was lifted at a slow speed of 1 mm/s such that the powder fell gently into a slightly larger (26 mm diameter) measurement tube to standardize the sample loading. A lightweight aluminum platen was then gently placed on the top of the powder with the help of a placement string. The measurement tube was lifted 1 mm and dropped, followed by an automatic measurement of the height which was repeated 1,500 times. Utilizing this methodology the evolution of the tapped density at each tap could be measured such that materials with similar bulk and final tap density might show differences in the settling of particles and the progression of the tapped density.

Each measurement was repeated a second time with new material after cleaning the test cell. All tests were performed with room conditions between 22.9 – 25.3°C and 39.3 - 47.3% relative humidity. The equipment automatically calculated the initial density, final tapped density, number of taps to get to half the final density (n½), Hausner ratio (final tapped density divided by initial density), and the extrapolated maximum density from tapping (ρ[∞]).

2.6 Electrostatic Charge Density / Triboelectric charging

Triboelectric charging of the powders was determined using a GranuCharge Instrument (GranuTools, Awans, Belgium). The equipment consists of a 700 mm long, 47 mm diameter V-shaped tube made of 316 L stainless steel where the powders become charged when flowing through the tube. The V-tube geometry combines the different mechanisms leading to tribo-electrification: (i) friction between the grains, (ii) friction between the grains and the wall, and (iii) impact of the grains on the wall at the connection between the two tubes where the powder changes direction (119).

Approximately 50 ml of the powder was weighed in a glass beaker and grounded to dissipate any charge. The powder was then poured directly into the Faraday cup to determine the initial charge. The Faraday cup was then cleaned and replaced. A new sample of 50 ml of powder was weighed, grounded and then fed into the testing tube using a vibratory feeder set at 25% vibration. The feeder and tubes were grounded before the measurement to replicate the grounding of processing equipment used in pharmaceutical manufacturing. After flowing through the testing tubes, the powder was collected into a Faraday cup and the final charge was measured. The measurements were repeated five times for each material. Charge density (nC/g) was then calculated by dividing the net charge by the mass of the material for the initial and final charges and the accumulated charge was determined as the difference.

All tests were performed between 23-26°C and 39-47% RH, alternating between CR and DC types to reduce any environmental bias. It has been demonstrated that powders have a material specific threshold to relative humidity, above which they show significant changes in the triboelectric charging (155). The GranuCharge equipment has the capability to test different humidification levels with the additional environmental attachment, but this aspect was not evaluated.

Additional testing was performed with HPMC K100M CR using tubes with different materials of construction commonly found in pharmaceutical manufacturing environments (316L Stainless Steel, Poly-Ethylene, Poly-Vinyl Chloride, Aluminum, and High Density Poly-Ethylene) to determine the charging effect with different contact materials using the same testing method as described. Single measurements were made for each material.

2.7 Compact Feeder Equipment

The GEA loss-in-weight compact feeder (GEA, Columbia, Maryland) was used for this study. This equipment is identical to the GEA Compact Feeders (CF) utilized in the GEA CDC-50 equipment designed for continuous direct compression and shown in **Figure 16**.

The GEA Compact Feeder uses a twin screw conveying system for powders with three different gear servos available depending on the targeted feed rate. There is also a horizontal impeller above the screws to prevent cohesive materials from bridging in the hopper, ensuring complete filling of the screws. The impeller rotates counterclockwise making one turn for every 8 turns of the screw. During normal operation the feeder uses gravimetric control where the load cell determines the mass flow, which is compared to the target value. The screw speed is then adjusted to keep the actual mass flow as close to the target as possible.

When the LIW feeder goes into volumetric mode it is the most susceptible to feeding errors because there is no feedback loop to keep the mass flow on target. The feeder will go into volumetric mode during a refill or when a perturbation occurs, such as scale disturbance, vibration on scales, or when there is feeding difficulty.

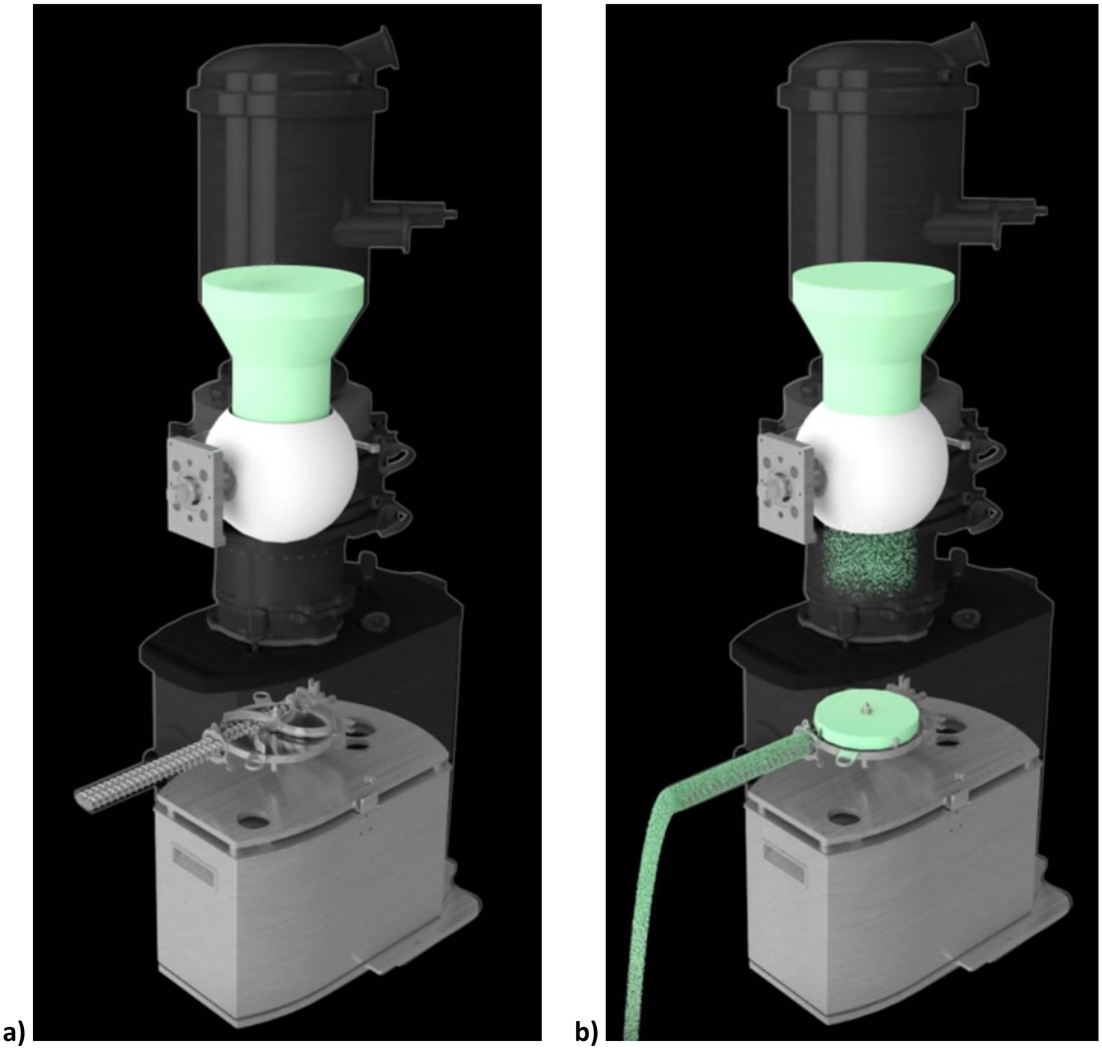

Figure 16 LIW feeder system. Diagram of GEA Compact Feeder module (GEA Group Düsseldorf, Germany) used for continuous manufacturing. **a)** Empty hopper with material in refill bowl **b)** Material being fed out of hopper and refill event initiating.

During a refill event it is necessary for the feeder to switch from a gravimetric feed rate (mass per time) to a volumetric (fixed speed based on feed factor array and the mass of material) because additional mass is added to the feeders. The refill is triggered when the feeder reaches a defined minimum mass setpoint (approximately 300 g was used for HPMC) at which point the feeder switches to volumetric feeding and the refill hopper rotates 180 degrees to dump additional powder into the hopper which typically takes 0.6 - 1.2 seconds. While the system uses gravity to empty the hopper there is vibration and the top up system is designed to come to a sudden stop once turned 180 degrees, causing a knock that assists in emptying the material. The feeder continues in volumetric mode to stabilize before switching back to gravimetric mode. In order to improve the accuracy during volumetric feeding, the system utilizes a feed factor array based on bins of different powder mass. The feed factor array is set using a calibration run and updated constantly during the run based on measured data. This ensures consistent mass flow during a refill and determines what screw speed should be used when exiting volumetric mode. The feed factor itself is a measure of the mass per revolution and is a factor of the total mass or head pressure from the material in the hopper. The higher the head pressure the more material is fed by the screws per revolution, and the higher the feed factor.

In order to evaluate the impact of refills for this study, material was fed such that the hopper was refilled at least three times for each material using the 1.2 L refill bowl. The refill bowl is available in 0.4, 0.8, 1.2 or 1.6 L sizes allowing for optimization of the refill. In some cases it is beneficial to provide for more frequent refills with less material

(156, 157). This provides for less variability in the head pressure and potentially more consistent feeding but also increases the frequency of refills and overall amount of time where the system is not running gravimetrically. For materials with poor flow and a tendency to rathole or bridge in the hopper or refill bowl it may be beneficial to use larger bowls, as the smaller bowls have smaller openings which could be more prone to bridging or clogging.

The screw feeder has different sized outlet screens that can be placed at the end of the screws to facilitate more consistent feeding. The size of meshes available are either 8 mm (open), 2 mm (coarse) or 1 mm (fine). Material is pressed between holes in the screen so that cohesive powders will fall off more reproducibly and it can also help with free-flowing powders to create some back pressure and moderate the flow. In some instances, the powders can be dosed with improved accuracy using a screen, but it is highly material dependent. For the HPMC materials even the large coarse screen created significant back pressure in the system which caused the screws to over torque and stop. As a result, no screen was used in these studies.

The importance of establishing the Residence Time Distribution (RTD) for continuous systems has been highlighted by many authors (41, 158-162). The RTD of the GEA Compact Feeder has been evaluated and shown to have good results (short RTD) compared to other loss-in-weight feeders (163). This is beneficial as it reduces the time for an excursion to pass through the system and results in less rejection of material. Determining the residence time for the materials in the entire continuous system will support determining an acceptable level of variation in the feed rate for each of the materials.

2.8 Loss in weight (LIW) feeding studies

Prior to the experiments, a full hopper was run completely empty while the software was in calibration mode in order to identify the low refill level and establish a feed factor (g/screw revolution) array. The refill level was chosen at the point slightly before the instantaneous mass flow RSD started to increase when the powder bed was running low. This equated to approximately 25% of the material remaining which was similar to other common pharmaceutical materials (104). Each of the materials was fed at three different feed rates, 1, 7.5 and 15 kg/h (equivalent to mass flows of 0.278, 2.083 and 4.167 g/sec). These rates were chosen to reflect the likely range of common production throughputs on the CDC-50 when using common amounts of HPMC in a formulation. The GEA CDC-50 has a typical low throughput of 10 kg/h and a nominal maximum throughput of 50 kg/h. HPMC is typically used at a concentration of 10-30% in modified release formulations, leading to the range of 1 kg/h (10% concentration at 10 kg/h throughput) and 15 kg/h (30% concentration at 50 kg/h throughput) with 7.5 kg/h as a center value. The gear box required for each feed rate is provided in **Table 13** along with the subsequent feeding parameter ranges.

The LIW feeder was set up with 20 mm screws and standard feeder paddles. No outlet screen was utilized on the feeder barrel output as even the largest screen resulted in excessive backpressure and equipment shutdown. During the feeder evaluations multiple refills were completed for each of the materials using the 1.2 L refill hopper. Data was logged at a rate of 0.2 seconds. The feeder emptied the powder directly into a collection container which was placed 9 cm below the feed screw outlet. All tests were conducted with room environmental conditions of 21-25°C and 28-39%RH. The feeder was set on a marble table with anti-vibration pads to eliminate external disturbances.

Table 13 Feeder setup and summarized feeding parameters.

Target Feed Rate (kg/h)	Mass Flow Setpoint (g/sec)	Gear Motor Used	Screw Speed (rpm)	Feed Factor
1	0.278	235:1	10.8-14.1	1.21-1.58
7.5	2.083	235:1	78.7-95.9	1.26-1.60
15	4.167	63:1	143.3-197.8	1.13-1.78

3 Results and discussion

Data was analyzed and graphed using software tools including Excel (version 2016), Minitab (version 19.2020.1), JMP (SAS version 13), and Spotfire (TIBCO Analyst Version 7.11.1 LTS).

3.1 Angle of Repose

Results from the GranuHeap indicated that the K100M CR grade had the highest static angle of repose followed by the K15M CR grade. The remaining materials were similar with the DC types all showing the lowest angles of repose. The static cohesion index and heap heights were also lower for the DC grades with the exception of K4M. Due to test variability most had high standard deviations which is common for cohesive materials as the heap is not uniform all the way around. All tests were performed in triplicate with 16 measurements made around the heap for each test. The average and standard deviations shown in **Figure 17** and **Table 14**. Both the angle of repose and heap height were statistically significant with the DC grades being lower indicating better flow overall, although the range of 56-65° is still considered poor flow (164). While the method is only a static measurement and may not be representative of flowing powders, the tests are easy and provide a quick evaluation of the powders.

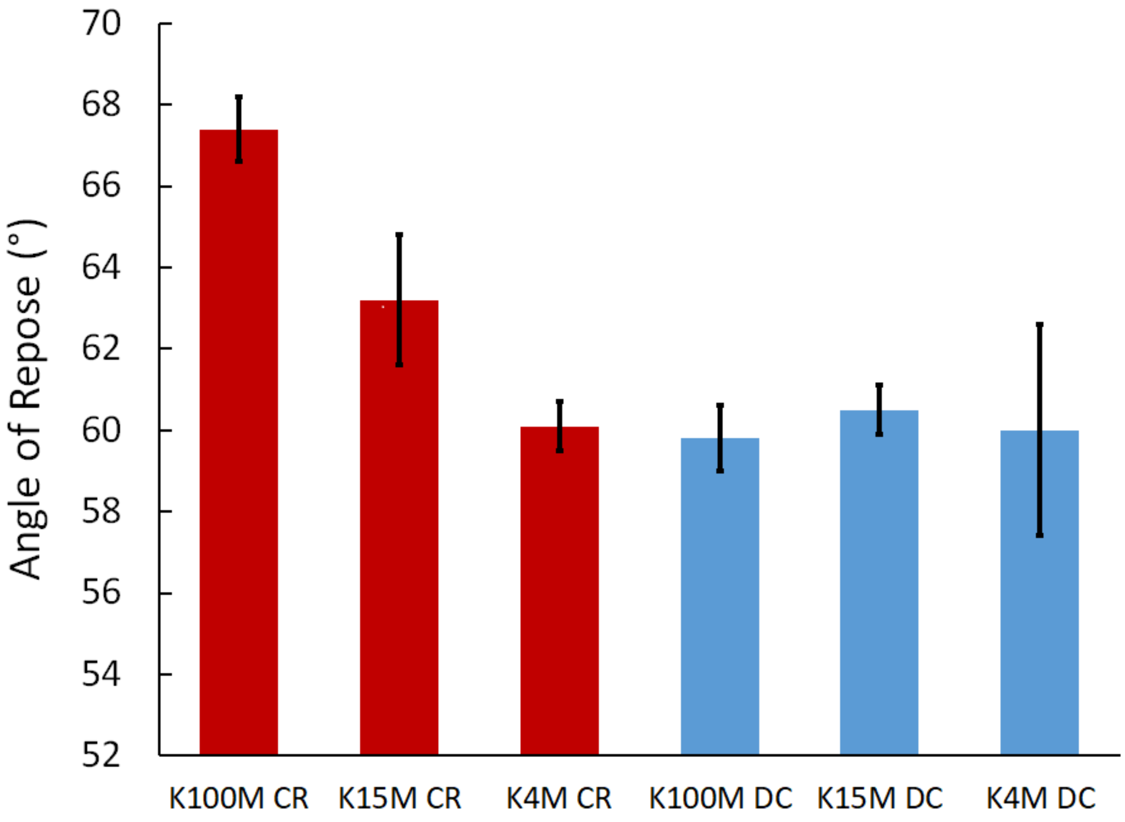

Figure 17 Angle of repose measured with GranuHeap. CR in red and DC in blue. Mean +/- standard deviation shown.

Table 14 Angle of repose, cohesion and height measured with GranuHeap. Mean and (standard deviation) shown.

HPMC	Angle of Repose (°)	Cohesion Index	Heap Height (mm)
K100M CR	67.4 (0.8)	1.8 (0.7)	37.1 (2.6)
K15M CR	63.2 (1.6)	1.3 (0.5)	34.0 (2.8)
K4M CR	60.1 (0.6)	0.8 (0.1)	30.1 (0.1)
K100M DC	59.8 (0.8)	1.3 (1.0)	29.4 (0.4)
K15M DC	60.5 (0.6)	1.2 (0.8)	30.0 (1.2)
K4M DC	60.0 (2.6)	0.7 (0.2)	30.2 (3.1)
P value (CR vs DC)*	**0.016**	0.392	**0.014**

*items in bold where P value < 0.05

3.2 Tapped Density

Based on the results from the GranuPack testing, DC grades demonstrated higher bulk density, tapped density, and predicted maximum density from tapping (ρ[∞]) compared to the CR grades as shown in **Table 15** (differences were statistically significant with $p < 0.05$). The materials did not differ significantly in the number of taps required to reach half of the tapped density or the Hausner ratio. In **Figure 18** it can be seen that the progression of tapped density was similar for all materials with the DC grades coming out with slightly higher tapped density when normalized by subtracting the initial density. According to the Hausner ratio they were all considered to have poor flow based on the bulk and tapped density (164, 165).

Table 15 Bulk and tapped density measurements from GranuPack. Mean and (standard deviation) shown.

HPMC Grade	Bulk Density (g/ml)	Tapped Density (g/ml)	n½ (taps)	Hausner ratio	ρ[∞] (g/ml)
K100M CR	0.288 (0.003)	0.411 (0.004)	83 (9)	1.426 (0.001)	0.463 (0.006)
K15M CR	0.312 (0.001)	0.431 (0.002)	82 (9)	1.384 (0.001)	0.482 (0.001)
K4M CR	0.324 (0.001)	0.450 (0.000)	89 (16)	1.387 (0.006)	0.510 (0.006)
K100M DC	0.344 (0.004)	0.477 (0.006)	75 (17)	1.387 (0.037)	0.533 (0.011)
K15M DC	0.324 (0.004)	0.467 (0.004)	117 (16)	1.442 (0.003)	0.533 (0.008)
K4M DC	0.335 (0.000)	0.469 (0.004)	113 (16)	1.401 (0.011)	0.533 (0.001)
P value (CR vs DC)*	**0.011**	**0.002**	0.156	0.494	**0.003**

*items in bold where P value < 0.05

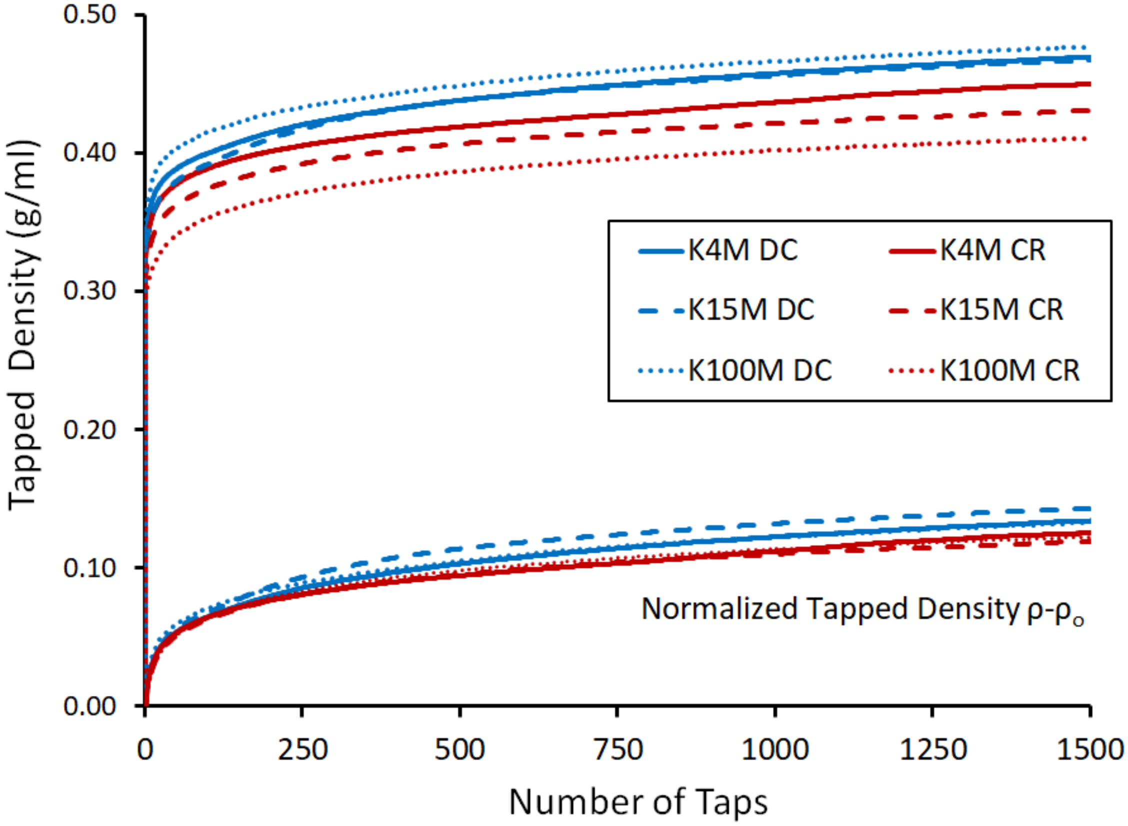

Figure 18 Tapped density profiles from the GranuPack. CR in red and DC in blue. K4M solid line, K15M dashed line, and K100M dotted line. Curves for tapped density normalized by subtracting the initial density are at the bottom.

3.3 Flow Angle and Cohesive Index

Since powder flow is a dynamic process it is beneficial to utilize dynamic tests to compare flow properties. To evaluate the flow of the different materials the flow angle and cohesive index were measured for each of the materials. The influence of the drum rotation speed on the powder flow behavior was determined by plotting the average flow angle and the average cohesive index against the drum speed.

The average flow angle shown in **Figure 19** increased for both materials from a drum speed of 2 rpm and reached a maximum at 8 rpm for DC and 10 rpm for CR and then decreased for both. Overall, the flow angle was slightly lower for the DC materials at drum rotation speeds > 10 rpm indicating less cohesive material, but the variability was high with overlapping standard deviations between the types.

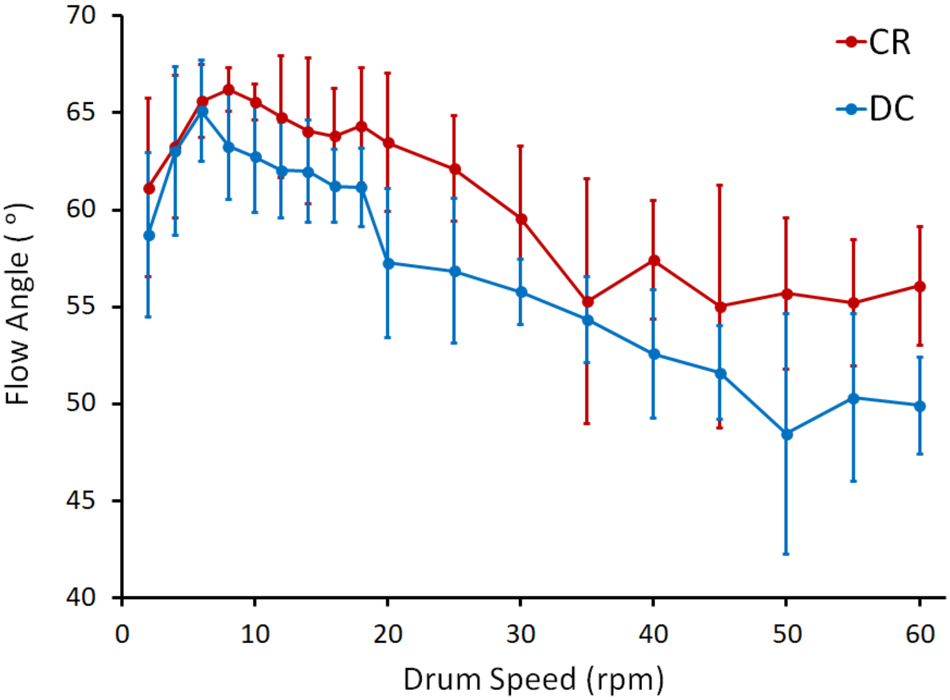

Figure 19 Average flow angle at each drum rotation speed measured on GranuDrum. CR in red and DC in blue. Mean ± standard deviation shown.

The average cohesive index, which is a measure of the variability of the flow, increased for both materials when the drum speed increased from 2 to 20 rpm although the DC type had a lower cohesive index across these speeds compared to the CR type as shown in **Figure 20**. As the rotation speed increased further, the cohesive index leveled out for the CR type but the DC materials showed a more regular and then better flow. This shear thinning behavior could be explained by a powder aeration at higher speeds. A similar decrease in cohesive index and shear thinning at increasing speeds was observed for lactose blended with 2% Mesoporous silica before testing (166).

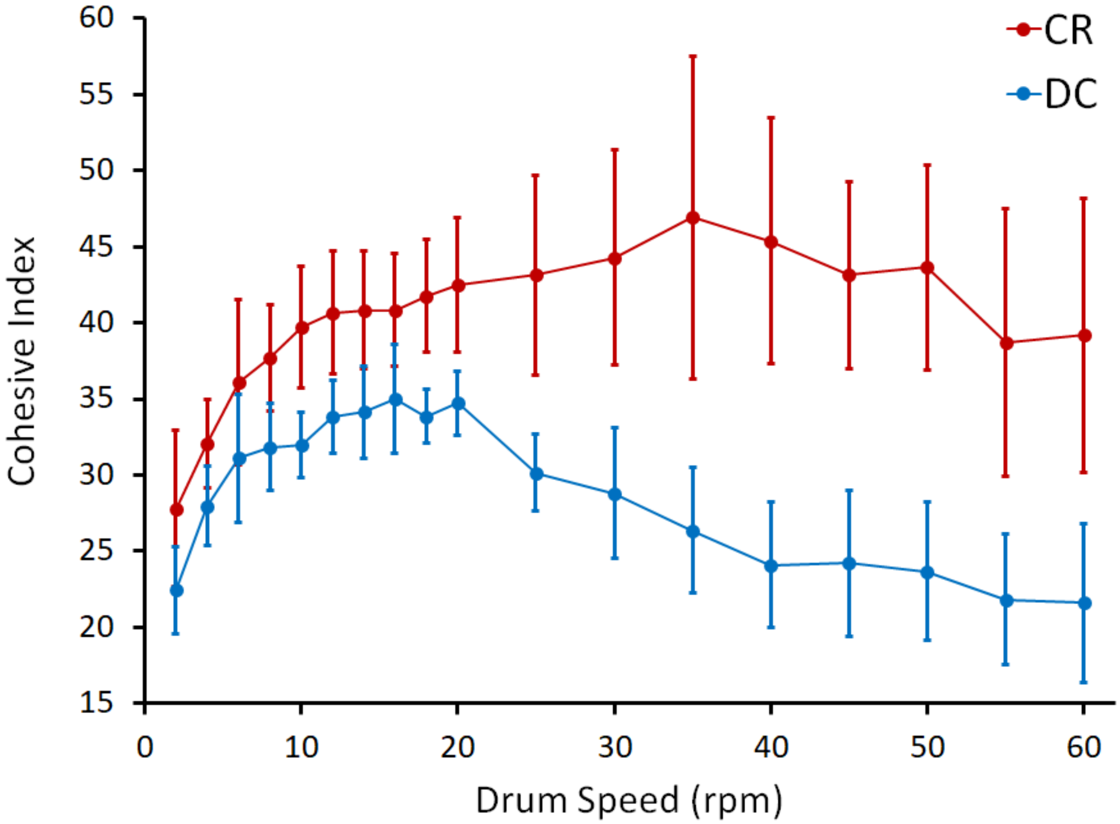

Figure 20 Average cohesive index at each drum rotation speed measured by GranuDrum. CR in red and DC in blue. Mean ± standard deviation shown.

3.4 Triboelectric charging of HPMC

Very few studies have assessed the importance of electrostatics during LIW feeding of powders and the potential impact it can have on the feeding process even when that possibility is acknowledged as a potential source of feeding error (167). Triboelectric charging can cause the powder to adhere to the LIW feeder barrel at the output and create electrostatic buildup powder. Over time, as the buildup increases it can become dislodged causing small or large spikes of powder to be added. When this occurs, it is detected by the control system since the mass of the equipment including the screw barrel is being measured to calculate the flow rate when in gravimetric control mode. However, when the LIW feeder was connected to the full CDC-50 hopper system which feeds into the blender, the buildup no longer occurred on the LIW feeder. Instead, the material started to build up on the discharge opening of the hopper. Since the hopper is not connected to the LIW feeder, any resulting material spikes would be invisible to the control system and could be problematic to product quality unless the blender was capable of blending out the unmeasured spike of material.

Of the materials studied, the CR types all had a small positive initial charge with significant charge accumulation after testing with 316 Stainless Steel. The accumulation of material on the barrel of the LIW feeder took on a different aspect depending on the feed rate as shown in **Figure 21**. Only K100M CR had a positive charge after testing with all other materials having a negative charge and the HPMC CR grades had charge accumulation such that K100M > K15M > K4M. This did not show the same trend as seen in another study where the magnitude of charge and surface adhesion inside a container decreased with increased polymer chain length such that K4M > K15M > K100M ranging from 12.3 to 3.9 nC/g depending on the HPMC grade and particle size (146). These opposing results may have come from the alternate test method of shaking powder in a stainless-steel container or from the HPMC itself which was from a different supplier and had different morphology.

Figure 21 Examples of electrostatic powder buildup of HPMC K4M CR at feed rates of **a)** 1 kg/h; **b)** 7.5 kg/h; **c)** 15 kg/h

The DC types all started with a small negative charge initially and only had a slight charge accumulation after testing. This correlated with a comparatively small amount of material accumulation on the LIW feeder barrel as shown in **Figure 22** and **Table 16**. The DC grades have been co-processed using a small amount of silicon dioxide which may provide both a mitigation against triboelectric charging as well as a flow aid. Similarly, mesoporous silica was studied in combination with lactose, starch and microcrystalline cellulose and was shown to decrease the charging of those materials (166). This is surprising since colloidal silicon dioxide on its own was shown to have the most negative chargeability of the materials studied and had the most electrostatic accumulation (168).

Table 16 Triboelectric charging measured by GranuCharge and material accumulation on feeder barrel after runs. Mean and (standard deviation).

HPMC Grade	Initial Charge q0 (nC/g)	Final Charge qf (nC/g)	Charge Accumulation Δq (nC/g)	Material accumulation on feeder barrel (g) 1 kg/h	 7.5 kg/h	 15 kg/h
K100M PH CR	1.32 (0.25)	6.96 (0.22)	5.64 (0.15)	0.81	5.13	6.52
K15M PH CR	0.88 (0.13)	-5.84 (0.49)	-6.73 (0.43)	0.36	*	*
K4M PH CR	0.63 (0.19)	-2.60 (1.01)	-3.23 (1.17)	4.05	*	13.53
K100M PH DC	-0.61 (0.05)	-1.08 (0.09)	-0.47 (0.10)	0.05	0.14	0.21
K15M PH DC	-0.76 (0.04)	-0.80 (0.02)	-0.04 (0.05)	0.28	0.10	0.19
K4M PH DC	-0.56 (0.14)	-1.44 (0.07)	-0.88 (0.12)	0.35	0.31	0.15
P value (CR vs DC)	**<0.001**	**<0.001 ****	**<0.001 ****	-	-	-

*Data not collected. Electrostatic differences were unknown at the time of feeding trials.
**The absolute value was used for statistical significance, due to positive final charge of K100M CR.

It is important to note that when there is buildup of material on the LIW feeder barrel there is the potential for some of this material to fall off in clumps causing spikes. This was observed during the feeder trials and resulted in measureable feeding spikes with the CR grade. An example of this is shown in **Figure 23 a and b** and has been seen with some other materials (115).

A majority of LIW feeder studies consist of feeding materials offline into collection containers, as was performed in this study. However, when LIW feeders are implemented in a continuous process there are multiple feeders inserted into a small hopper which feed a continuous blender. When the hopper was added to the LIW feeder there was no material accumulation on the feeder barrel but it did accumulate at the output of the hopper instead as shown in **Figure 23 c and d**. This is a critical finding because if the material were to build up anywhere else in the equipment other than the feeder barrel it would not be apparent to the control system during gravimetric feeding and would go unnoticed by the control system. It is possible that other materials in the formulation being fed into the same hopper could mitigate this electrostatic nature depending on their charge and as a result, the entire formulation and processing system should be considered.

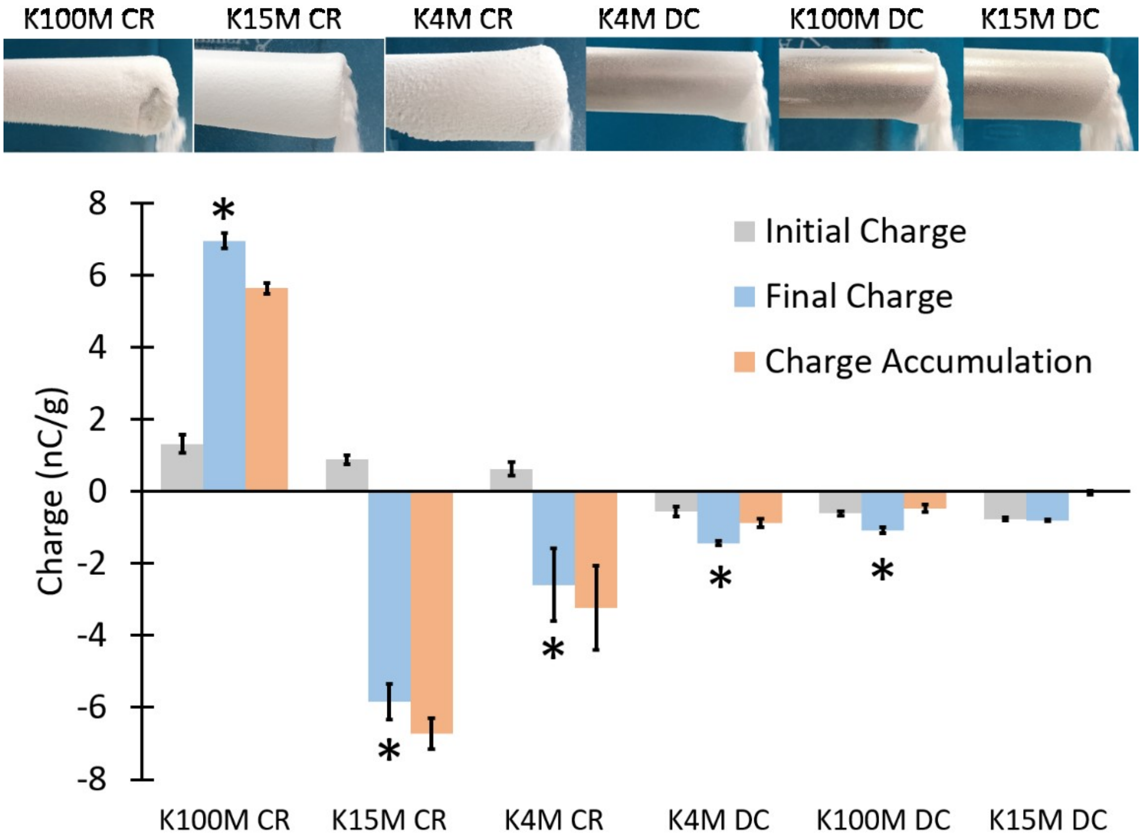

Figure 22 Initial charge in grey, final charge in blue and charge accumulation (difference of final and initial) in orange measured with GranuCharge. Plotted from highest to lowest with corresponding pictures of the material buildup of the powders on the LIW feeder barrels. Means ± SD are shown with * indicating P value < 0.05 for initial vs final charge.

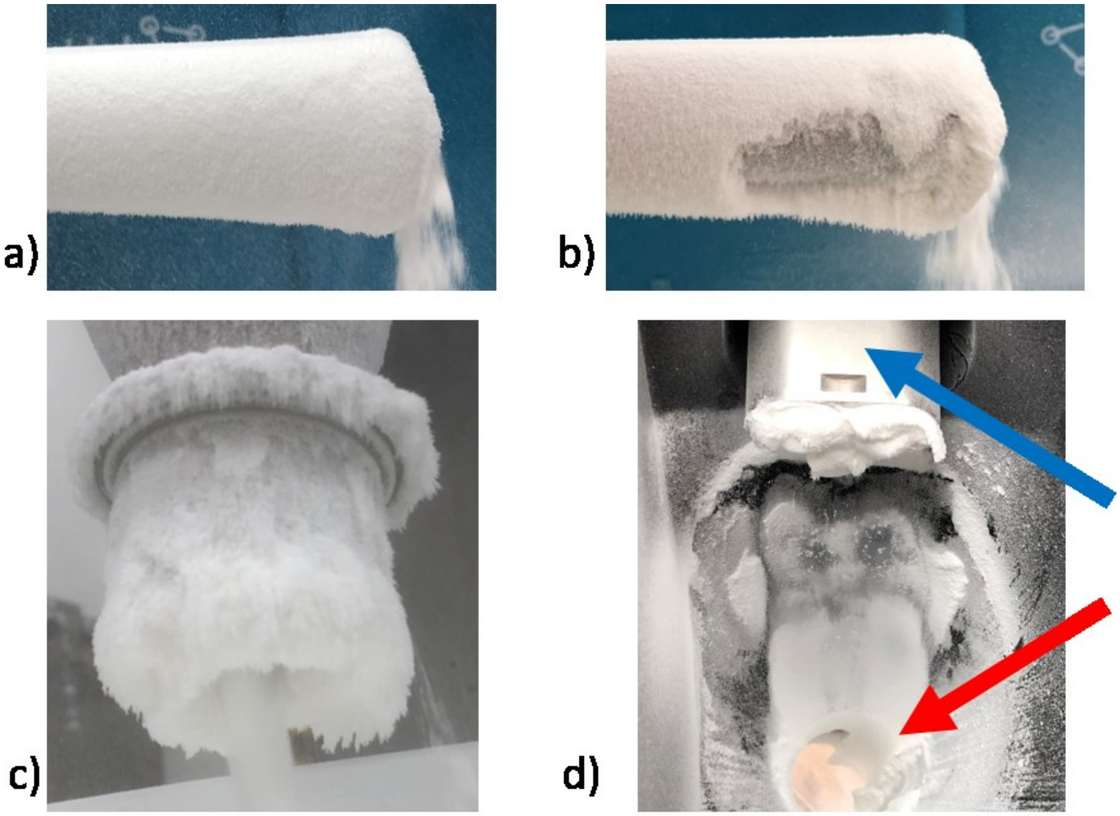

Figure 23 Representative images of electrostatic buildup of HPMC CR grades; **a)** material accumulation on feeder barrel; **b)** accumulated material falling off the barrel and causing a spike in the feed rate and mass flow RSD; **c)** material accumulation at output of the hopper; **d)** clean LIW feeder barrel (blue arrow) when placed into a hopper with material building up at hopper output instead (red arrow).

This study also explored the effect of materials of construction commonly used in pharmaceutical manufacturing using only K100M CR grade of HPMC. Charge accumulation was in the order of 316L Stainless Steel > Poly-Ethylene > Poly-Vinyl Chloride > Aluminum > High Density Poly-Ethylene, with approximately a factor of 2 between the high and low as shown in **Figure 24**. Previous studies have also demonstrated that the contact material can impact the charge accumulation of powders for Ibuprofen, theophylline, lactose monohydrate and microcrystalline cellulose using a V-Blender constructed of some common materials (169).

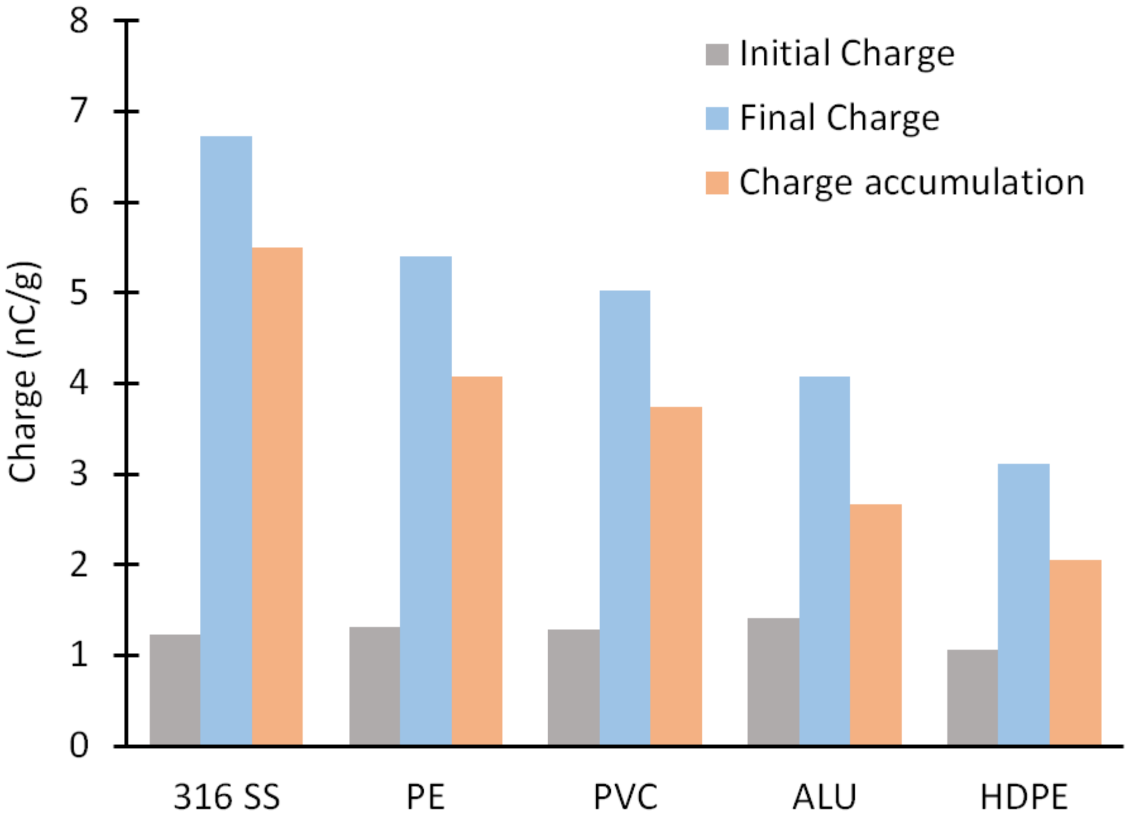

Figure 24 Initial charge in grey, final charge in blue and charge accumulation (difference of final and initial) in orange for HPMC K100M CR measured with GranuCharge for common materials of construction using tubes of 316L Stainless Steel (316 SS), Poly-Ethylene (PE), Poly-Vinyl Chloride (PVC), Aluminum (ALU), and High Density Poly-Ethylene (HDPE).

3.5 LIW Feeder Studies

The data was not evaluated when the feeder was running in volumetric mode (during the refill cycle) as the weights are inaccurate when the refill hopper engages for the refill. A catch scale to weigh the material being fed from the LIW feeder is one way to accurately capture the feed rate during volumetric mode but was not available for these experiments.

The first 20 seconds for refill 1 (the start of feeding) was removed for all of the trials for 7.5 and 15 kg/h and the first 45 seconds for refill 1 of 1 kg/h trials to allow for stabilization of the feed rates and feed factors during startup of the equipment until the Instantaneous Mass Flow RSD dropped below 1%. This initial startup was not representative of the entire run and continuous processes reject initial materials during startup to allow for system stabilization.

Other data that was excluded from the comparative analysis was K4M CR at 15 kg/h for time >386 seconds which had additional refills to evaluate a long run. Also, K4M CR at 1 kg/h for time >3,950 seconds since it had a significantly longer run than the equivalent DC type with increasing mass flow variability after that time.

There were three events during the experiments which were excluded for cause. The first event was for the K100M DC at 7.5 kg/h when it ran out of powder. When the situation was realized the process was stopped, more powder was added to the refill hopper and the process was run longer to complete additional refills. During this time of having an empty hopper and being topped up (484.6 - 706.4 sec) the data was excluded from the calculations. The second event occurred for K100M DC at 15 kg/h where the balance was disturbed when the hopper was accidently touched when checking powder levels from 122.2 - 123.6 seconds. The third event was for K15M CR at 7.5 kg/h when the door to the processing room was opened which disturbed the feeder balance between 288.0-290.4 seconds.

The screw speed required to achieve the target mass flow rate can be dependent on the particle properties such as the bulk density, particle size, and shape. While there were slight differences in the bulk density and tapped density between the CR and DC types, it did not seem to affect the filling of the screws as the correlation between screw speed and mass flow were similar as shown in **Figure 25** with a linear increase across the ranges studied.

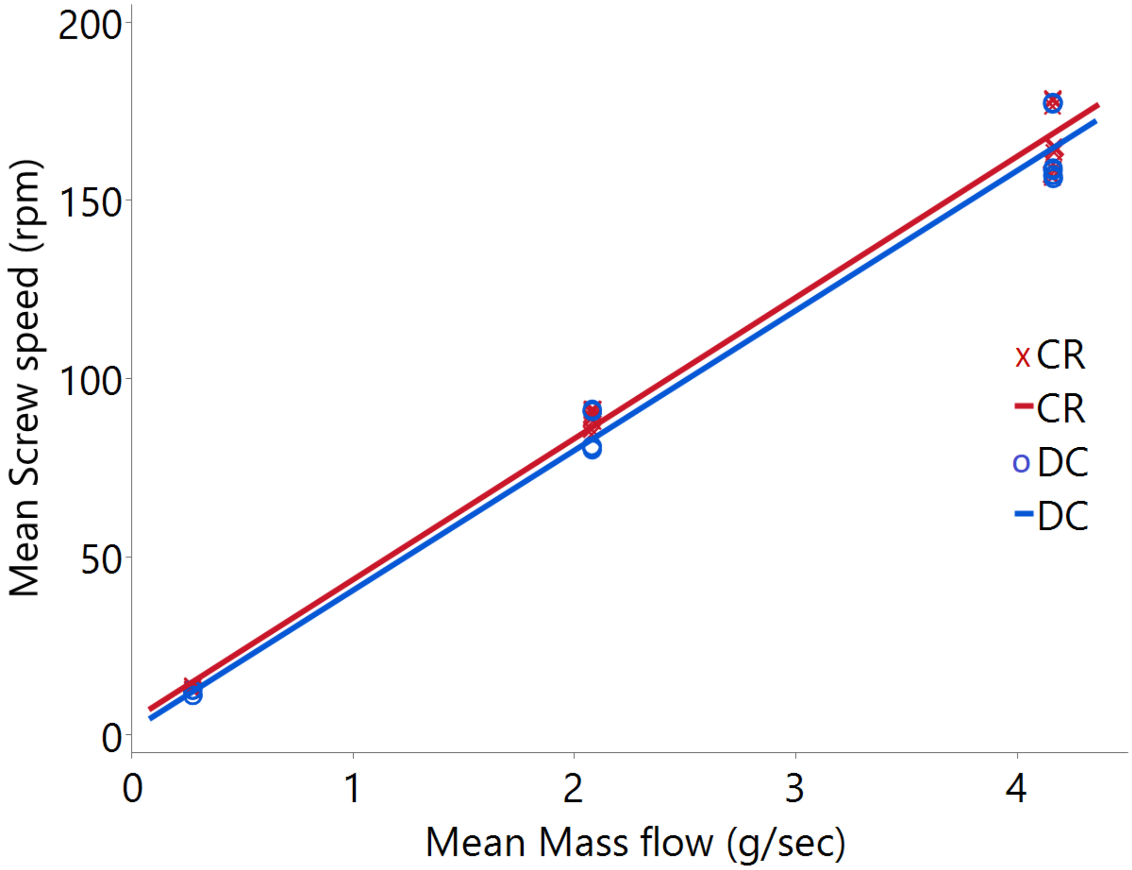

Figure 25 Correlation between the mean screw speed and mean mass flow for each grade and rate. CR in red X and DC in blue circle.

The LIW feeders are designed to deliver the target feed rate by using a feedback loop to automatically adjust the screw speed in response to the measured mass flow when running in gravimetric mode. The mean mass flow rates were almost identical and on target for all of the materials indicating that the LIW feeders are capable of delivering the target mass flows. The standard deviations of the mass flow rates were all low with the standard deviation and range being lower for the DC types as shown in **Table 17** indicating better feeding performance.

Table 17 Feeder mass flow rate, range of mass flow, and screw speed. Mean and (standard deviation) shown for mass flow and screw speed.

Rate (kg/h)	Grade	Type	Mass flow (g/sec) (Standard deviation)	Range of Mass flow (g/sec)	Screw speed (rpm) (st.dev.)
1	K100M	CR	0.278 (0.003)	0.024	13.4 (0.2)
1	K15M	CR	0.278 (0.002)	0.022	12.4 (0.2)
1	K4M	CR	0.277 (0.005)	0.050	12.6 (0.2)
1	K100M	DC	0.278 (0.002)	0.017	11.0 (0.1)
1	K15M	DC	0.278 (0.002)	0.018	12.4 (0.2)
1	K4M	DC	0.278 (0.002)	0.019	11.0 (0.1)
7.5	K100M	CR	2.082 (0.021)	0.288	91.1 (1.2)
7.5	K15M	CR	2.084 (0.014)	0.179	89.7 (1.5)
7.5	K4M	CR	2.079 (0.031)	0.729	87.3 (2.4)
7.5	K100M	DC	2.082 (0.011)	0.092	80.5 (0.8)
7.5	K15M	DC	2.082 (0.012)	0.099	90.9 (1.0)
7.5	K4M	DC	2.082 (0.017)	0.107	80.8 (0.9)
15	K100M	CR	4.163 (0.039)	0.541	178.0 (2.0)
15	K15M	CR	4.169 (0.047)	1.332	164.5 (1.3)
15	K4M	CR	4.162 (0.064)	1.703	158.3 (3.0)
15	K100M	DC	4.164 (0.017)	0.123	156.6 (1.5)
15	K15M	DC	4.163 (0.023)	0.177	177.2 (1.9)
15	K4M	DC	4.163 (0.017)	0.143	158.6 (1.9)

In order to compare across feed rates, the percent difference of the measured mass flow from the target rate was calculated at each time point and demonstrated that most of the mass flow data points were within 5% of the target rates as shown in **Figure 26**. The materials were close to target with small standard deviations indicating that overall the equipment performed well for both types of material. This was expected since there is a feedback loop when running in gravimetric mode that adjusts to keep the mass flow close to target. There were occasions where the mass flows were off target at different times in the feeding trials. As shown in **Figure 26**, the CR types had more excursions which were outside of 5% of the target mass flow rate compared to the DC types which were all within the 5% limit. Overall, the DC grade mean mass flow percent offset was closer to target (DC mean = -0.0006% +/- 0.0068) compared to the CR type (CR mean = -0.0013% +/- 0.0124) and the difference was statistically significant with a P value < 0.001. In a multiple comparisons test for equal variances, the DC materials had lower standard deviations compared to their CR counterparts for each of the grades and the difference was also statistically significant as shown in **Figure 27**.

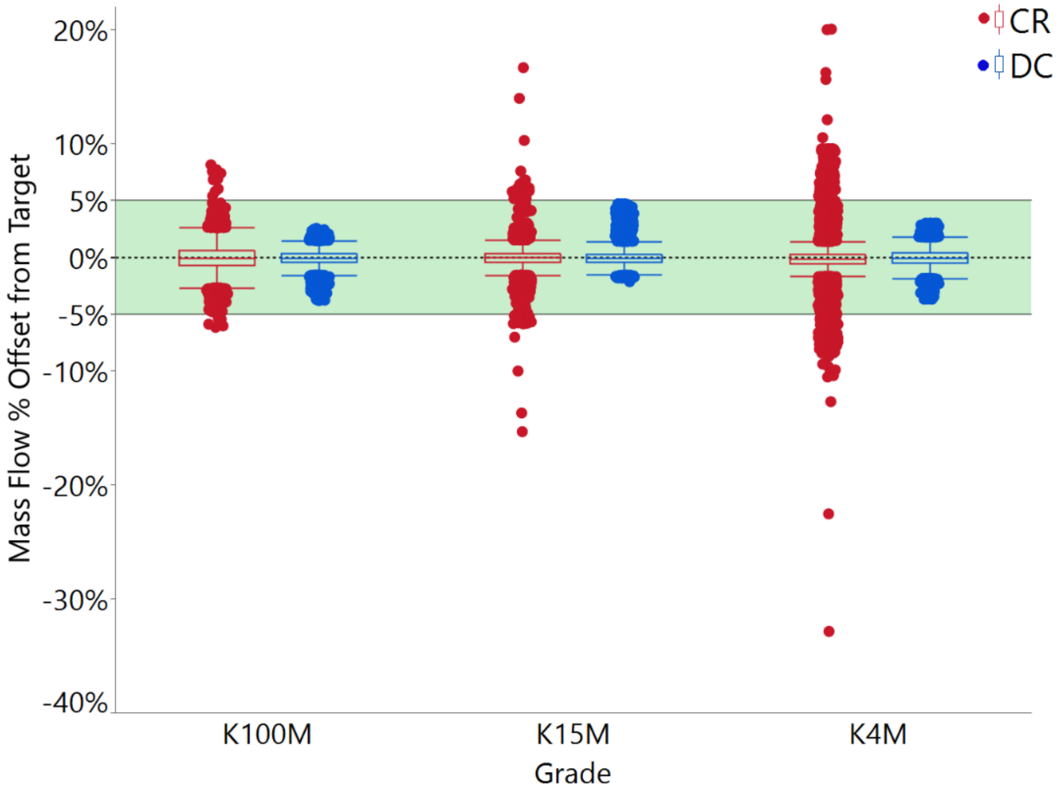

Figure 26 Mass flow percent offset from target mass flow rate. CR in red and DC in blue. Green band indicates mass flow rate +/- 5% from target rate.

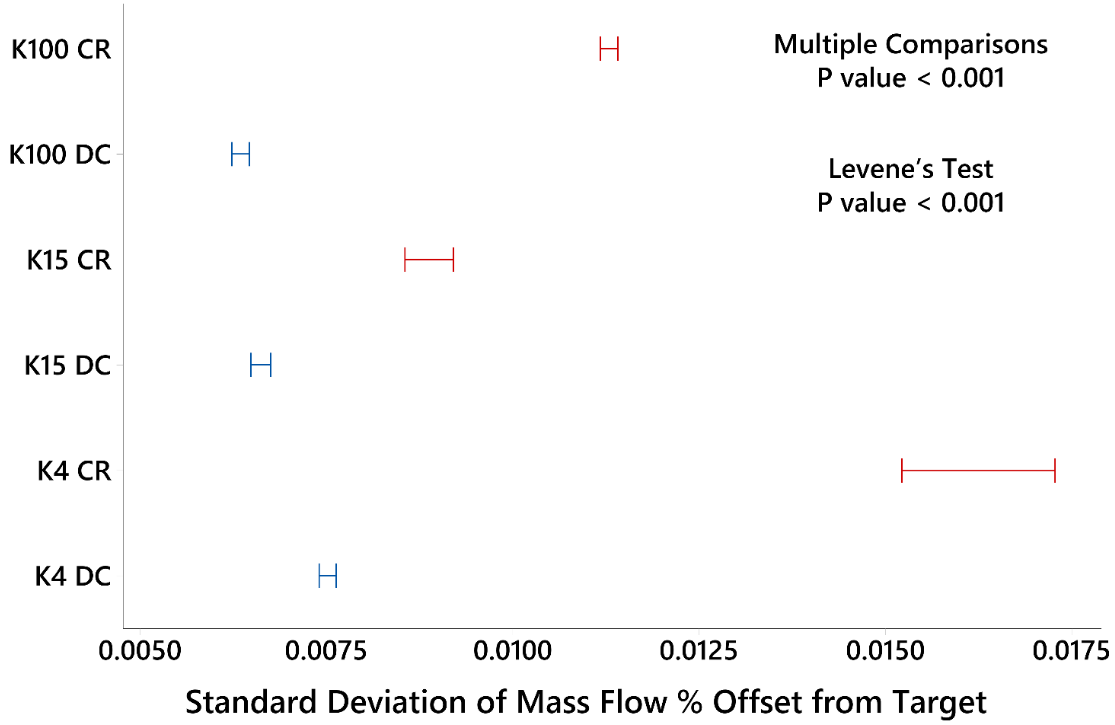

Figure 27 Test for Equal Variances CR vs DC: Mass Flow Offset vs Grade Type. Multiple comparison intervals for the standard deviation, α = 0.05. If intervals do not overlap, the corresponding standard deviations are significantly different. CR in red and DC in blue.

Another measure of the acceptability of the material for use in LIW feeders is the Instantaneous Mass Flow RSD. This is the moving relative standard deviation of the mass flow signal using a variable window size. The window size is equal to 50% of the mass flow filter length which changes based on the flow rate, decreasing at higher speed. The Instantaneous Mass Flow RSD was similar across the feed rates as shown in **Figure 28**. A previous study with different feeding equipment showed that the RSD was higher for the lower feed rates (170, 171) which was not observed in this work. The mean of the Instantaneous Mass Flow RSD for all the grades combined was similar, with the DC grades being slightly lower overall as shown in **Figure 29**. Across all grades and rates the mean Instantaneous Mass Flow RSD was lower for the DC materials (DC 0.334 ± 0.246 vs. CR 0.407 ± 0.246) and the difference was statistically significant with a P value < 0.001 indicating the DC materials performed better for LIW feeding.

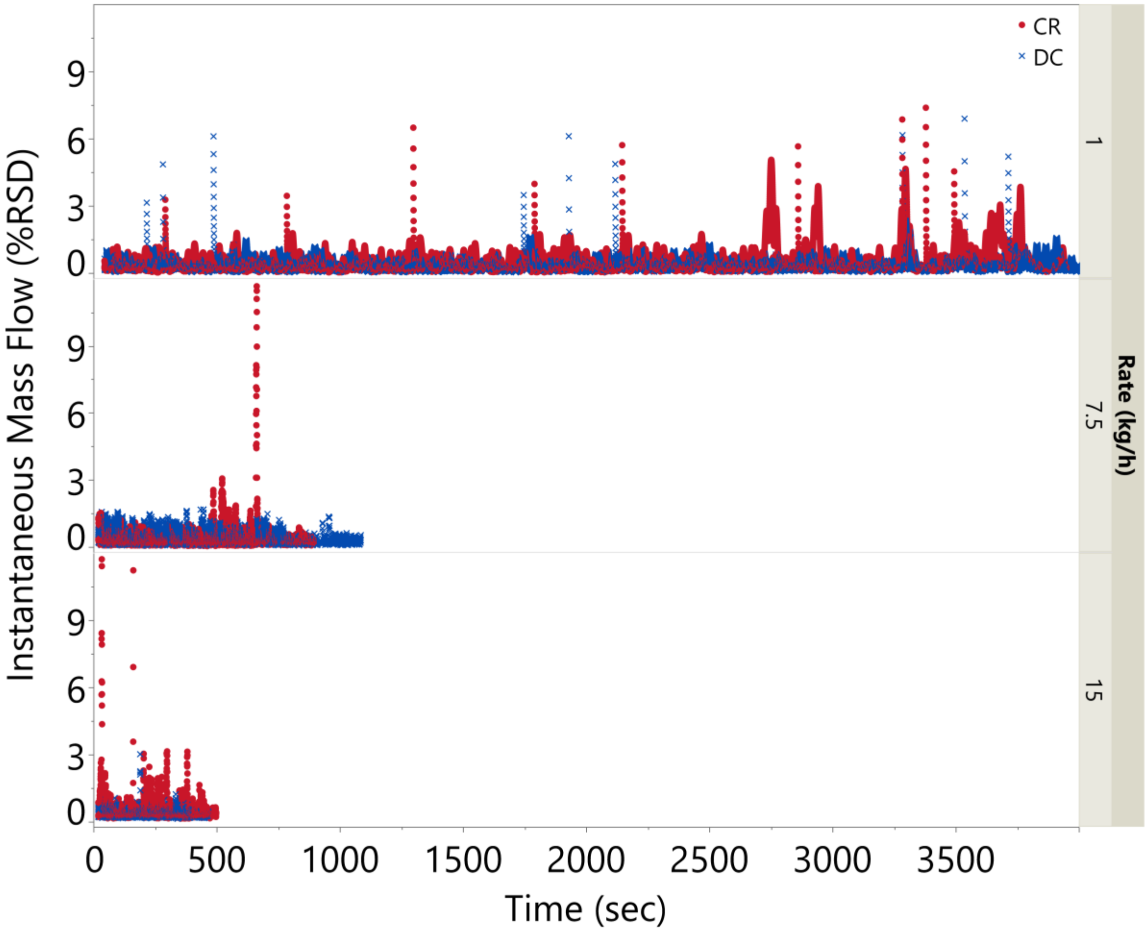

Figure 28 Instantaneous Mass Flow RSD over time (seconds). CR in red and DC in blue.

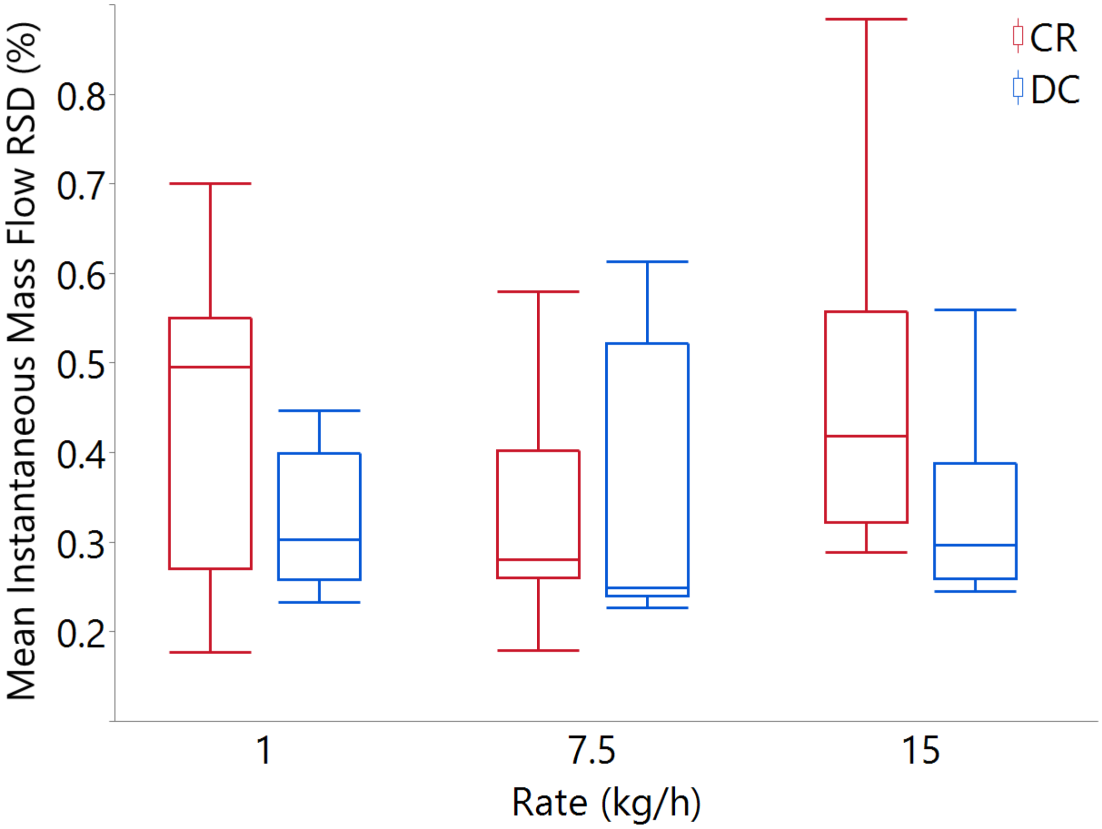

Figure 29 Mean Instantaneous Mass Flow RSD by feed rate for all materials per refill. CR in red and DC in blue.

Mass flow excursions can be caused by several factors beyond the normal variability of the process. These excursions can come from hopper refills, either just before going into a refill or coming out of a refill, external influences on the sensitive scale, and/or changes in material properties or powder flow (172). Mass flow excursions can also result from material adhering to screw outlet via electrostatics as discussed in **Section 3.4**. As the material adheres to the screw outlet it can build up on the stainless-steel feeder barrel and occasionally excess material can fall off in varying amounts. This causes a measurable spike in the mass flow which induces a response in the feedback control slowing down the screw speed which drops the mass flow below target before eventually adjusting back to target. An example of this spike and response is shown in **Figure 28** at approximately 675 seconds for K4M CR at 7.5 kg/h where it was observed that a large amount of buildup fell off as shown in the pictures of Figure 8a and 8b. A zoomed in view of the LIW feeder control system response to one of these spikes is shown in **Figure 30**.

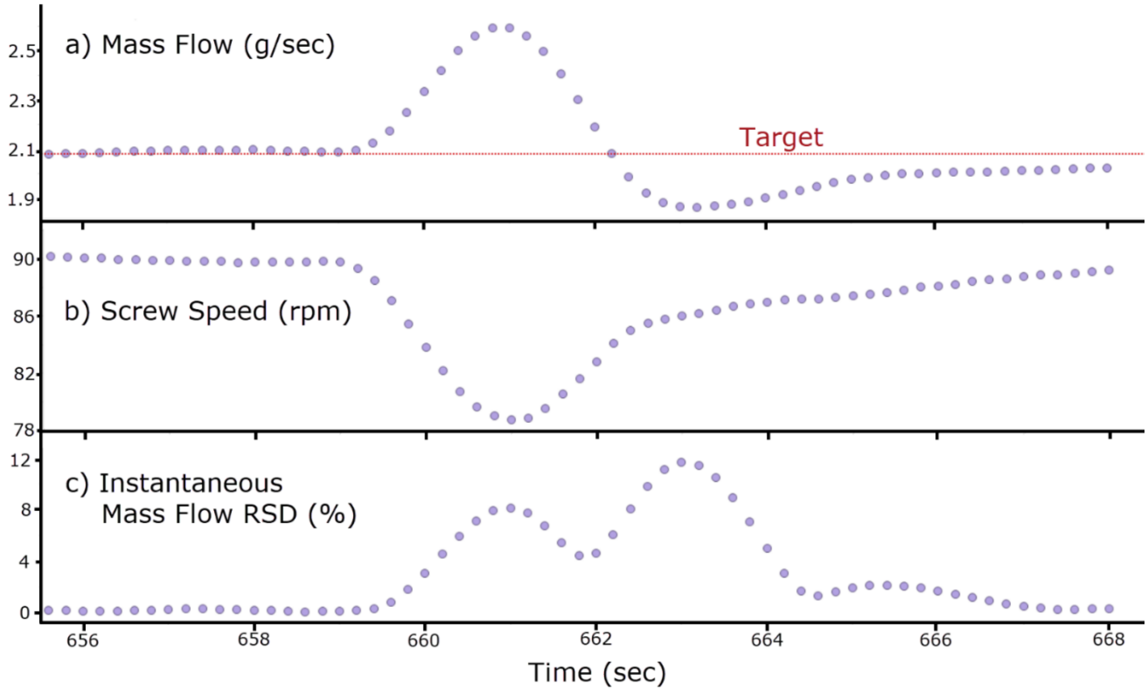

Figure 30 LIW feeder control system response to electrostatic buildup falling off the feeder barrel. a) Mass flow increase from the material falling off, target mass flow red dotted line. b) Screw speed responded to mass flow increase. c) Instantaneous Mass Flow RSD peaks from the extra material and then from the decreased rate after the screw speed responded to the extra material.

Bridging of the powder in the feeder hopper preventing it from getting into the feeder screws is unlikely to occur in the GEA compact feeder due to the inclusion of a rotating impeller to agitate the powder. However, if the material bridges or ratholes in the feed chute leading to the refill container it can result in a failed refill attempt. There were some instances of failed refills during these trials for the CR types. Ratholes in the feed chute were observed for both K15M CR and K100M CR which prevented the refill from being completed. A similar phenomenon was observed in other feeder studies with different materials and equipment (173, 174).

The number of refill attempts were evaluated to identify any challenges from the refill hopper. Even if a material has acceptable mass flow, the process overall is unacceptable if the material is not being refilled. In some instances when the refill bowl would turn to dump additional material into the hopper, the powder would not empty from the bowl or the material had bridged or formed a rathole in the feed chute preventing it from filling the refill bowl. In these cases, the lack of additional powder was recognized by the system since no mass was added and it would trigger another refill attempt. After the first failed refill attempt the equipment was manually tapped to help the powder fill and empty from the refill bowl. After the second failed attempt the powder above the refill bowl was stirred manually and the outside was tapped to ensure powder would be transferred to the hopper. There were two instances where the standard CR grades required two refill attempts and three instances where it took three refill attempts. The DC type did not have any failed refill attempts.

In addition to the number of refill attempts, the amount of time for the refill to occur was evaluated. When the refill is occurring the LIW feeder is running in volumetric mode instead of gravimetric and the feeder mass is not being measured so there is more potential for inaccurate mass flow. After a refill occurs, the feeder stabilizes before switching back to gravimetric mode. The lowest feed rate of 1 kg/h resulted in the longest time to refill for all materials while the 7.5 and 15 kg/h took similar times as shown in **Figure 31**.

The CR type had multiple occasions where refills took longer at each of the rates resulting in longer time running in volumetric mode which increases the risk of inaccurate mass flow. For this reason, the improved flow of the DC grades is beneficial to prevent refill issues and reduce the amount of time that the feeder is running in volumetric mode during refills where the actual gravimetric feed rate is not measured. The importance of refills should not be overlooked when conducting LIW feeder studies.

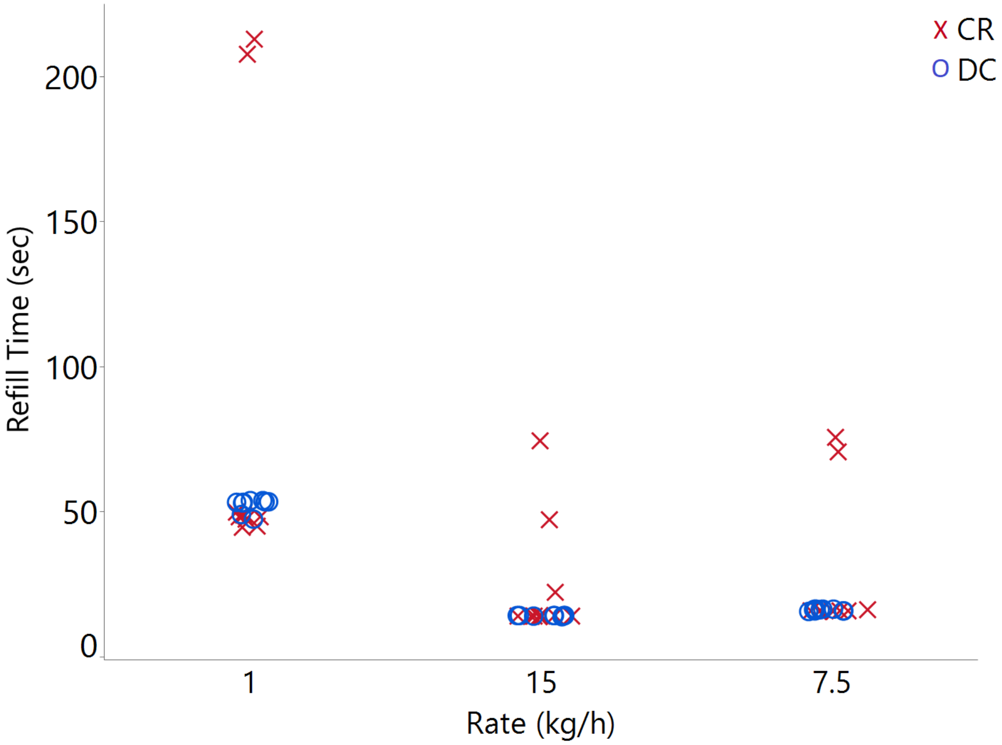

Figure 31 Time for a refill of the hopper to occur. CR red X and DC blue circle.

The K4M CR material was used to perform a longer run covering eleven refills. As can be seen in **Figure 32**, the number and degree of mass flow excursions increased over time except for refills #5 and #8. While this was observed for the long run, there was no increase in excursions over time observed during the first three refills when comparing all the materials.

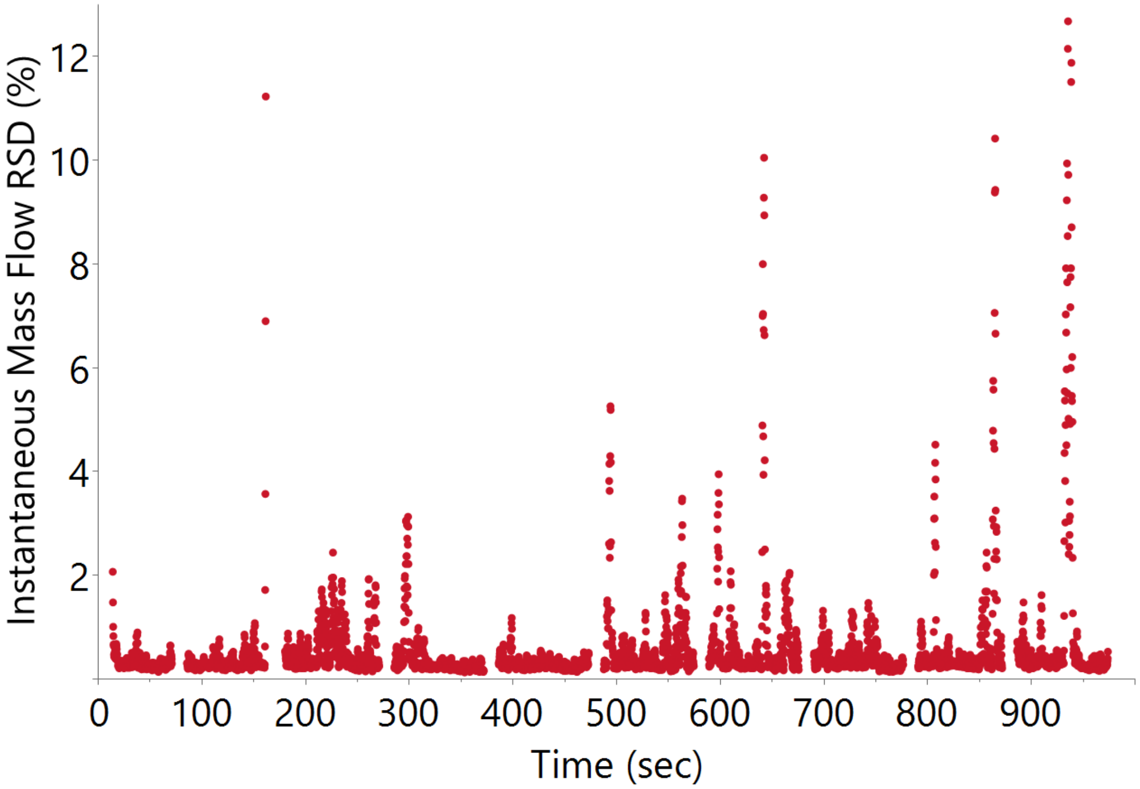

Figure 32 Instantaneous Mass Flow RSD for long run of K4M CR over time. Breaks in data indicate a refill event.

Some degree of sinusoidal variation to both the Mass Flow and the Instantaneous Mass Flow RSD was observed over a 3-5 second range for all feed rates fluctuating about 2% from the mean Mass Flow as shown in **Figure 33**. This was also observed for silicified microcrystalline cellulose over a 2 second period when feeding at 12 kg/h and measured at 0.1 second intervals using a different loss-in-weight feeder (115). The oscillations they observed were an order of magnitude larger and significantly more periodic. The authors hypothesized that it was due to free-flowing powder emptying out of each flight of the screws because when a screw with a smaller free volume was used the pulsations were reduced in magnitude.

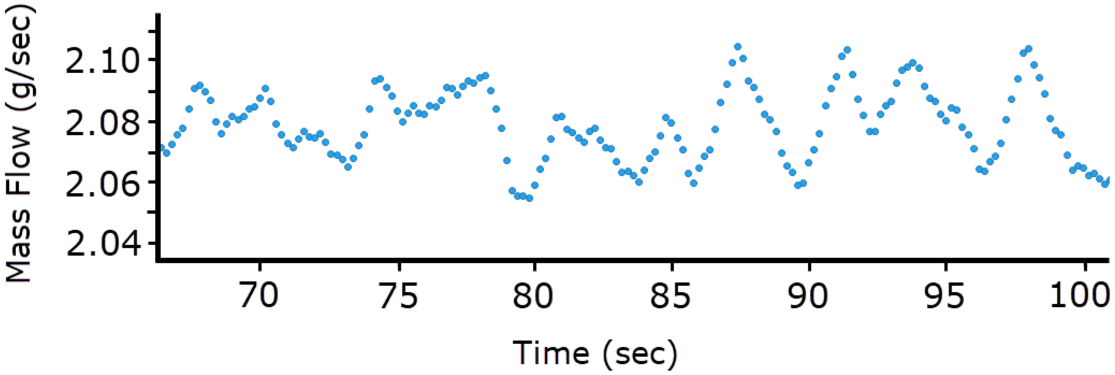

Figure 33 Example of periodic fluctuations in mass flow over a short time frame for K100M CR at 7.5 kg/h.

4 CONCLUSIONS

The bulk density and tapped density were higher for the DC HPMC grades. It was expected that this difference in density would affect the packing of the material in the screw and result in lower screw speeds required to achieve the target mass flow, but this was not the case. Both CR and DC had similar screw speeds with a linear increase in the screw speed / mass flow relationship over the range studied.

It was demonstrated previously via different powder flow testing methodologies that the directly compressible (DC) HPMC had better flow properties compared to the standard (CR) HPMC even though they had similar particle size and morphology. This work also demonstrated improved flow overall for the DC HPMC with additional testing methodologies. The angle of repose, heap height, flow angle and cohesive index all indicated that the DC grades had better flow while the cohesion index from the angle of repose and the Hausner ratio from bulk and tapped density did not show differences in the materials.

Even though the DC material showed better flow, it was not known if that would translate into improved LIW feeding since the equipment utilizes a feedback loop to keep the feed rate at target. While the mass flow was kept on target for all materials the DC HPMC had lower mass flow standard deviation, a smaller range for the mass flow, less excursions and lower standard deviation of the mass flow offset from target. These results were observed across all three HPMC grades and all three feed rates leading to the conclusion that the DC HPMC performed better for LIW feeding across the ranges studied. Depending on the system and sensitivity, it is possible that the variability in the CR HPMC would be blended out during downstream processing in the continuous manufacturing train. However, the impact is process and formulation dependent, and would require an understanding of residence time distributions for the entire system to determine how frequently and to what degree these mass flow deviations are acceptable.

Another important aspect to LIW feeding is the refill to the hopper. Even if the system can handle the larger variability and excursions with the CR HPMC the materials need to be refilled frequently as the feeder hopper runs out of material. If the material bridges or creates a rathole it can be very problematic for a process which is meant to run continuously. The DC HPMC all refilled the LIW feeder hopper on the first attempt, but the CR HPMC had instances where the hopper refill failed. On multiple occasions for CR HPMC, the equipment needed to be stopped after a failed refill to manually intervene. This performance would be extremely problematic for a continuous manufacturing system which is designed to be run constantly without interruption and where accessing the powders would be very challenging because of the sealed and contained nature of the equipment. It was also detrimental to the mass flow because the equipment switches to volumetric dosing during a refill. At this stage the actual mass flow is not being measured since more powder is being added to the balance. During this time, the system is prone to feeding inaccuracies which are not being measured. In some cases, when there was a failed refill, it resulted in volumetric dosing which was four times longer.

The importance of fully characterizing the powders intended to be used in a LIW feeder was demonstrated by the triboelectric charging of the materials. DC HPMC had significantly lower triboelectric charging compared to the CR type. The initial charge, final charge and charge accumulation were closer to zero for the DC HPMC. The criticality of this was observed in the feeding trials where the CR types had high amounts of electrostatic buildup of material on the feeder barrel and resulted in increased number of mass flow excursions during the run.

Even more critical was the observation that the location of the electrostatic buildup of material changed with the configuration of the equipment. This effectively ‘blinds’ the control system so that buildup and subsequent spikes from material falling off is no longer observed when the material is building up in a location other than the feeder barrel which is attached to the mass sensors. Results from feeding studies using an offline LIW feeder going into a container may not be transferrable to a full, contained continuous manufacturing system when there are electrostatic effects in play as well as other materials which could either mitigate or increase the effect. Most continuous manufacturing systems are sealed and contained which could help to prevent electrostatic material buildup but would also make it extremely difficult to observe if it did occur inside the system.

The direct compression (DC) grades of HPMC were developed for better flowability and improved tablet compactability but these improvements also apply to LIW feeding providing for tighter control over the mass flow, reduced triboelectric charging, fewer feed rate excursions, and more consistent refills. Avoiding the complications of acquiring a rathole in the powder inside the system is a significant advantage by itself, even if the higher feed variability and excursions with CR HPMC were acceptable for the system. All of these improvements observed with DC HPMC would be beneficial when running any continuous process (wet granulation, roller compaction, or direct compression) or other processes where LIW feeding is utilized such as melt extrusion or twin-screw granulation.

CHAPTER 3 MODELING OF A LOSS IN WEIGHT FEEDER WITH ELONGATED PARTICLES TO SUPPORT CONTINUOUS MANUFACTURING

1 BACKGROUND

The goal of this work was to incorporate the hydroxypropyl methylcellulose (HPMC) Direct Compression (DC) material previously characterized in **Chapter 1** and **Chapter 2**, which was shown have improved flow and compactability over the standard HPMC grades, into a computer model of the loss-in-weight (LIW) feeder using Discrete Element Method (DEM) as the first component of a continuous manufacturing system.

A full development or commercial rig such as the CDC-50 (GEA Group, Düsseldorf, Germany) consists of multiple loss-in-weight feeders adding different excipients and the active ingredient(s) into a continuous blender for blending the materials to a uniform distribution. The material would then be fed into a second continuous blender to add lubricant and possibly other extragranular materials before being fed into a rotary tablet press. After the tablets are produced they can be conditioned to allow for tablet relaxation before being transferred to a continuous coater, realizing the goal of producing a final dosage from in a continuous manner from the individual ingredients.

The advantages of improved flow, reduced triboelectric charging, and improved tabletability for the novel DC type HPMC make it ideal for use in the continuous process. However, modeling approaches for nonspherical particles like HPMC are particularly challenging. For this reason a DEM approach using overlapping multi-spheres to represent the HPMC was implemented. Calibration of these multi-spheres was performed by simulating multiple characterization tests using DEM in order to determine the appropriate model particle parameters. Once the parameters were established they were validated against another characterization test and then utilized in a DEM model of the LIW feeder and the results compared to experimental.

2 MATERIALS AND METHODS

2.1 Materials

Benecel^{TM} Directly Compressible Hypromellose K100M DC grade from Ashland Inc. was used as the model material for this study and was previously characterized in detail in **Chapters 1 and 2**. The DC type of HPMC has similar particle size and morphology as the standard K100M CR HPMC but has been co-processed with a small amount of silicon dioxide to improve flow and compactability.

2.2 Particle size and geometry determination for use in DEM simulations

Before running the DEM simulations it was necessary to determine the appropriate DEM particles to represent the elongated fiber-like HPMC. DEM simulations are typically run using spherical representations for the particles due to the reduced computational requirements for spheres. However, due to the elongated nature of the HPMC material as shown in the Scanning Electron Micrograph (SEM) in **Figure 35**, it was necessary to create DEM particles that were more representative of HPMC's geometrical characteristics.

Other studies have used overlapping spheres, glued spheres, complex polyhedrals, ellipses or cylinders to mimic nonspherical particles (39, 175-180). Each of these approaches have trade-offs between accurate representations of the material and the computational workload. Some work has even been done with entangled particles (181) but the high computational requirements limit the ability to utilize these particles in more complex models with a large number of particles. The overlapping multi-sphere method was used for this study to get representative complex shapes for particles. This approach has been shown to work in previous studies for different shapes (176, 182, 183) and the additional novel step of including variation in aspect ratios was implemented to better represent the HPMC.

Particle shape and size analysis was performed previously using image analysis (Sympatec QicPic GRADIS) to measure approximately 1-2 million particles. The particle size was determined using the volume EQPC (EQuivalent Projection area of a Circle) method which is based on the diameter of a circle with the same area as the area of the actual particle from image analysis. The HPMC K100M DC had EQPC particle size distribution as follows: D10 = 57 µm; D50 = 107 µm; D90 = 184 µm. This can be described as 10% of the particles had an EQPC size less than 57 µm while 50% of the particles had a EQPC particle size less than 107 µm.

The DEM model utilized material with larger particles compared to the actual HPMC material. Particle sizes in the simulation with 1.2 mm or 2 mm EQPC were 12 to 20 times larger than D50 of HPMC (also via EQPC measurements). The reason for using a larger particle size in the DEM model is that it reduced the total number of particles required for the simulation by 1,728 times less particles for 1.2 mm and 8,000 times less particles for 2.0 mm particles, resulting in significantly reduced computation time to run the simulations.

Multiple versions particles were considered for use in the simulation and are shown in **Figure 34**. The simplest was a capsule shaped particle shown in **Figure 34a**, created from a capped cylinder with dimensions of length and width to replicate the elongated nature of HPMC. Although they had an elongated form, they did not fit the data well due to the smooth and straight surface. The most similar to the actual HPMC material was “HPMC replica” particles shown in **Figure 34b** which were based on a set of six different shapes made of different sized spheres and arrangements to match the particles observed in the SEM as shown in **Figure 35**. While these particles were the most similar they were computationally intense from a DEM perspective and more simplified particles were required. The final set, which were utilized in this study, were Bow shaped particles shown in **Figure 34c**. These were simplified versions of the HPMC replica particles with different aspect ratios to imitate the actual HPMC particle variability during collisions.

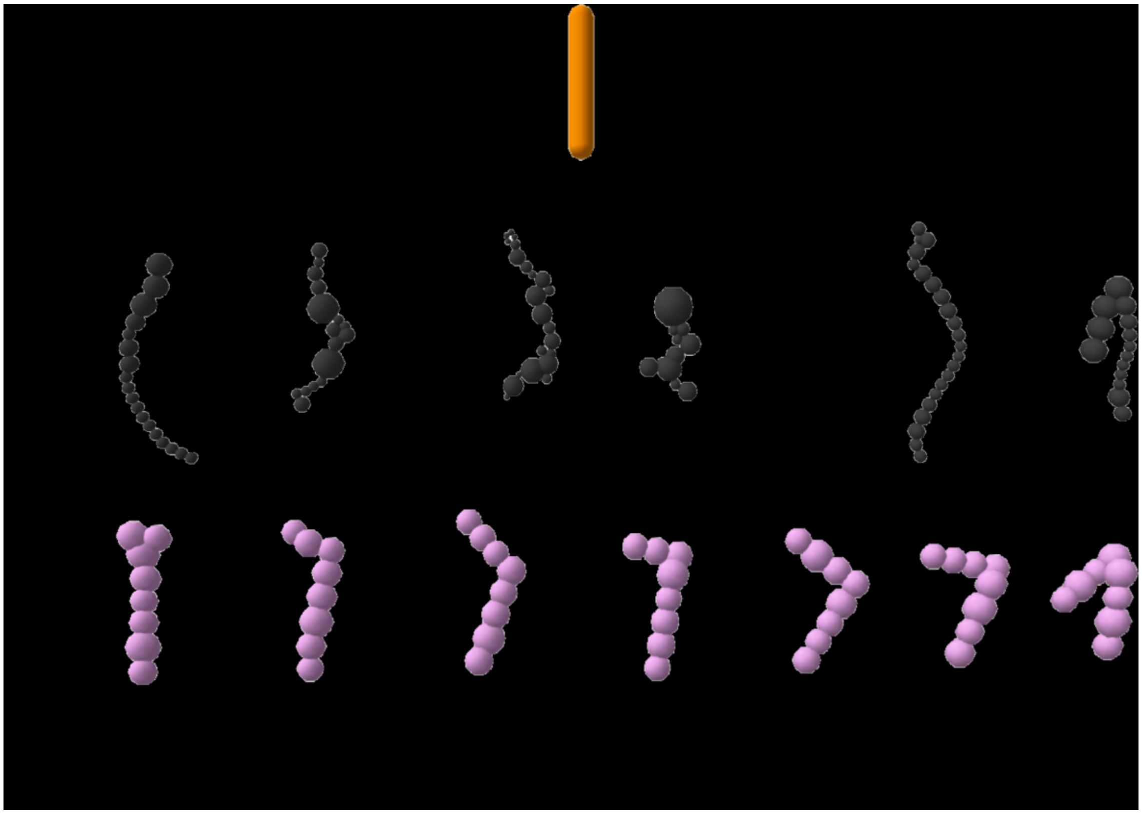

Figure 34 Shapes evaluated to represent HPMC proposed for the simulation. All particles have the same EQPC. **a)** Capsule shaped; **b)** HPMC replica particles with six different shapes depicted; **c)** Bow particles that were used in the DEM model with seven different shapes and varying aspect ratios numbers shown for reference in **Table 18**.

Figure 35 Representative SEM image of K100M DC HPMC at a magnification of 100x and representation of 'HPMC replica' particles shown in orange.

The aspect ratio (AR) provides an indication of the elongation of the particles, and is a measure of the length and width of the particle. It is calculated by AR = F_{min}/F_{max} where AR is the Aspect Ratio, F_{min} is the minimum Feret diameter which is the shortest distance between any two parallel tangents on the particle and the F_{max} is the longest as shown in **Figure 36**. The HPMC K100 DC had aspect ratios of D10 = 0.37; D50 = 0.57; D90 = 0.80. Similar to the distribution of sizes for the particles there is a distribution of aspect ratios where 50% of the particles had an aspect ratio less than 0.57.

The method of introducing particle shape variability from different aspect ratio particles was preferred over implementing a distribution of shapes and sizes due the computational requirements. Calibration of the Bow particles using the simulated characterization tests was necessary to establish the material properties for the DEM LIW feeder model.

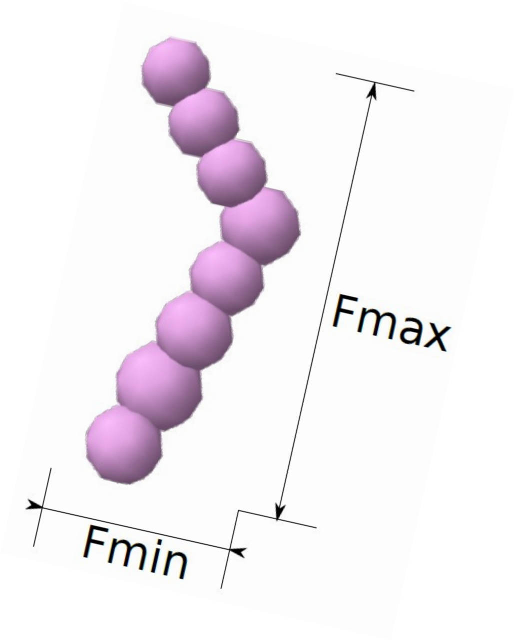

Figure 36 Example of Feret distances for aspect ratio with the minimum Feret diameter and maximum Feret diameter shown.

The Bow particles with constant EQPC were selected for implementation in the DEM simulations since they balanced complex particle geometry with representative shape while still being less computationally intense than varying particle size and shape across a larger range. In order to match the actual distribution of aspect ratios in the HPMC material the relative amounts of the seven different Bow particles were adjusted. Since particle size distributions were not used in the DEM model, the variation in aspect ratios was the key geometrical factor used to influence the behavior of particles in the simulation including particle interlocking. The Bow particles had aspect ratios from 0.32 to 0.86 as shown in **Table 18**. The measured cumulative distribution of aspect ratios for K100M DC HPMC along with the matching distribution for the Bow particles used in the simulation is shown in **Figure 37**.

Table 18 Aspect ratio, Feret diameters and relative amounts for Bow particles used in the DEM simulations.

Particle number*	Aspect Ratio	F_{min} (mm)	F_{max} (mm)	Distribution of particles used in model (%)
1	0.32	1.37	4.35	1.71
2	0.39	1.68	4.31	13.00
3	0.42	1.87	4.42	5.57
4	0.48	1.90	3.93	11.14
5	0.57	2.23	3.88	16.72
6	0.74	2.45	3.29	31.58
7	0.86	2.68	3.11	20.28

*Particle numbers referenced from **Figure 34**.

In addition to the Bow particles, the simulation was also run using spheres for comparison. Spherical particles are almost universally utilized for DEM simulations due to the simplified shape and reduced computational burden but do not represent elongated particles well (39, 184).

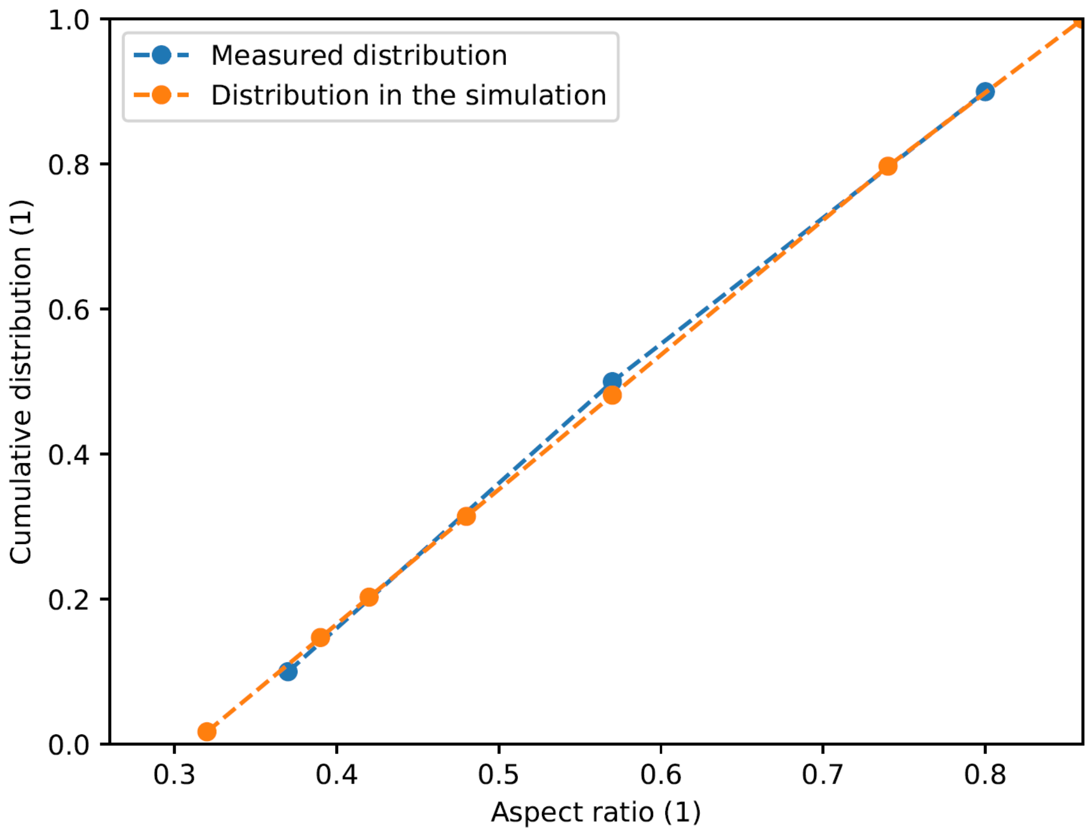

Figure 37 Correlation of aspect ratios for experimental and modeled HPMC. HPMC K100M DC measured experimentally in blue. Bow shaped particles used for the DEM models in orange.

2.3 DEM model

Coupi Polyphysica DEM code was used to perform the calibration and simulation runs. The model is described in more detail (178, 185) and has been applied successfully for simulating a number of different engineering problems (186-190). Polyphysica contact representation implements a full JKR adhesion model (191, 192) for normal force computations which reduces to a standard Hertzian contact model in the absence of adhesive forces. Tangential forces include iterative computations for the elastic part and

Coulomb friction model. The contact model also includes inelastic viscous force damping based on the coefficient of restitution (CoR) for each material.

Overlapping multi-spheres were utilized to represent the more complicated shapes for HPMC particles. This approach has been used to replicate complicated granular materials and can provide some degree of surface roughness depending on the number of spheres. The number of spheres per particle needs to be balanced by the total number of desired particles and run time for the DEM model to balance the computational speed (193, 194).

A triangular mesh was used in the DEM model to represent the physical bodies in the system. The number of triangles used to create the mesh was reduced from the initial design in order to reduce the number of interactive parts by 90% while still preserving the representation of the equipment. This reduction in the number of interactive parts allows for reduced computations and faster time to run the simulations. An example of the triangular mesh (initial and reduced) is included in **Figure 38**.

The main limitations for this model is that particle breakage and global deformations such as bending and twisting of the particles were not incorporated into the model due to the high computational requirements for the significantly large number of particles and related collisions.

Figure 38 Representation of the triangular mesh used to represent the LIW feeder screws. Purple was the initial mesh and Gold was the reduced mesh resulting in 90% fewer interactive parts while still maintaining the overall geometry.

One of the challenges involved with DEM simulations is the computational time since the particle-particle contact model must track and compute distances and forces on each particle collision. Moreover, DEM requires a very small time step due to physical requirement for the characteristic time to capture the collision of the solid bodies. These collisions are especially frequent with large numbers of particles and dense flows where each particle moves freely and independently of its nearest neighbors (195) and the number of potential contacts increases significantly with increasing number of particles used for the simulation and with size and shape differences between the particles.

The DEM model of the LIW feeder utilized particle properties determined by SEM images and DEM simulations of the HPMC powder characterization tests.

2.4 Loss-In-Weight Feeder Equipment

The GEA Loss-in-Weight compact feeder (GEA, Columbia, Maryland) was used to experimentally evaluate HPMC K100 DC. This standalone equipment is identical to the feeders utilized in the GEA CDC-50 equipment designed for continuous direct compression and is shown in **Figure 39**. It uses a twin screw conveying system to dose powders at a target feed rate. There is a a horizontal impeller above the screws to ensure consistent filling of powder into the screws.

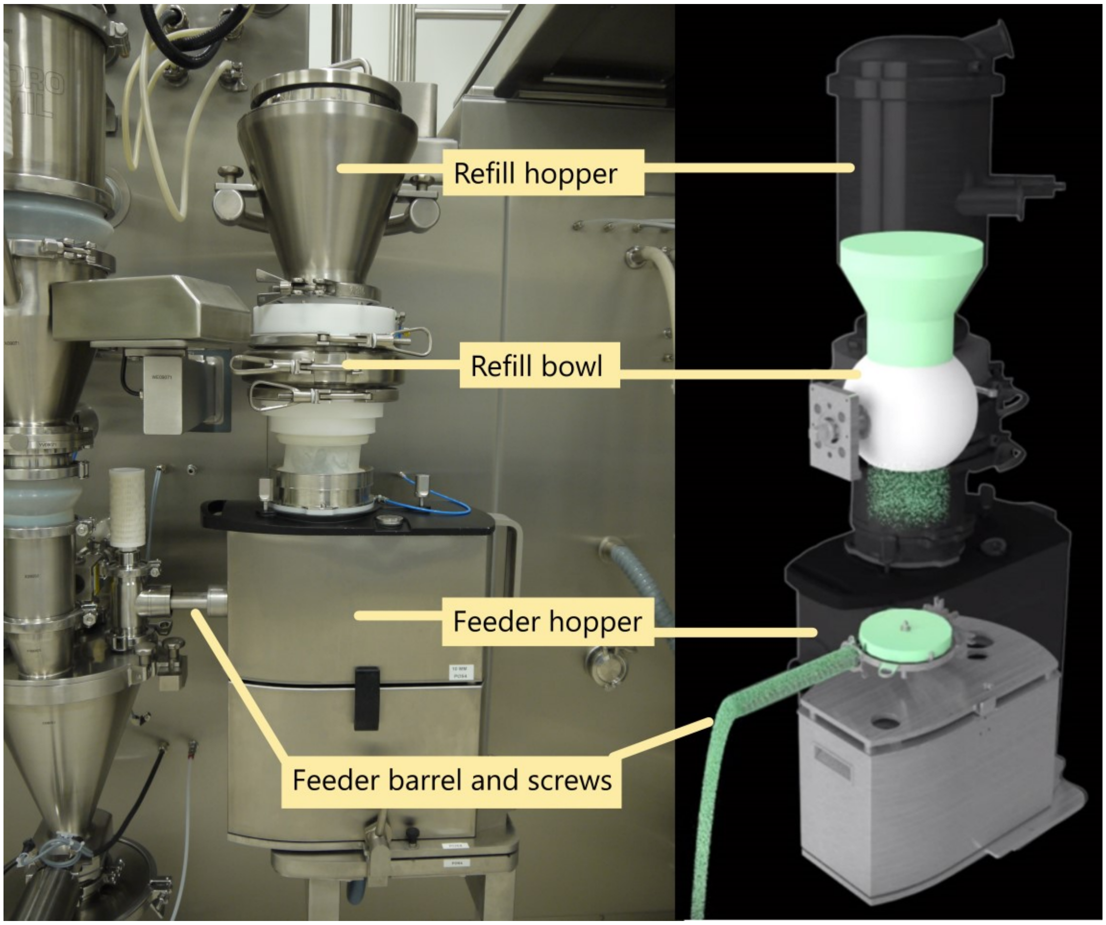

Figure 39 Compact feeder diagram and photo with relevant parts identified.

There are two modes of operation with the GEA loss-in-weight feeders: gravimetric and volumetric. The gravimetric mode is the typical mode of operation where the actual mass flow is calculated based on the loss in weight detected from the load cells. The load cells weigh the entire feeder with the screws, barrel, and hopper including the powder in the system. The weight is the difference between actual weight of the feeder with powder and the weight of the feeder without powder. There is a feedback control loop where the screw speed is continuously adjusted to keep the mass feed rate at target.

A refill of the material is triggered when a predetermined amount of material is remaining in the hopper. When additional material is added it is necessary for the feeder to switch from gravimetric mode (measured mass per time with adjusting screw speed) to volumetric mode (fixed speed based on feed factor array and the mass of material). If the system detects a significant upset in the mass flow it can also switch to volumetric mode. In order to improve the accuracy during volumetric feeding, the system utilizes a feed factor to determine the required screw speed based on the expected amount of material in the hopper. The feed factor is a measure of the mass fed per screw revolution and is dependent on the material, the amount of material in the hopper and the type of feeding screw utilized (196). Only the gravimetric feeding portion was modeled for the DEM simulation of the LIW feeder.

The LIW feeder was set up with 20 mm concave screws and standard feeder paddles. The feeder has different sized outlet screens which can be placed over the barrel at the end of the screws, but even the largest screen created significant back pressure and caused the screws to stop with HPMC, so no mesh screen was used on the feeder outlet.

As described in **Chapter 2**, the HPMC K100M DC was tested with mass flows of 0.278, 2.083 and 4.167 g/sec and approximately 450 g of material was fed through the screws. The tests were repeated multiple times using the refill hopper to add more material and the mass feed rate, mass feed rate RSD, and screw speed were monitored to evaluate the overall performance of the feeder with HPMC.

The CAD model of the LIW feeder including the hopper, impeller, barrel, and screws was imported into the Coupi Polyphisica DEM model as shown in **Figure 40**. The equipment was triangulated to ensure accurate representation of the equipment geometries balanced with having too small or elongated triangles which would slow down the computations.

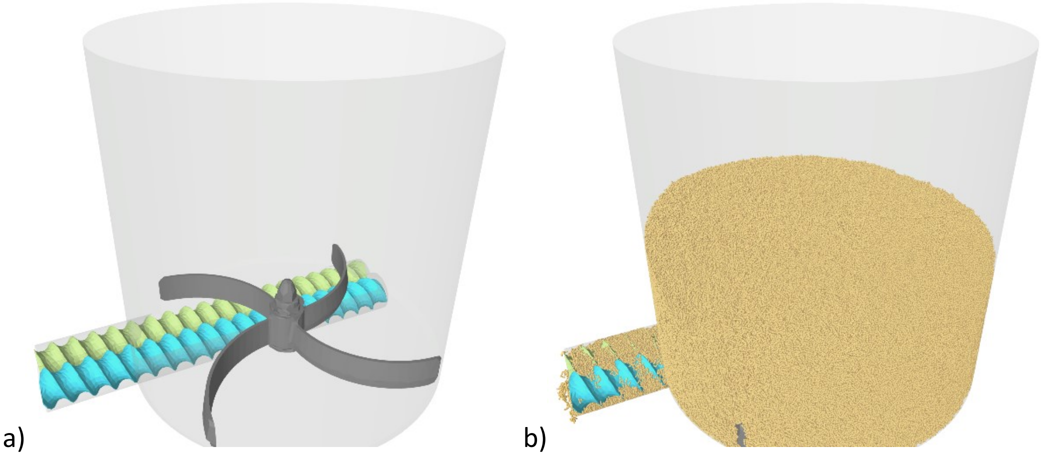

Figure 40 Coupi Polyphisica model of GEA loss-in-weight feeder a) empty and b) with 600 g of simulated Bow particles in the hopper and being fed through the screws.

The LIW feeder equipment is made of polished stainless steel for all product contact surfaces. The shear modulus for the steel was reduced from 77-79 GPa for the different types of steel to 0.1 GPa for the DEM model. This was done because material with lower shear modulus (stiffness) will have larger characteristic times (duration) for the collisions that can be accurately resolved with an increased time step (by 100x) which significantly reduces the computational load when running the simulation with minimal impact on the simulation accuracy. The process is driven mainly by the particle geometry, friction and cohesion, hence decreased shear modulus should not significantly affect the results. The generalized steel parameters which were used for the DEM model are shown in **Table 19**.

The coefficient of restitution (CoR) determines how much energy is absorbed during collisions. It is the ratio between the particle velocities before and after the collisions based on how much energy is absorbed by the material during the collisions where CoR = 1 implies material that is perfectly elastic and CoR = 0 implies completely inelastic material (all collision energy is dissipated). A CoR value of 0.1 was used for the model and has been shown to have no impact on the results for other similar DEM models and materials over a wide range of values (197).

The Coulomb friction was determined during the initial DEM calibration simulations where increasing > 0.2 did not affect the results so it was kept at 0.2 for steel and is discussed in more detail for the particles.

Table 19 Generalized Steel Parameters for DEM.

Parameter	Value	Description
G	0.1 GPa*	Shear modulus for steel
ν	0.31	Poisson ratio
μ	0.2	Coulomb friction (static/dynamic)
CoR	0.1	Coefficient of restitution
ρ	2,500 kg/m^3	Material density

* Lower than the actual value of 77-79 GPa for different types of steel.

The barrel and screw were cut-off in the DEM to reduce the path for the particles before they exit the LIW feeder which allowed for faster computations. It was confirmed that the material flow in the screw and barrel becomes uniform after 5-6 sections of the screw and has no back flow. At this point the material is only conveyed through the length of the barrel. Therefore, cutting the barrel and the screws for the DEM model at this point does not affect the overall feed rates in the simulation.

The LIW feeder simulations were run using the highest experimental mass feed rate of 4.167 g/sec in order to reduce the model run time, but one simulation was performed at the medium speed of 2.083 g/sec to confirm the model for different feed rates. The lowest experimental speed was not simulated as the simulation run time would have been too long. The simulation utilized Bow particles to evaluate the particle size scale effects with 1 mm diameter (EQPC) spheres run for comparison. The LIW feeder simulations utilized the material parameters established from the DEM calibration tests and shown in **Table 18**, **Table 19** and **Table 21**. Overall run time of the simulations varied with runs split using different hopper fill levels of 600 g, 360 g and 220 g. The model utilized a screw speed based on the experimental data for HPMC. The data files were analyzed using post-processing algorithms written in Python and Lua.

2.5 DEM Material Calibration Process

There are many different approaches that have been used in calibrating particle properties for DEM from simple bulk property correlations to advanced neural networks (36, 175, 198-202). One common approach is to place the particles directly into the desired DEM model and adjust the particle properties to match the experimental results. The downside to this approach is that the parameters may be process specific and may not work if applied to different DEM models. For this work, DEM models were created for a number of characterization tests which were used to calibrate the material and contact properties for model.

Image analysis of HPMC K100 DC was used to determine the desired DEM particle shapes and aspect ratios. It was not feasible to simulate the actual particle size or the particle size distribution of HPMC in the DEM simulations as the number of particles involved would require unrealistically large computational resources. To reduce the computational requirements, larger sized particles were implemented for the DEM simulations. These particles were still much smaller than the components for the material calibration and LIW feeder models. The collection of particles in the DEM model represent the bulk of the material and the size of the particles can be considered as the “resolution” of the model.

The coulomb friction coefficient used for DEM particles was not measured directly and was based on nominal value as it was shown not to affect our calibration when coulomb friction μ > 0.3. It was initially evaluated using the angle of repose DEM calibration from 0.3-1 with minimal impact to the outcome as shown in in **Figure 41**. The value used in the simulations was μ = 0.5 which was the same as values used in other similar simulations (203, 204).

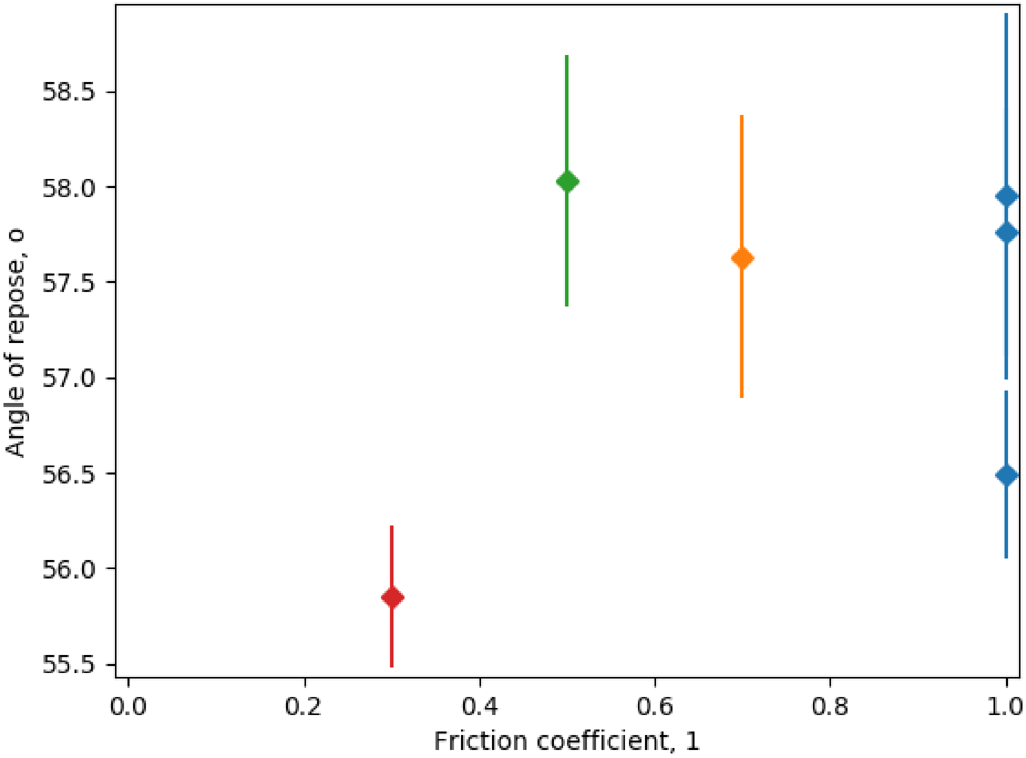

Figure 41 Influence of the friction coefficient (coulomb friction) on the angle of repose results. Mean and standard deviations indicated. Color indicates different friction coefficients evaluated.

Once the particle shape, particle size, density and coefficient of friction were determined, it left the particle cohesion to be derived via the angle of repose simulation. Overall the cohesion depends on particle shape, size, friction, interparticle forces, as well as the number and type of contacts. The cohesion is represented in the DEM simulation in terms of surface energy in addition to the particle shape, size, etc.

The bulk density DEM simulation was used to determine the particle density of the DEM particles. This was done by using the HPMC true density as a starting density and changing the DEM particle density until the simulated bulk density agreed with the experimentally determined value. The true density for HPMC could not be used as the DEM particle shape was smooth while the HPMC had many cracks and crevices as shown in **Figure 7b** and **d**. The material's bulk density depends on particle shape, size, coulomb friction, cohesion, and particle density. As the DEM shape and size were already determined through direct measurements, the coulomb friction was specified, and the cohesion was derived from angle of repose the apparent density was the only independent parameters to be established. The determination of the surface energy through the angle of repose was rechecked with the initial true density and the adjusted apparent density and confirmed not to be impacted within that range.

After the DEM parameters had been established there was an independent validation performed by simulating the rotating drum flow tests and comparing results. The flow test is mainly affected by the particle shape, friction, and cohesion. Matching the experimental results for the rotating drum confirmed the validity of the selected parameters for the DEM model.

To decrease the computational requirements for the LIW model, the particle size was further increased from the calibration simulations to reduce the total number of particles in the LIW model by a factor of 7 which reduced the computation time for the simulations. The shear modulus was also reduced to increase the time step without impacting accuracy since it has minimal effect on accuracy for the particle velocities that occur during LIW feeding.

Dimensional analysis was used to scale the simulated materials from the calibration tests to what was eventually implemented in the LIW feeder model, while balancing the need to reduce the simulation computation time with representative results. Once the model properties were identified the LIW feeder equipment was modeled and multiple DEM LIW feeding simulations were performed and compared to experimental data.

2.6 DEM Material Calibration using the Bulk Density Test

The bulk density for HPMC K100M DC was performed experimentally using a volumetric bulk density tester (Scott Volumeter) shown in **Figure 42**. The empty 16.4 mL sample cell was weighed and placed under the volumeter. Powder was gently poured into the top of the volumeter to allow for the powder to be conditioned and aerated while falling between the alternating glass plates until the sample cell was completely full. Excess material above the sample cell was carefully removed using a flat spatula. The mass of material added to the sample cell was measured and the bulk density was calculated according to the formula: bulk density = material mass / volume of the cell.

The bulk density test was simulated using DEM with a cylindrical hopper and 16.4 mL cylindrical sample cell made of steel with approximately 20,000 particles and 170 thousand interactive parts for the equipment surfaces. The hopper contained 4 plates that prevented material from falling directly into the open cell and provided material with some aeration to ensure loosely packed material filled the test cell. The powder was generated using small portions distributed in space above the hopper. The sample cell was rotated slowly with a small constant angular speed of 1 revolution every two seconds to ensure distributed filling of the cell with the simulated particles and the bulk density determined for the modeled particles.

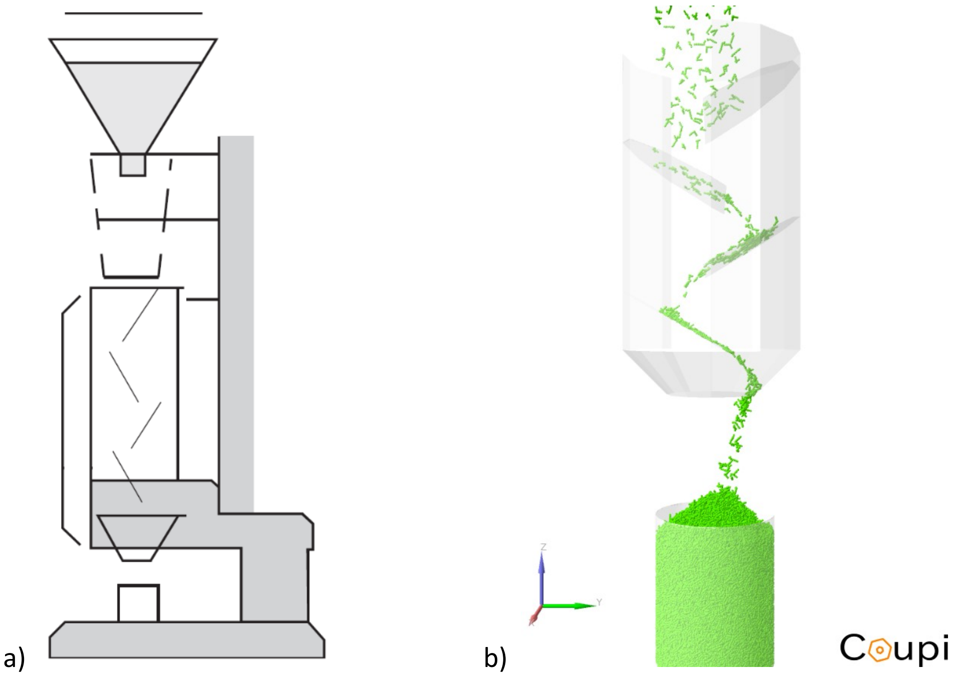

Figure 42 a) Bulk volumeter for measurement of bulk density image from (205); b) Coupi Polyphysica DEM simulation of the bulk density test.

2.7 DEM Material Calibration using Static Angle of Repose

When a powder is poured onto a surface, a heap is formed (206). It is well established that both the angle of repose and the heap shape strongly depend on the combined particle properties including the cohesive properties (153). A highly cohesive powder forms a tall irregular heap with a high angle of repose while a non-cohesive powder forms a regular conical heap with a low angle of repose (154). Therefore, a precise measurement of the heap shape and angle of repose can provide useful information about the physical properties of the powder.

The angle of repose measurements for HPMC K100DC were performed experimentally on the GranuHeap (Granutoools, Awans, Belgium). A powder heap was created on a 40 mm diameter cylindrical support plate using powder placed into a slightly larger diameter initialization tube. When the initialization tube was raised the powder was deposited onto the cylindrical support plate to form a heap. The equipment used a CCD camera to capture 16 images around the heap during a slow, controlled rotation of the test plate to view different heap orientations so that any asymmetric heap shapes are captured. An image recognition algorithm determined the air/powder interface and calculated the angle of repose which is based on the angle of an isosceles triangle with equivalent surface area as the powder heap's projected image. The angle of repose was computed for each of the images and the average value determined. The test was performed in triplicate for the HPMC K100M DC material. The equipment was cleaned and a fresh sample used each time.

The DEM model of the angle of repose was run using 64,000 particles with 500,000 interactive parts from the surfaces and is shown in **Figure 43**. The projection area was created by projecting particles perpendicular to the support plate on a rectangle that is specified by a view angle as shown in **Figure 44**. There were also 16 view angles used in a range from 0 to 2π to compute the deviation of the heap projection similar to the methodology used by the GranuHeap. A plane was separated to 1000 × 1000 equal cells for quantification. The cell was considered to be filled if at least one point of a particle projection was inside the cell. The height of the heap *h* was calculated as the distance between the center of the highest filled cell and the base.

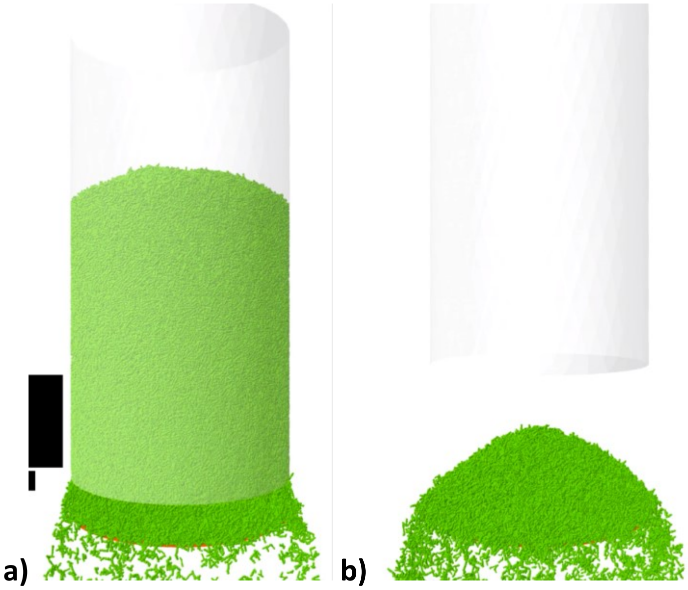

Figure 43 Angle of repose DEM simulation for bow particles in green showing a) outer cell being lifted; b) heap of particles being formed on platform.

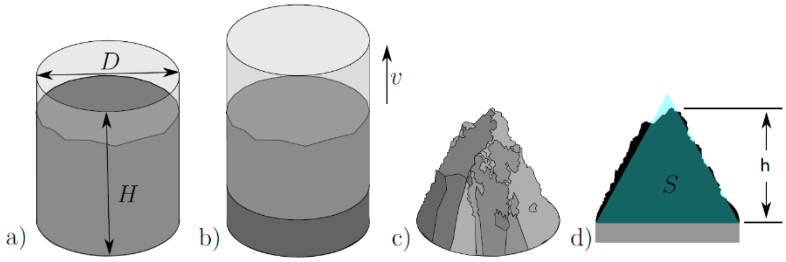

Figure 44 Scheme of the DEM simulation for angle of repose. **a)** Filling up the open initialization cylinder with height *H* and diameter *D*; **b)** pulling up the cylinder with a low constant speed *v*; **c)** heap is formed; **d)** determination of the heap shape projection, calculation of the projection area, heap height h, and creation of an equivalent surface area isosceles triangle *S*.

Based on the projection area of the heap an isosceles triangle with the same surface area was created. The base side of this triangle was considered to be the diameter of the support. The height of the isosceles triangle is h = 2*S / D where S is the area of the isosceles triangle and D is the diameter of the base plate. The angle of repose is the internal base angle between the base and the leg of the isosceles triangle which can be calculated by the formula: $\alpha = \arctan(2*h / D)$. The average and standard deviation of the angle of repose was calculated from each of the 16 view angles.

2.8 DEM Material Calibration using Flow Angle from GranuDrum

Powder flow under dynamic conditions was studied experimentally using the GranuDrum (Granutools, Awans, Belgium). The instrument consists of a clear cylindrical drum with an inner diameter of 84 mm and a width of 20 mm which was half filled with the HPMC sample. The drum with powder rotates around the axis at an angular velocity in a range from 2 to 60 rpm. The rotating drum is backlit and utilizes a CCD camera to capture images of the powder as it is flowing. For the powder testing, speeds of 2 to 20 rpm (every 2 rpm) and then 20 to 60 rpm (every 5 rpm) were used. The powder was initially conditioned for 15 seconds and then 40 images were acquired at each of the 18 speeds. The software detected the interface of the powder/air and determined the flow angle, also referred to as the dynamic angle of repose, which was computed from the average angle measured at the center of the powder/air interface. A low value of the flow angle corresponds to better powder flowability. The flow angle can be influenced by a wide set of parameters, but mainly friction, cohesive forces (Van der Waals, electrostatic and capillary forces), and the particle morphology (152, 207, 208).

The DEM simulation of the GranuDrum characterization test used approximately 38,000 particles and 316 thousand interactive parts for the equipment surfaces and shown in **Figure 45**. To determine the flow angle a projection of all particles in the drum on a plane perpendicular to the drum's axis was created and the interface position was determined with a resolution of 800 x 800 cells to cover the diameter of the drum. A cell was considered filled if at least one point of a particle's projection was inside. This was performed every 50 msec over 15 revolutions of the drum to create the "images" utilized for the calculations. Drum speeds of 10, 20, 30, 40, 50 and 60 rpm were performed for the simulation. The mean interface position was then determined at the center of the interface similar to the equipment software. The flow angle was then determined as being the slope of the mean interface.

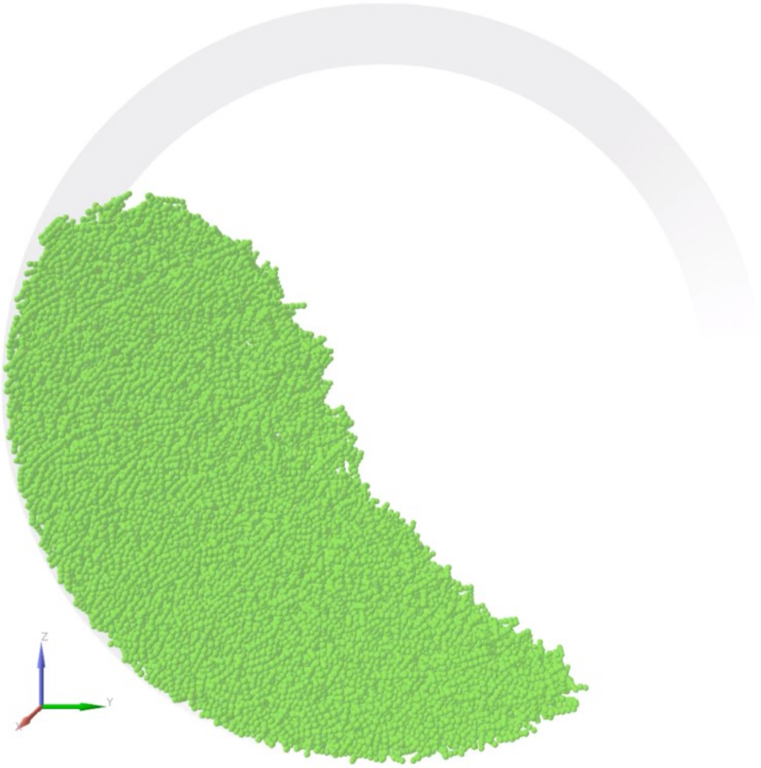

Figure 45 DEM simulation of bow particles in green rotating at a drum speed of 40 rpm.

2.9 Scaling of particle size and mechanical properties

The calibration simulations were performed with 1.2 mm Bow particles to establish the particle properties to utilize in the LIW feeder model but when these 1.2 mm Bow particles were attempted in the LIW feeder simulation the computation times were excessively long. In order to shorten the time required for computations, it was necessary to reduce the number of particles required for the simulation by increasing the Bow particle size to 2 mm. This resulted in 4.6 times fewer particles being required and decreased the simulation run time by a factor of 7. Dimensional analysis was used to scale the particle properties determined for the 1.2 mm particle in the calibration tests. **Table**

20 includes the parameters that influence the particle properties in the simulations for the calibration tests and the LIW feeder model.

Table 20 Particle parameter description used in DEM model.

Parameter	DEM Units	Description
γ	Mt^{-2}	Surface energy
G	$ML^{-1}\,t^{-2}$	Shear modulus
ρ	ML^{-3}	Density
g	Lt^{-2}	Free fall acceleration
d	L	Particle (characteristic) size
f	t^{-1}	Frequency for feeder screw operation
μ	1	Coulomb friction
D	L	Process equipment characteristic sizes

*These parameters were determined via the DEM characterization work and scaling analysis.

Where *L* is in the length dimension, *M* is in the mass dimension, and *t* is in the time dimension. Assuming that d / *D* « 1, and not considering processes that include a frequency, there are the following five physical parameters to combine into dimensionless constants: surface energy *γ*, shear modulus (stiffness) *G*, density *ρ*, free fall acceleration *g*, and particle size *d*. Dimensional analysis is a technique for scaling (209) that is commonly used in DEM to scale multiple parameters. The number of dimensionless groups required to define a problem equals the total number of variables, (size, density, etc.) minus the fundamental dimensions (time, length, etc.). In this case there are 5 variables and 3 independent dimensions resulting in 2 independent dimensionless parameters considered as X and Y.

For such dimensionless parameters X and Y, the ratios of the cohesion force and elastic force (F_c/F_e) can be used as well as the cohesion and mass force in the following form (F_c/F_m) as the ratio between the “cohesion force” and the “gravitation force”:

$$Y = \frac{1}{\rho g}\frac{\gamma}{d^2} = \frac{\gamma d}{\rho g d^3} = \frac{F_c}{F_m} \quad \text{and} \quad X = \frac{\gamma}{dG} = \frac{\gamma d}{d^2 G} = \frac{F_c}{F_e}$$

3 RESULTS AND DISCUSSION

The Bow shaped particles were selected over the capsule shape and the more accurate HPMC Replica shape to balance between representative particle geometry and the computational requirements that determine the time required for the simulation to run. As there were seven different Bow particles included with different aspect ratios the relative amounts were varied to represent the distribution of aspect ratios observed for HPMC K100M DC. Some of the calibration tests and the LIW DEM model used sphere, HPMC replica and capsule shaped particles for comparison of results.

The shear modulus and coulomb friction were fixed after initial evaluations identified these as appropriate and they were confirmed via the calibration tests to establish the density and surface energy (cohesion). The time step used in the simulations was 1 x 10^{-6} seconds. The DEM LIW feeder simulations required between 558,000 and 1,500,000 particles composed of 2.5 million to 12 million spheres (variation depending on the amount of material in the hopper) with 25,000 interactive parts in the equipment which were simulated for the Bow particles. The run with 1 mm EQPC spheres instead of the Bow particles utilized 1,014,000 particles for the simulation. Additional parameters used for the LIW DEM model were identified via the calibration tests and scaling validation studies and are described in subsequent sections.

3.1 DEM Material Calibration using the Bulk Density Test

When the bulk density DEM simulation was run for the various particles it produced bulk density values which were larger than the actual HPMC K100M DC ρ_{bulk} = 0.302 g/ml (±0.001). The capsule shaped particles significantly overestimated the bulk density, giving 0.443 g/ml as a result of the smooth shape and dense packing which could be achieved.

The HPMC Replica particles resulted in a very close match to the actual material with bulk density of 0.292 g/ml owing to their complicated and more representative morphology. However, these were simulated with a surface energy of zero to give the lower bound for the density. Additional calibrations were not performed as this shape was too computationally intense to use in the DEM LIW feeder model.

The Bow particles also overestimated the bulk density from the test and were in-between the HPMC Replica and Capsule shaped particles with bulk density of 0.370 g/ml. The difference in simulation and actual results was attributed to the smooth surface and simple morphology for the Bow particles compared to the actual HPMC. There could also be differences in packing from the particle size distribution for HPMC while the Bow particles only varied in aspect ratios and not size. The particle diameter of 1.2 mm was approximately 11 times higher than the actual HPMC particles, however this is not expected to impact the bulk density as the volume of the testing chamber is sufficiently larger than the particle size.

The measured true density via helium pycnometer for the HPMC K100 DC was 1.315 g/ml, which is the density of the material excluding the volume of any open or closed pores. The true density measurement is performed using helium gas at a high pressure which penetrates every surface flaw down to one Angstrom and can even capture occluded pores (68). Based on the SEM images of the particles in **Figure 46**, the actual HPMC particles have a very rough surface with channels, cavities, and holes. However, the particles utilized for the DEM model are completely smooth without any surface variability. The lower apparent density of the Bow particles resulted in the higher bulk density for the DEM simulation.

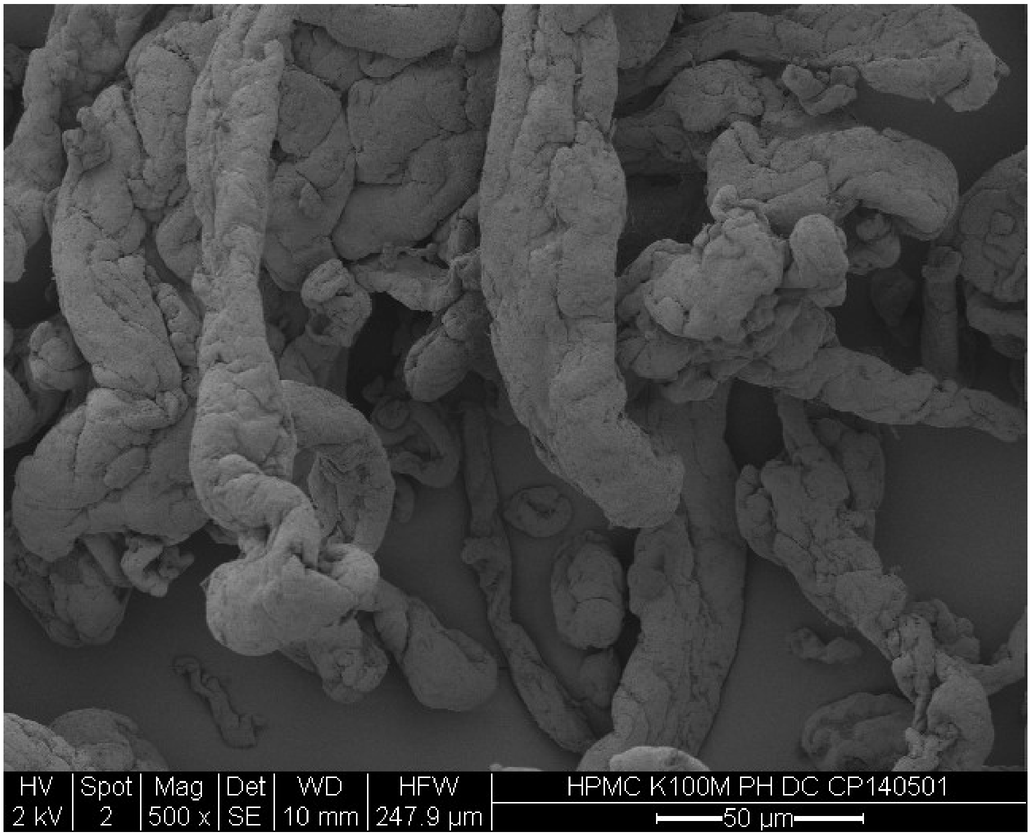

Figure 46 Representative SEM image of HPMC K100M DC at a magnification of 500x showing various cracks and crevices in the HPMC particles.

The material density is one of the driving parameters for the LIW feeder system as the conveying screws will feed material based on a volume of particles that can fill the screw flight and be conveyed out of the feeder. As a result of the overestimation of the bulk density with the Bow particles it was necessary to adjust the apparent density of the simulated Bow particles from the actual 1.315 g/ml for HPMC to 1.085 g/ml. The value was selected based on the correlation shown in **Figure 47** which simulated the bulk density of the Bow particles using different apparent densities. The use of a modified apparent density for the simulated particles is justified based on the surface differences with the simulated particles which are completely smooth.

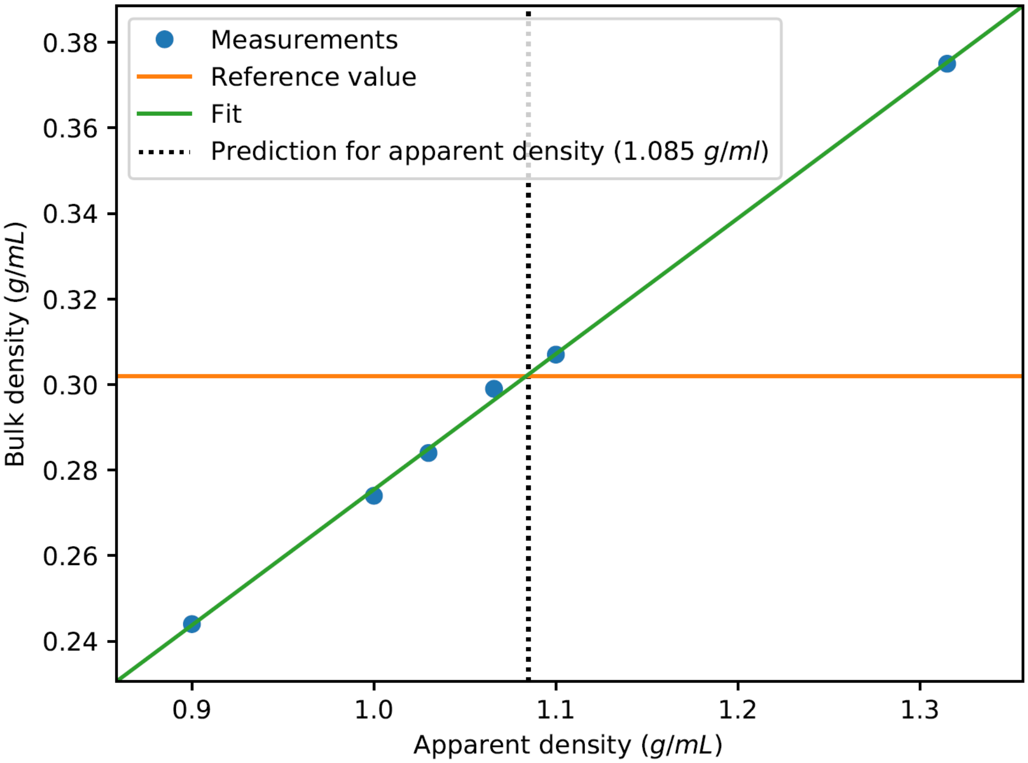

Figure 47 Relationship between material apparent density and bulk density simulated in the Scott Volumeter test. Orange line shows the reference value for HPMC K100M DC. Dotted line shows the value of apparent density in the DEM simulation that gives the target experimental bulk density of bulk density.

3.2 DEM Material Calibration using Static Angle of Repose

Results from simulating the angle of repose from the GranuHeap are shown in **Figure 48**. For reference, materials with angle of repose 46-55 are considered poor flow and 56-65 are classified as very poor flow (164). When the surface energy (*γ)* used in the simulation increased, the measured angle of repose also increased because the surface energy is the main parameter affecting cohesion besides the particle geometry. There was minimal impact when changing the particle size from 1.2 to 1.5 mm. This led to the initial selection of surface energy (*γ)* of 0.06 N/m for the material DEM properties based on the correlation in **Figure 48** and matching the experimental angle of repose for HPMC K100M DC. This surface energy value was then confirmed using the GranuDrum simulations for the dynamic angle of repose.

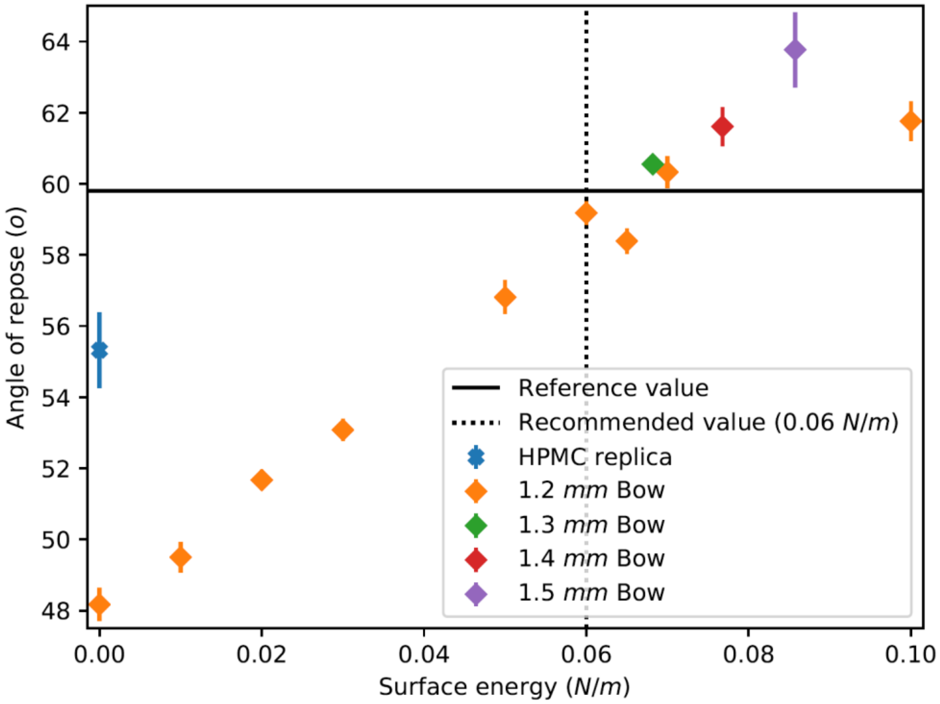

Figure 48 Angle of repose measurements for different shapes of the powder particles with a range of surface energy. Means and standard deviations are shown.

3.3 Verification of DEM Material Parameters using Flow Angle from GranuDrum

The powder flow in a drum was used as an independent verification of the selected surface energy and other particle parameters such as apparent density, particle shape, coulomb friction and particle size intended to be used in the DEM model. The dynamic angle of repose is sensitive to the simulated powder cohesion as poor flowing powder will have a very high angle of repose in the rotating drum. The dynamic test of the material flowing in a rotating drum is affected differently by particle properties compared to the static tests of bulk density and angle of repose and served as verification of the determined parameters.

For HPMC K100 DC the average flow angle increased from a drum speed of 2 rpm and reached a maximum at 8 rpm before decreasing and flattening out after 30 rpm as shown in **Figure 49**. There was less variability between the two replicate tests at speeds above 30 rpm. For reference, a moderately flowing material like lactose had a drum flow angle of 35-40 degrees at low drum rotation (154) where HPMC had a flow angles of 58-64 degrees indicating that the material is still considered cohesive. At higher drum speeds it is likely that the powder starts to become fluidized as both the flow angle and standard deviation decrease.

The DEM simulation for the powder flow in a drum was initially performed using the true density of the actual HPMC material of 1.315 g/ml with the surface energy determined from the Angle of Repose $\gamma = 0.06$ N/m. Simulations were performed at drum rotation speeds of 10, 20, 30, 40 and 60 rpm and shown in **Figure 49**.

After it was determined that the apparent density for the Bow particles needed to be adjusted from the bulk density tests, additional simulations were run for the GranuDrum with the corrected apparent density. The change in density had a minimal impact to the determined flow angles. When changing the surface energy from $\gamma = 0.06$ N/m to $\gamma = 0.1$ N/m while keeping the shear modulus fixed the flow angle increased significantly at 60 rpm demonstrating that the GranuDrum simulation is sensitive to the simulated particle properties as shown in **Figure 49**.

The flow angles for the simulated Bow particles matched well with the experimental results for HPMC K100M DC. The behavior of the powder close to the edge of the drum was slightly different between the simulation and the HPMC experiments as can be observed in **Figure 50,** but as the flow angle is measured near the center of the drum these edge effects did not impact the results.

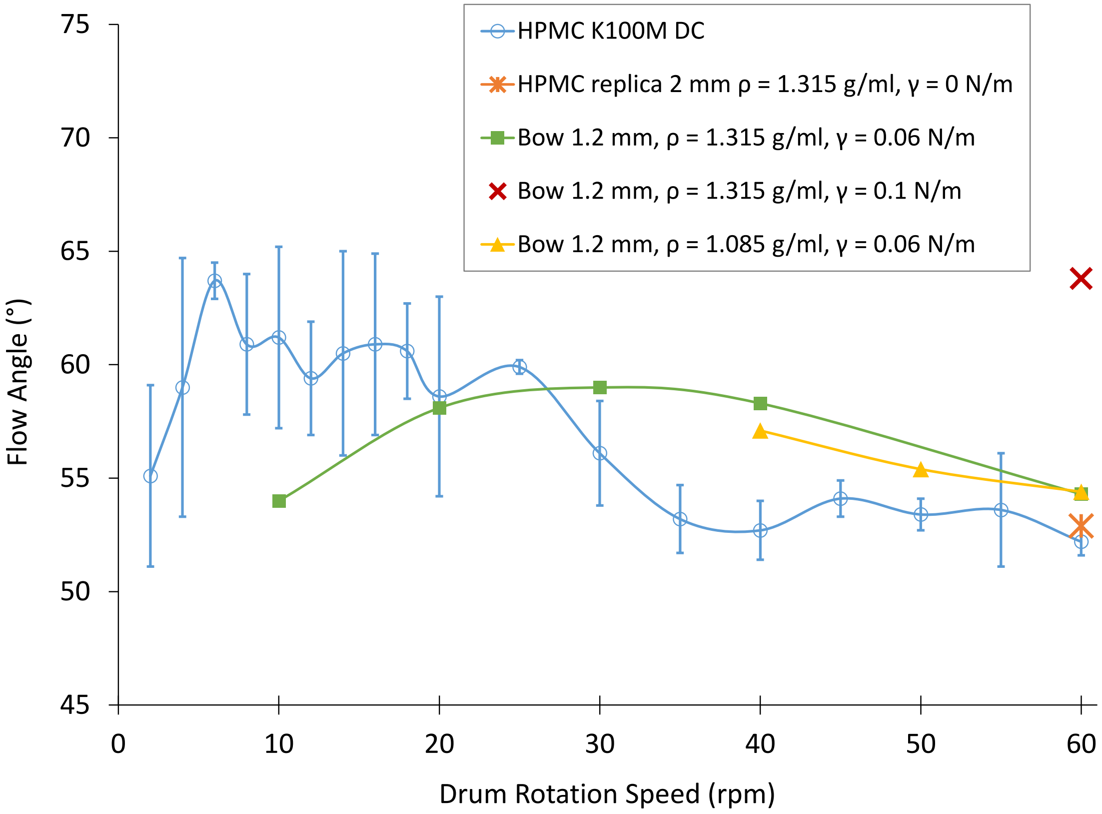

Figure 49 Flow angle for HPMC and simulated particles for the GranuDrum at different rotation speeds. Means and standard deviations are shown.

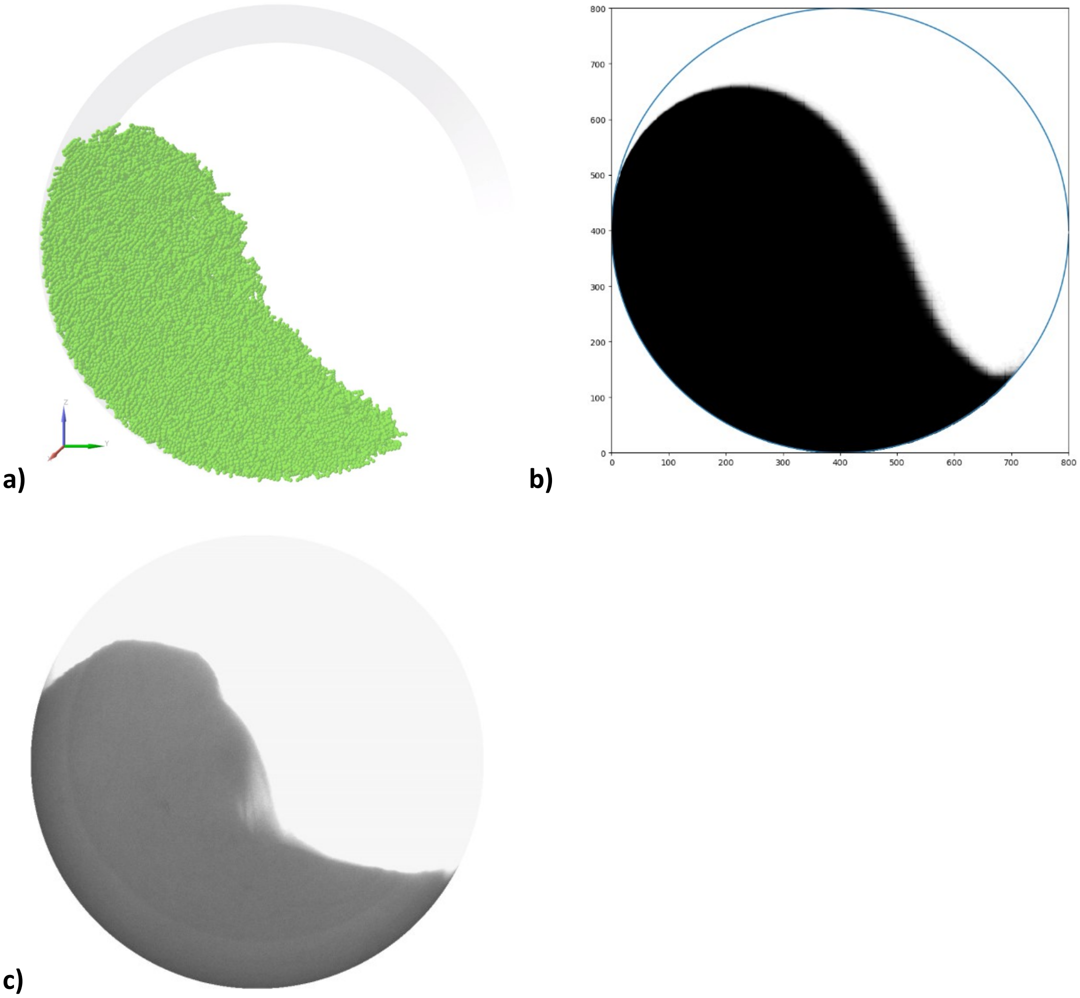

Figure 50 GranuDrum powder in a rotating drum **a)** DEM simulation of 2 mm bow particles at 40 rpm; **b)** Composite image of 1.2 mm Bow particles with 1.2 mm at 60 rpm; **c)** Experimental results for HPMC K100 DC at 40 rpm individual image.

3.4 Parameter Scaling Results

The initial calibration simulations were performed using particle size of d= 1.2 mm for the Bow particles. This size was selected for the LIW feeder model based on the 20 mm concave twin screw pitch (distance between the screw sections) of 10 mm, hence 10 mm / 1.2 mm = 8.33 providing sufficient particles in the screw section to avoid boundary influences. An example of the 1.2 mm Bow particles in the screw pitch is shown in ***Figure 51*** **(top)**.

The 1.2 mm Bow particles worked well for the calibration simulations, but LIW DEM model required significantly more particles and resulted in unacceptable simulation run times, even after the other steps to reduce the simulation time were taken (such as cutting off a portion of the LIW feeder barrel and reducing the number of component parts for the equipment).

One common way of reducing simulation run time is increasing the particle size used for the DEM model. Increasing the Bow particle size from 1.2 mm to 2 mm resulted in a 4.6x reduction in the number of particles required for the LIW feeder DEM simulations resulting in approximately 7x reduction in computation time. Increasing the particle size to 2 mm gives 10 mm / 2 mm = 5 particles across the screw pitch which should have been acceptable for boundary effects. An example of the 2 mm Bow particles in the screw pitch is shown in ***Figure 51*** **(bottom)**.

Boundary influences when the size of the particles are close to the size of the equipment can result in reduced bulk density and reduce the overall feed rate if the particle size is close to the volume that is being occupied. A similar screw feeding DEM study indicated boundary effects occurred for spheres occurred with 4 particles/section while 5 particles / section (1.54 mm diameter with 8 mm screw pitch) gave results close to experimental (210).

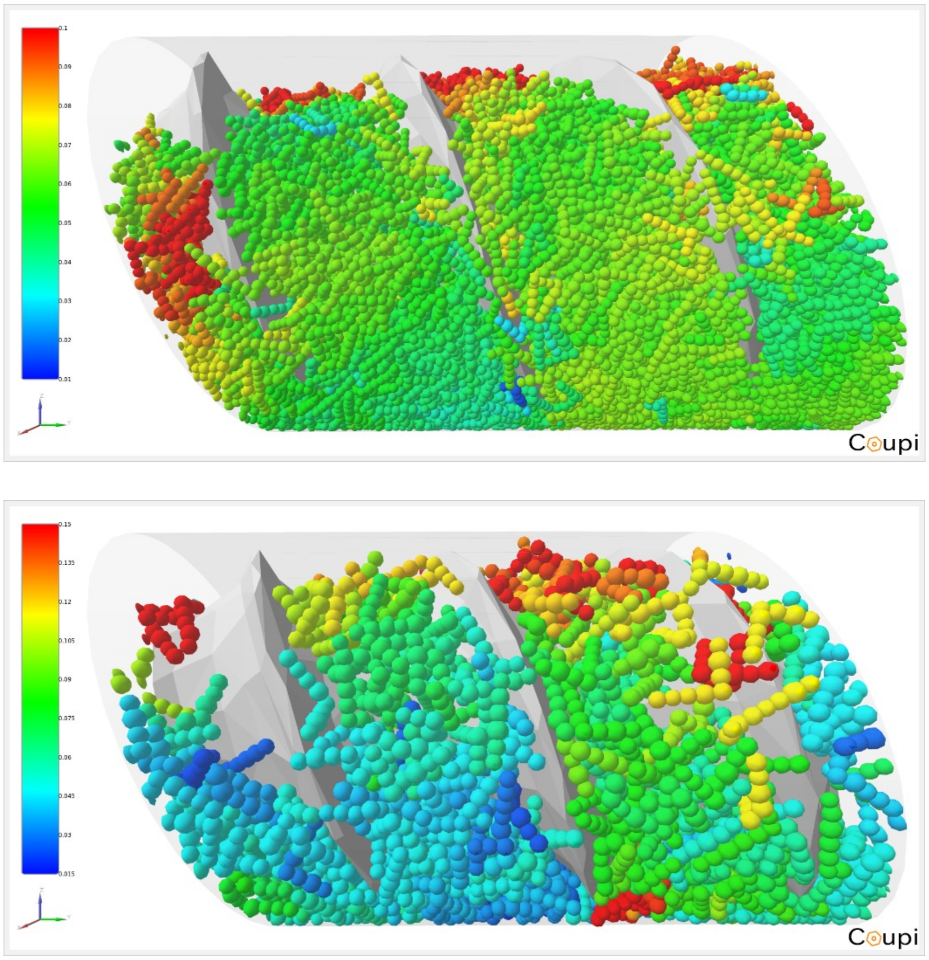

Figure 51 Example of particles filling the screw pitch in the DEM LIW simulation showing the different number of particles based on the size difference for (**top**) 1.2 mm Bow particles and (**bottom)** 2.0 mm Bow particles. Color indicates velocity for the particles in the Y direction where red is high velocity (0.15 m/sec) and blue is low 0.015 m/sec).

The larger 2 mm particles still resulted in an unacceptable simulation run time. To further reduce the simulation run time it was necessary to reduce the shear modulus. Initially a shear modulus G=0.1 GPa was selected for the calibration due to similar materials (211, 212) and shown to have little impact over a very wide range (213). This was done to reduce computation time by increasing the required time step to resolve any particle contacts. The shear modulus (*G*=0.1 GPa) corresponds to the shear wave speed: $\sqrt{\frac{G}{\rho}}$ when adjusted for units $\sqrt{\left(\frac{1\times10^{8}}{1.085\times10^{3}}\right)}$ which is approximately 300 m/s. This is significantly faster than the velocity of any particles or parts in the LIW feeder simulation which were less than 1 m/s.

This further 20 x reduction of the shear modulus from G = 0.1 GPa to 0.005 GPa allowed for an increased time step to resolve the particle contacts and resulted in a 4.5 x reduction in the computation time as determined by the reduction in the shear wave relationship between the different shear moduli as follows: when the densities cancel out, $\sqrt{\left({}^{G_1}/_{G_2}\right)}$ = $\sqrt{\left({}^{0.1}/_{0.005}\right)} = 4.47$.

This new shear modulus gives a shear wave speed of $\sqrt{\frac{G}{\rho}}$ = $\sqrt{\left(\frac{5\times10^{6}}{1.085\times10^{3}}\right)}$ which is approximately 68 m/s. This is still much higher than the velocity of any particle or parts in the LIW feeder simulation which were all <1 m/s.

Dimensional analysis was used to determine the surface energy when adjusting the shear modulus to avoid repeating the calibration simulations with the new parameters. It is necessary to reduce cohesion via adjusting the surface energy when the shear modulus is decreased. This is because as the material is softened by reducing the shear modulus the contact area during collisions increases. This leads to higher cohesion in the simulation if the surface energy is not adjusted accordingly.

The dimensionless parameter X was used for scaling with $X = \frac{F_c}{F_e} = \frac{\gamma}{(d*G)}$

representing the ratio between cohesion force F_c and elastic force F_e which determines how the particles behave in the DEM simulations. For 1.2 mm particles, a surface energy of γ = 0.06 N/m was determined using the angle of repose DEM simulation. In this case, the dimensionless X value that is kept constant for the LIW simulations when scaling is:

$X = \frac{\gamma}{(d * G)} = \frac{0.06\ \mathrm{N}/\mathrm{m}}{(1.2 \times 10^{-3}\mathrm{m})\left(1 \times 10^{8}\ \mathrm{N}/\mathrm{m}^2\right)} = 5 \times 10^{-7}$ based on the initial parameters.

In order to keep the granular material properties the same it is required to keep the scaling factor X the same. When the particle size was changed to 2 mm and the shear modulus changed to G = 0.005 GPa (5×10^6 Pa = 5×10^6 N/m^2) it required adjusting the surface energy. This was done via constant X such that $X = \frac{\gamma}{(d * G)}$ and solving for the desired γ with the new particle size and shear modulus:

$$\gamma = X * d * G = (5 \times 10^{-7})\,(2 \times 10^{-3}\mathrm{m})\,\left(5 \times 10^{6}\ \mathrm{N}/\mathrm{m}^2\right) = 5 \times 10^{-3}\ \mathrm{N}/\mathrm{m}$$

Resulting in the scaled surface energy γ = 0.005 N/m for d = 2 mm Bow particles.

Both the change in particle size from 1.2 mm to 2 mm and the reduction in shear modulus G from 0.1 to 0.005 GPa (and subsequent scaling of surface energy) were successful in reducing the computation times. The shear modulus was similarly adjusted from 0.1 to 0.005 GPa for steel. The computation times required for each of the LIW feeder simulations ranged from 192 to 432 hours depending on the particle size, amount of material, the feed rates, and the simulated time.

3.5 HPMC Experimental LIW Feeder Analysis

The main factor that can be controlled which influences the mass flow for a given material is the screws speed. As the mass flow deviates from the target set point the screw speed adjusts in a constant feedback loop to deliver more or less material as required. The other main factor is the density of the material entering the screws which is impacted by the material itself and the total mass of the material in the hopper. When the material is fed by the screw feeder the mass of material remaining in the hopper is reduced. This affects the density of the material and the screw speed needs to increase to keep the feed rate at target.

Experimental results for the mass flow of HPMC K100M DC at the medium feed rate of 2.083 g/sec and high feed rate of 4.167 g/sec are shown in **Figure 52** and **Figure 53**. The feed rate was kept close to target by the LIW feeder due to the feedback control loop.

It can be seen in **Figure 54** and **Figure 55** that as material is fed out of the hopper and the weight is reduced the screw speed is increased to offset the change in material density and keep the feed rate at the set point. The DEM LIW feeder model utilized the quadratic line fits for the screw speed based on the weight of the material in the hopper from the experiments in order to determine the screw speed in the simulations.

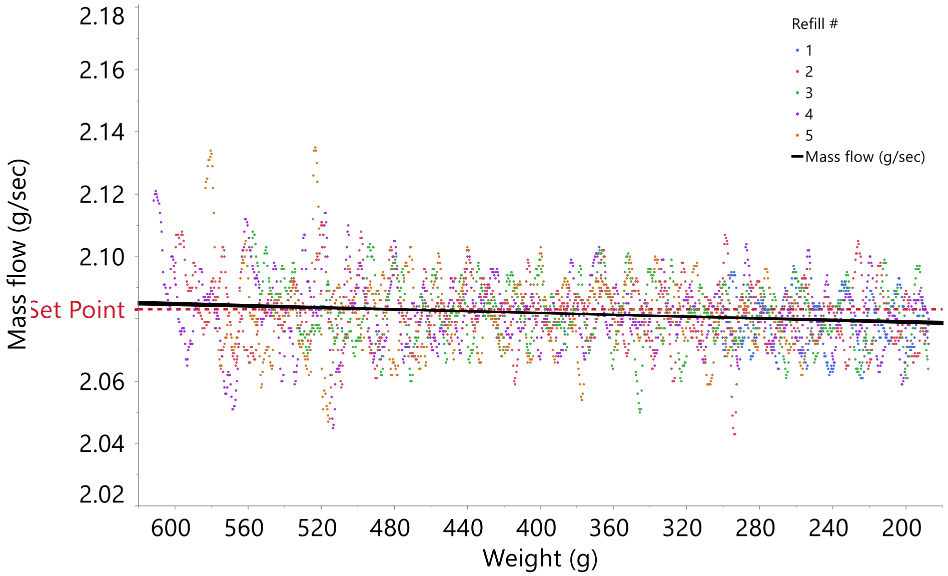

Figure 52 Mass flow as a function of the weight of material in the hopper for HPMC K100M DC experimental runs at the medium feed rate of 2.083 g/sec. Color indicates the refill number and the solid black line is the linear fit.

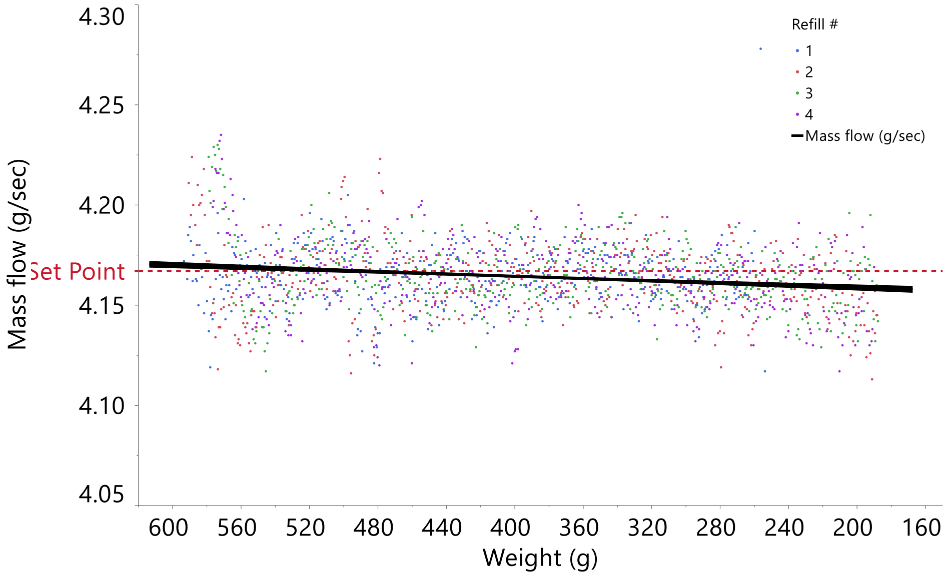

Figure 53 Mass flow as a function of the weight of material in the hopper for HPMC K100M DC experimental runs at the high feed rate of 4.167 g/sec. Color indicates the refill number and the solid black line is the linear fit.

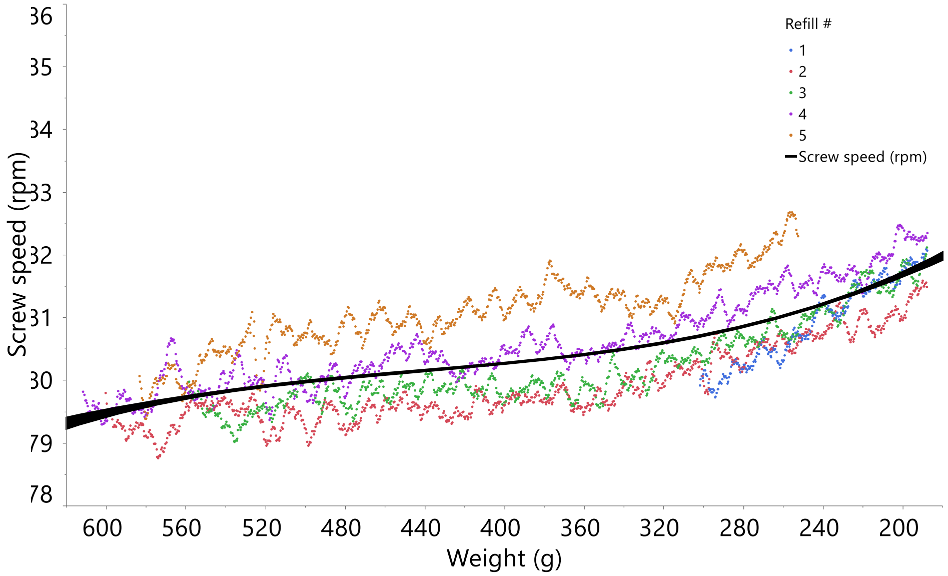

Figure 54 Feeder screw speed as a function of the weight of material in the hopper for HPMC K100M DC experimental runs at the high feed rate of 2.083 g/sec. Color indicates the refill number and the solid black line is the quadratic fit.

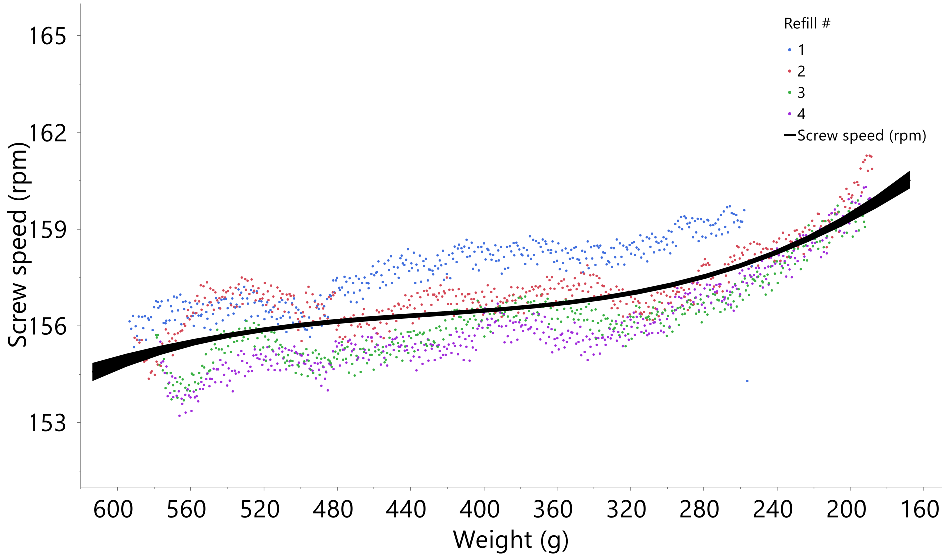

Figure 55 Feeder screw speed as a function of the weight of material in the hopper for HPMC K100M DC experimental runs at the high feed rate of 4.167 g/sec. Color indicates the refill number and the solid black line is the quadratic fit.

3.6 DEM LIW Feeder HPMC Simulation Results

The DEM LIW Feeder model was run using the particle parameters shown in **Table 21** which were based on the calibration tests and then adjusted through dimensional scaling after the shear modulus was reduced to decrease the computation time to a manageable amount.

Most of the simulations used the 2 mm Bow particles but there was one trial added with 1.2 mm Bow particles using the reduced shear modulus and the new scaled surface energy. This was done via constant X such that $X = \frac{\gamma}{(d*G)}$ and solving for the desired γ with the new particle size and shear modulus:

$$\gamma = X * d * G = (5 \times 10^{-7})\,(1.2 \times 10^{-3}\mathrm{m})\left(5 \times 10^{6}\ \mathrm{N}/_{\mathrm{m}^2}\right) = 3 \times 10^{-3}\ \mathrm{N}/_{\mathrm{m}}$$

Resulting in the scaled surface energy γ = 0.003 N/m for d = 1.2 mm Bow particles. It can also be determined through proportional relationships since the surface energy was already determined for 2 mm particles with the new shear modulus such that $\frac{d_{1.2}}{d_2} = \frac{\gamma_{1.2}}{\gamma_2}$ giving $\frac{1.2\ mm}{2\ mm} = \frac{\gamma_{1.2}}{0.005\ N/m}$ such that γ = 0.003 N/m for d = 1.2 mm Bow particles when using shear modulus G = 0.005 GPa.

The coulomb friction for the material is not known. When the friction is close to zero the material behaves as a fluid, but at larger values >0.2 the irregular shape of the Bow particles becomes more important than the friction. There are currently no reliable experimental approaches to accurately measuring the coefficient of friction for small nonspherical particles like HPMC and 0.5 has been used for similar materials (203, 204) There was also no effect on the calibration simulations when values ranging between 0.3, 0.5, 0.7 and 1 were simulated as surface energy has a larger effect. Other DEM evaluations have also shown negligible impact from varying CoR for similar pharmaceutical processes (214, 215).

Table 21 Generalized Particle Parameters for DEM for LIW model.

Parameter	Description	Value for simulated particles
G	Shear modulus	0.005 GPa*
ν	Poisson ratio	0.3
μ	Coulomb friction (static/dynamic)	0.5
CoR	Coefficient of restitution	0.1
g	Free fall acceleration	9.81 m/s^2
ρ	Material density	1.085 g/ml
f	Frequency for feeder screw operation	Variable rpm, based on target feed rate (either 4 g/s or 2 g/s) and the HPMC experimental curve for screw speed vs material weight in hopper
D	Process equipment characteristic sizes	Appropriate for equipment (e.g. hopper, screw, barrel, etc.)
d	Size	1.2 mm and 2 mm Bow particles, 1 mm Spheres
AR	Aspect Ratios	0.32, 0.39, 0.42, 0.48, 0.57, 0.74, 0.86
γ	Surface Energy	0.005 N/m for 2 mm Bow Particles** 0.003 N/m for 1.2 mm Bow Particles** 0.003 N/m for 1 mm Spheres**

* Reduced value from calibrations to allow for increased time step to reduce the simulation run time.

** Scaled from the value identified in the calibrations based on the reduced shear modulus.

The LIW simulation was initiated with the particles falling into the hopper with time for the particles to settle before the screws were started. The feeder screw speed used in the simulation was based on the observed screw speed for the HPMC K100M DC material related to the amount of material in the hopper and the target feed rate as described in **Section 3.5**. The initial 0.5 seconds were not included as that was the time required for the material to start filling the screws since they were initially empty. For the run at half speed it was required to remove the first 1 second as it took twice as long for the screw sections to fill at half speed. Also, the initial portion of the LIW feeder simulation still had particles beginning to be transferred out of the feeder before being fed at a constant rate. The average screw speeds and feed rates were determined for all of the simulations and experimental runs and shown in **Table 22** where all the line fittings to determine the feed rates had $R^2 \geq 0.992$ indicating a good fit. The line fits for the experimental HPMC across multiple refills were above $R^2 \geq 0.9995$.

The full hopper with 577 g of simulated 2 mm Bow particles was run at the high feed rate of 4 g/sec and compared to 1 mm spheres. The Bow particles were run for 2.9 seconds while the spheres were run for 7.4 seconds (faster simulation due to the ease of modeling with spheres). As expected, the spherical particles were poor representations for the elongated HPMC materials and resulted in significantly higher feed rate that was 63% faster compared to the experimental results as shown in **Table 22** and **Figure 56**. The 2 mm Bow particles were closer to the actual HPMC material, but had a feed rate 15% slower than HPMC K100M DC. **Figure 60** and **Figure 61** show a snapshot of the DEM simulations.

Instead of simulating the entire hopper emptying event there were multiple simulations performed using different amounts of material in the hopper of 360 g and 220 g to confirm the model at different hopper fill amounts with the 2 mm Bow particles. These resulted in a feed rates that were 15% and 11% slower respectively, as shown in **Figure 57** and **Figure 58** and in **Table 22**. These simulations were run for 3.5 seconds for the 360 g fill and 4 seconds for the 220 g fill and are shown in **Figure 62** and **Figure 63**.

The lower feed rates indicate that there may be some boundary affects manifesting with the larger 2 mm particles relative to the LIW feeder equipment since the screw pitch was 10 mm. To evaluate this possibility, the 1.2 mm particles were run with the lower 220 g hopper fill despite the simulation taking about 7 times longer due to the increased number of particles and contacts and slightly smaller time step that was required to resolve the collisions. This resulted in a feed rate that was 10% faster than the experimental rate, confirming the expectations around the boundary effect for 2 mm particles causing a reduced feed rate. Results for this tests are also included in **Figure 58** and **Figure 64**. A similar result was observed for spherical particles where a 20% lower simulated feed rate was determined for larger spheres because they had a lower probability to fall inside the screw pitch cavity, resulting in lower volumes of material being fed (210).

The final LIW feeder simulation was run at a medium speed (target feed rate 2 g/sec) with the medium hopper fill of 360 g to see if the simulations hold for significantly different screw speeds. The simulation was run for 6.2 seconds and had a very accurate feed rate that was 0.4% slower than the experimental results as shown in **Figure 59**. Since the feed rate for the medium screw speed was very close to target it further demonstrates the boundary effects seen for 2 mm bow particles at high speed as they were not present at medium speed. This is likely due to the ability for the particles to undergo rearrangement and better packing at medium speed and not at high speed.

Table 22 DEM simulation results for the LIW feeder.

Particle Shape	Hopper Fill Weight (g)	Simulated Time (sec)	Mean Screw Speed (rpm) ± (St dev)	Feed Rate (g/s) ± (St dev)	R^2 for Feed Rate (%)	Offset from Experimental Feed Rate
HPMC K100M DC*	at 576.55	-	155.7 ± 0.7	4.168 ± 0.003	0.9998	-
Bow 2 mm	576.55	2.9	155.59 ± 0.03	3.54 ± 0.01	0.9991	-15.1%
Spherical 1 mm	576.55	7.4	155.90 ± 0.02	6.774 ± 0.006	0.9997	+62.5%
HPMC K100M DC*	at 360	-	157.0 ± 0.9	4.167 ± 0.003	0.9998	-
Bow 2 mm	360	3.5	157.10 ± 0.01	3.56 ± 0.03	0.9929	-14.6%
HPMC K100M DC*	at 220	-	159.7 ± 0.4	4.158 ± 0.008	0.9995	-
Bow 2 mm	220	4	159.8 ± 0.1	3.71 ± 0.01	0.9991	-10.8%
Bow 1.2 mm	220	2.9	159.8 ± 0.1	4.59 ± 0.01	0.9995	+10.4%
HPMC K100M DC*	at 360	-	80.4 ± 0.6	2.083 ± 0.001	0.9998	-
Bow 2 mm	360	6.2	79.996 ± 0.008	2.092 ± 0.05	0.9987	-0.4%

*multiple refills over a 20 sec time frame

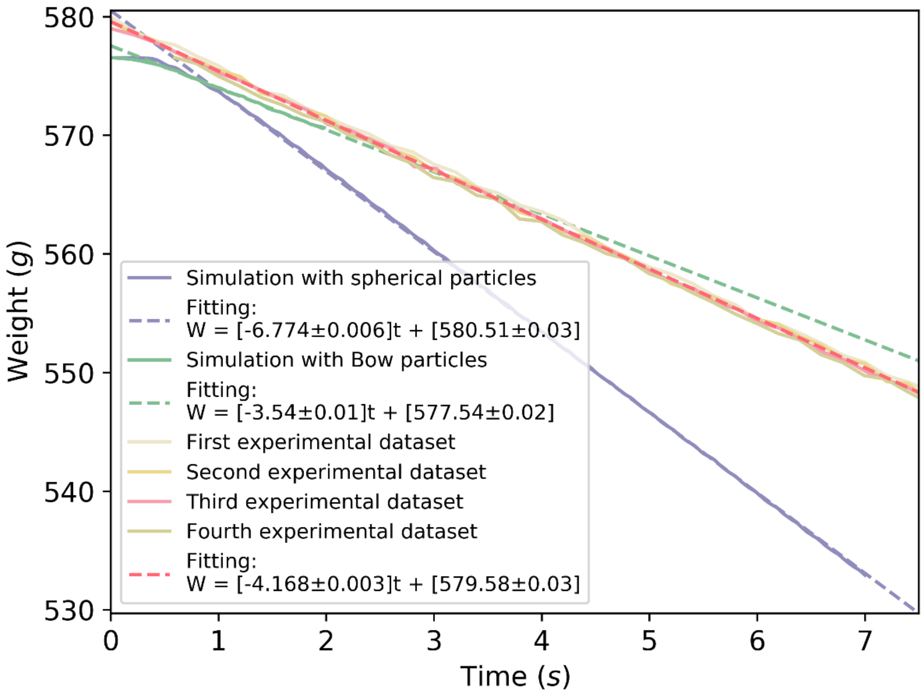

Figure 56 Simulation of 577 g hopper fill using Bow and Spherical particles.

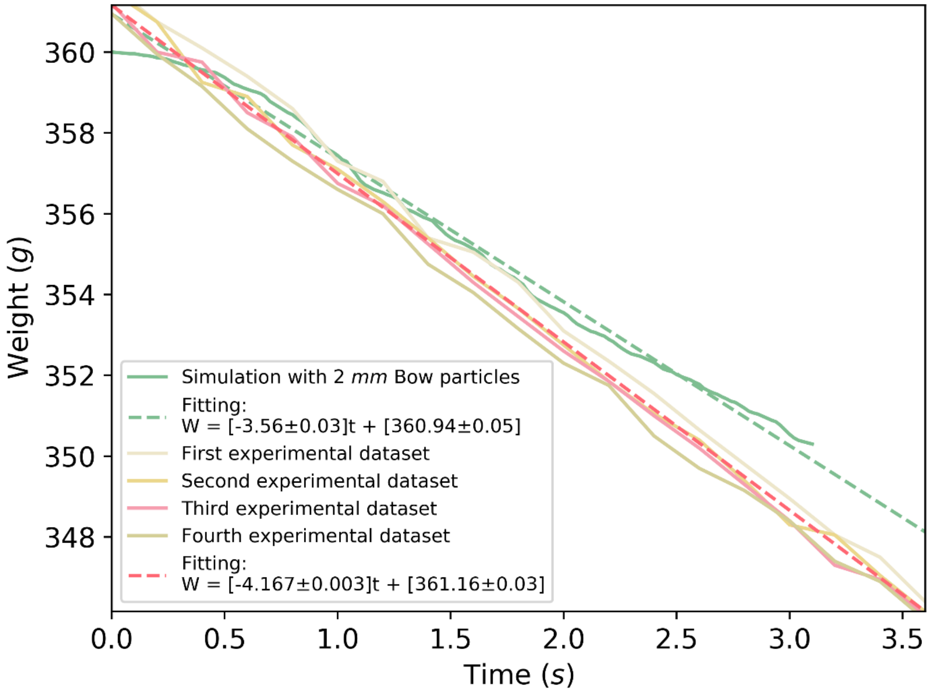

Figure 57 Simulation of 360 g hopper fill using 2 mm Bow particles.

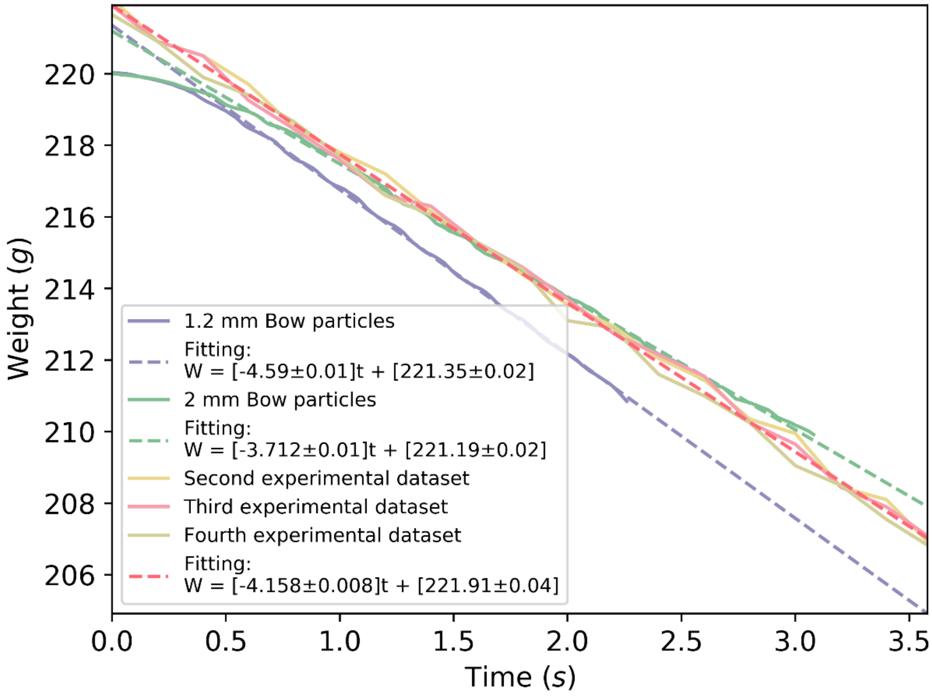

Figure 58 Simulation of 220 g hopper fill using Bow particles with EQPC = 2 mm and 1.2mm.

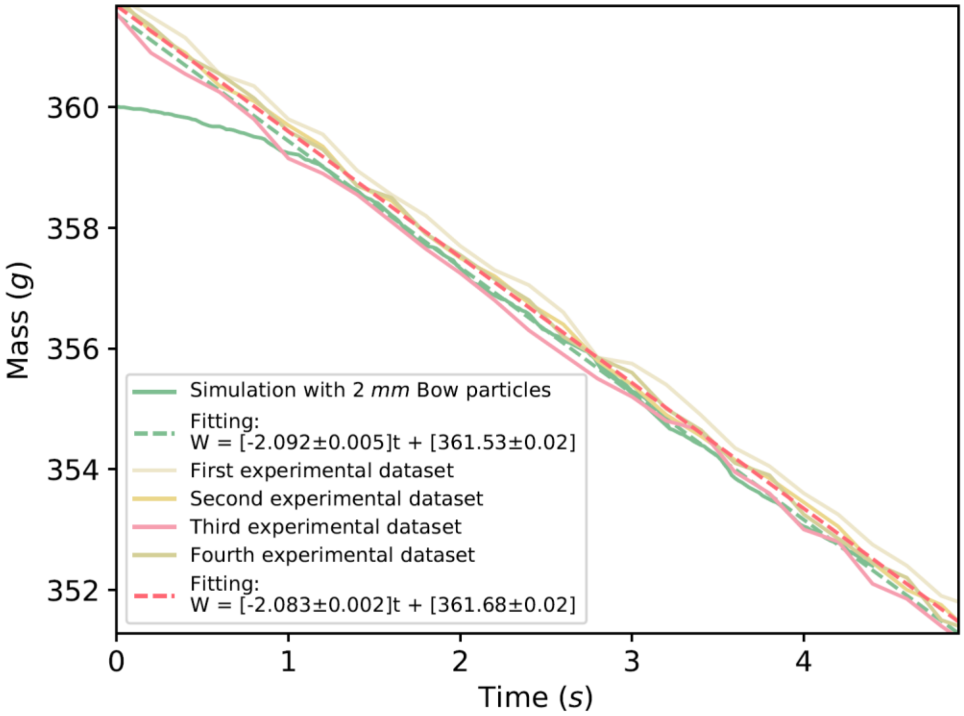

Figure 59 Simulation of 360 g hopper fill using 2 mm Bow particles for the medium feed rate.

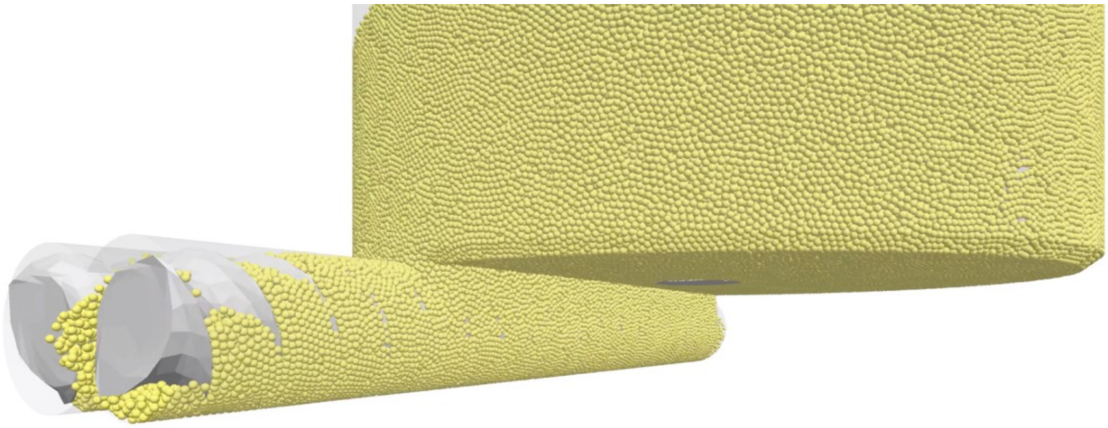

Figure 60 DEM simulation of LIW feeder for 1 mm Spherical particles with 577 g hopper fill.

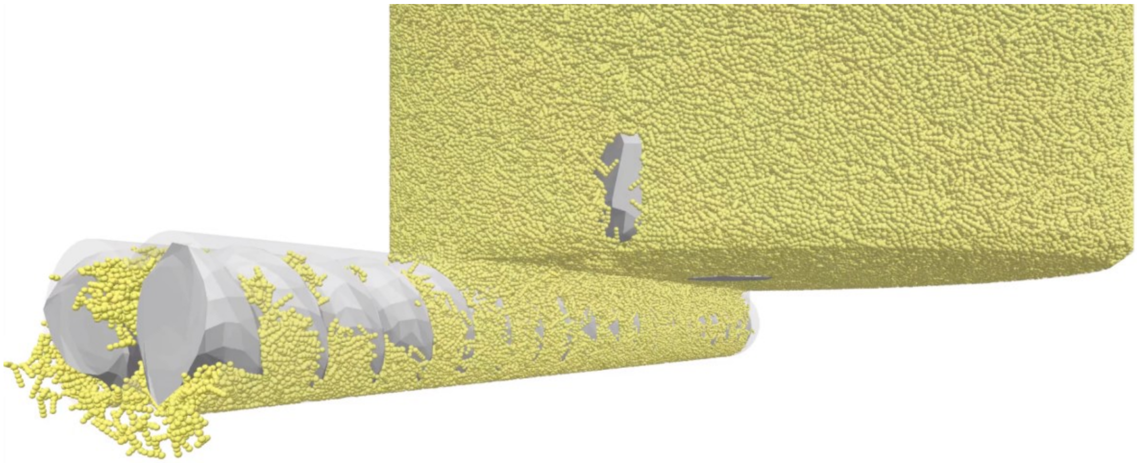

Figure 61 DEM simulation of LIW feeder for 2 mm Bow particles with 577 g hopper fill.

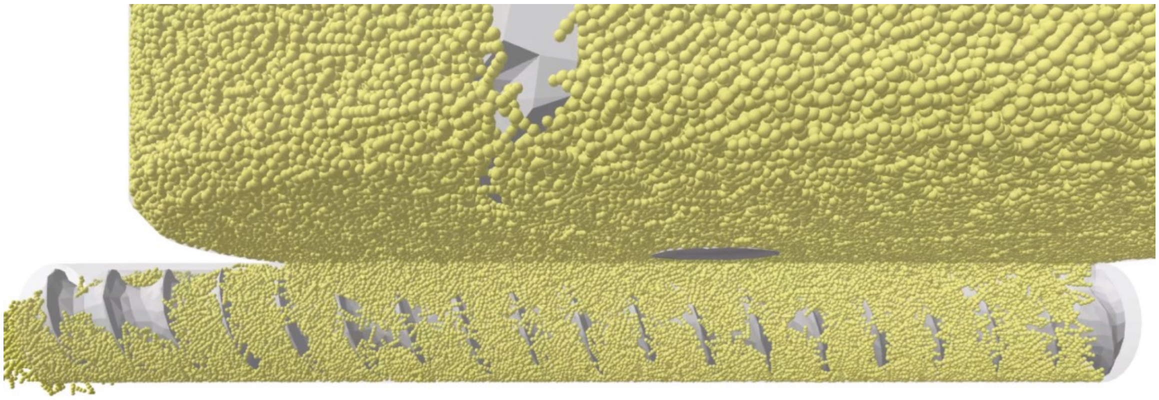

Figure 62 DEM simulation of LIW feeder for 2 mm Bow particles with 360 g hopper fill.

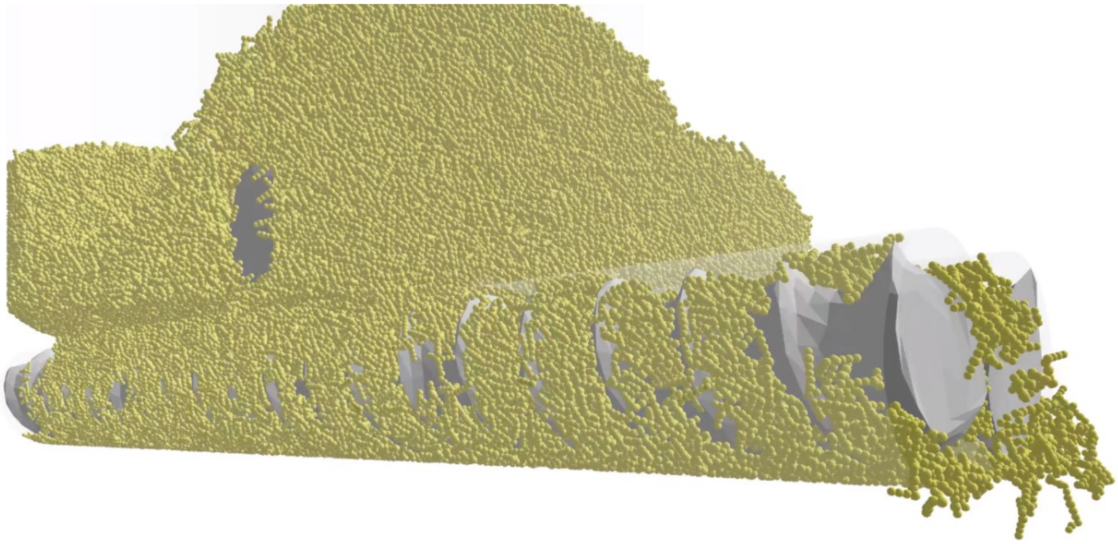

Figure 63 DEM simulation of LIW feeder for 2 mm Bow particles with 220 g hopper fill.

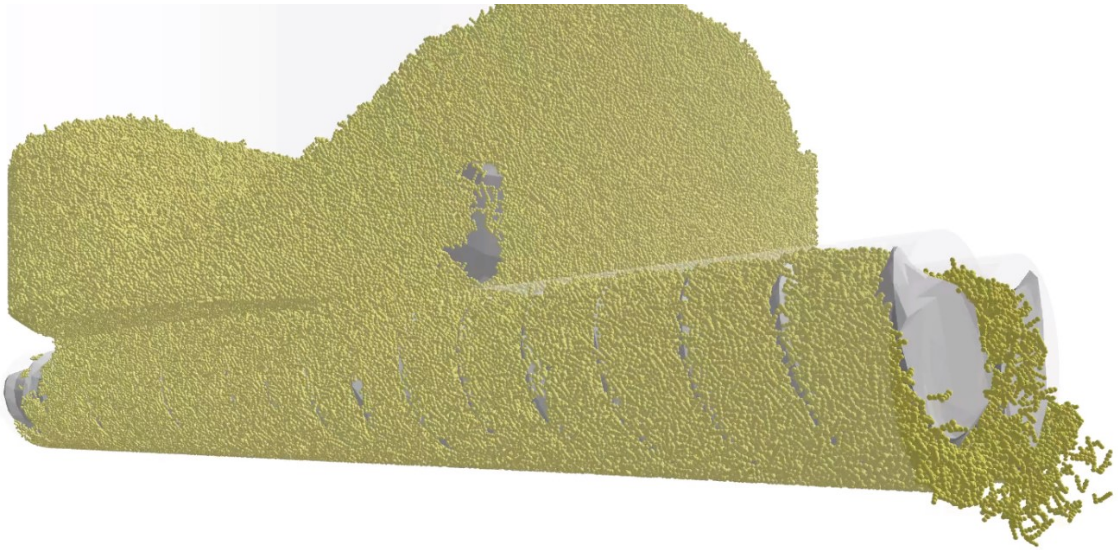

Figure 64 DEM simulation of LIW feeder for 1.2 mm Bow particles with 220 g hopper fill.

4 CONCLUSIONS

The use of overlapping multi-spheres to get representative complex Bow shaped particles with similar aspect ratios to the HPMC was successful in approximating the loss-in-weight feeding process for elongated HPMC particles. Spherical particles which are typically utilized for DEM simulations overestimated the feed rate by 63% demonstrating the importance of using a sufficiently representative shape for the DEM simulations. The simulations were successful across three different hopper fill ranges with the 2 mm Bow particles under predicting the actual feed rates for the high feed rate (ranging from -11% to -15% of experimental) with the reduced feed rates attributed to boundary effects due to the size of the particles, the volume of the screw pitch and the speed that the feeder was running. The slower rate was due to boundary interactions since the 2 mm EQPC particles (some of which were over 4 mm in length) were close to the 10 mm screw pitch even though a similar DEM simulation indicated the boundary effects were acceptable at a similar number of particles per screw section and the reduced rate did not occur until bigger particles were used, but that study was also performed using spheres (210). When the smaller 1.2 mm particles were simulated it over predicted the feed rate by 10% confirming the boundary effects and more accurately reproducing the experimental results.

The predicted feed rate was very close (0.4% slower than experimental) for the simulation with 2 mm Bow particles at the medium feed rate. At this slower speed the particles had twice as much time for particle rearrangement and filling of the screw sections compared to the higher speed further confirming the boundary effects from the particle size seen at high speed for 2 mm Bow particles.

It was also confirmed that the process could be characterized by running short simulations (long enough to derive a constant rate) at different hopper fill amounts rather than simulating the entire hopper emptying process.

The process of simulating the characterization tests was successful for determining the influence of shape, size, friction, cohesion, and density on DEM particle behavior and accurately simulated the GEA LIW feeder mass flow rate within 15% of experimental feed rates and even closer at slower speeds. This approach to material calibration is preferred over the system specific calibration approach which may only be valid in the system and in the ranges used for the calibration and may not represent the material in a different system (blending, flow through pipes, compaction, etc.) or outside of the parameters used. Individually calibrated and independently validated particle parameters should be the same for most system configurations once the important parameters are established.

SEM images and aspect ratios from image analysis were used to determine the DEM particle shapes which were then constructed from overlapped spheres. The HPMC true density and bulk density measurements were used to determine DEM particle apparent density. Angle of repose was used to estimate cohesion and determine the surface energy. A nominal value of coulomb friction was assumed since particle geometry and cohesion had the most influence on the process. Finally the rotating drum flow test was used to independently validate the DEM particle calibrations. While the calibration was performed using 1.2 mm particles, the surface energy was subsequently scaled using dimensional analysis to account for a necessary change increase in particle size to 2 mm and a reduction in the shear modulus. These changes were necessary to reduce the LIW feeder simulation run times to a more manageable 11-18 days each by reducing the number of particles (increased size) and allowing for an increased computation time step (reduced shear modulus).

Overall, this study has demonstrated that it is feasible to independently calibrate and model the LIW feeding process as the first step in a continuous manufacturing process even when challenging elongated particles shapes like HPMC are required and the simulation was able to predict feed rates within 15% of experimental results.

The relatively small difference between simulated and measured mass flows indicates that additional work is needed to examine calibration methodology to further improve simulation accuracy. This is especially important when combining multiple LIW feeders into an integrated continuous process as the mass flow results directly impact the downstream processes such as blending and compression. Additional DEM modeling may allow for the mass flows to be analytically determined requiring less computational burden to get meaningful results once established.

If the other process steps in the continuous manufacturing train were also modeled via DEM it would be possible to link the simulations of the various process modules to follow downstream impacts and gain overall process and system understanding. Many of these processes have already been shown as feasible via DEM but equipment specific to the continuous processing train would be required. Since GEA has standardized the equipment for continuous direct compression with the CDC-50 it is ideal for a combined implementation of DEM processes. These combined DEM models could then be used to evaluate process impacts for both material and process changes reducing the physical experimentation requirements.

APPENDICES

Additional SEM images at resolutions not included in **Chapter 1**. Magnifications 50x, 250x, and 1000x included. Material and magnification indicated on SEM images at the bottom. The images are grouped together in the following pages with each HPMC grade on a page with the three magnifications for that material

HPMC K100M CR

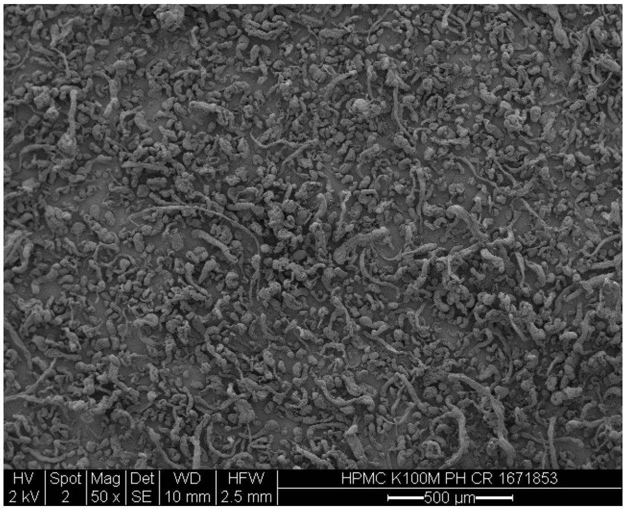

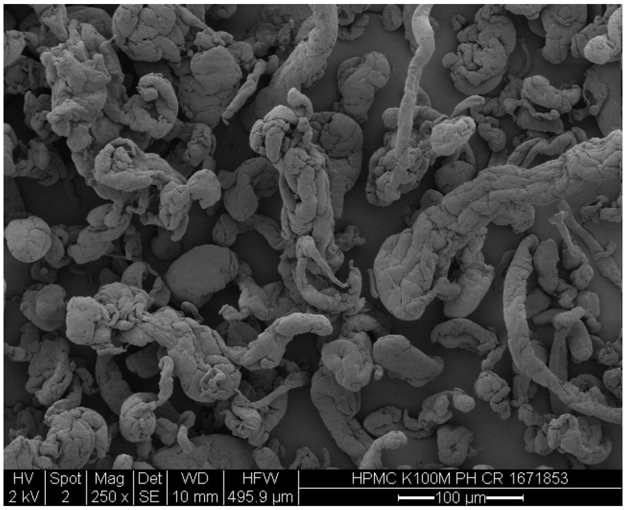

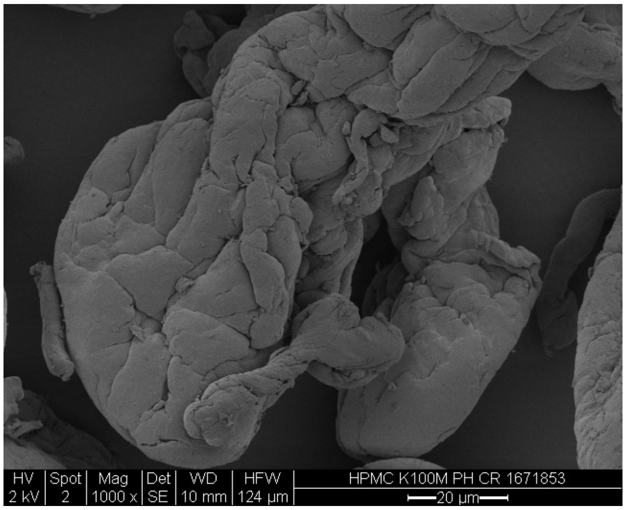

HPMC K100M DC

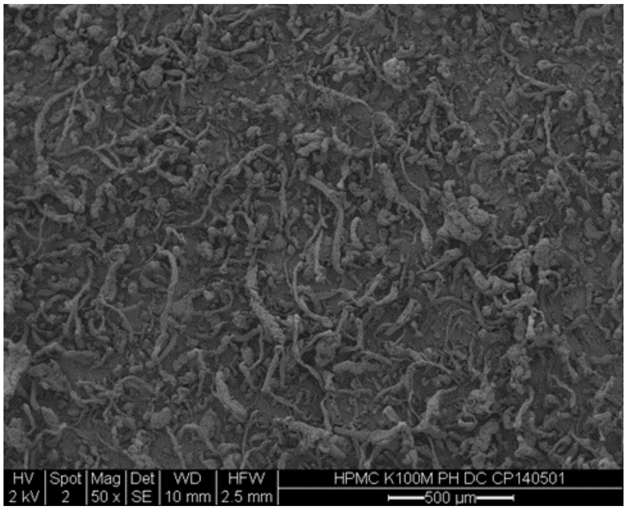

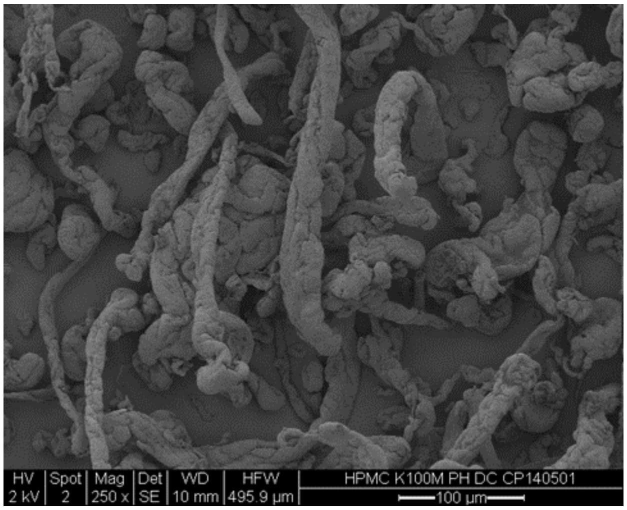

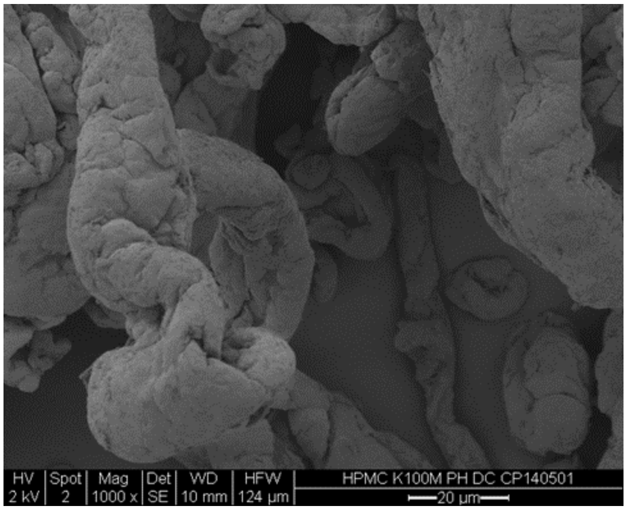

HPMC K15M CR

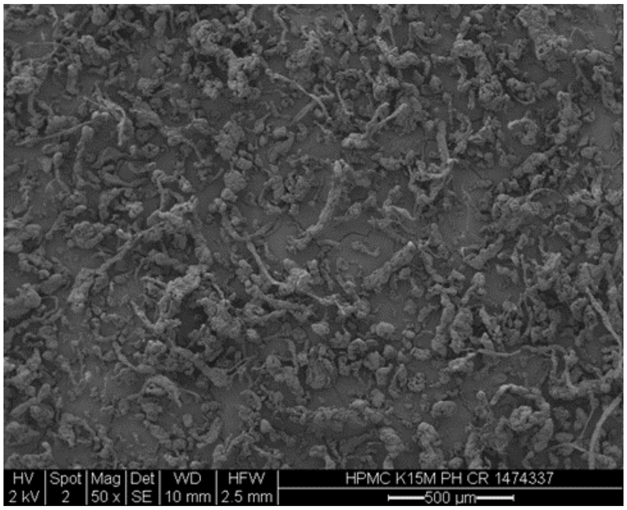
HV 2 kV
Spot 2
Mag 50 x
Det SE
WD 10 mm
HFW 2.5 mm
HPMC K15M PH CR 1474337
500 µm

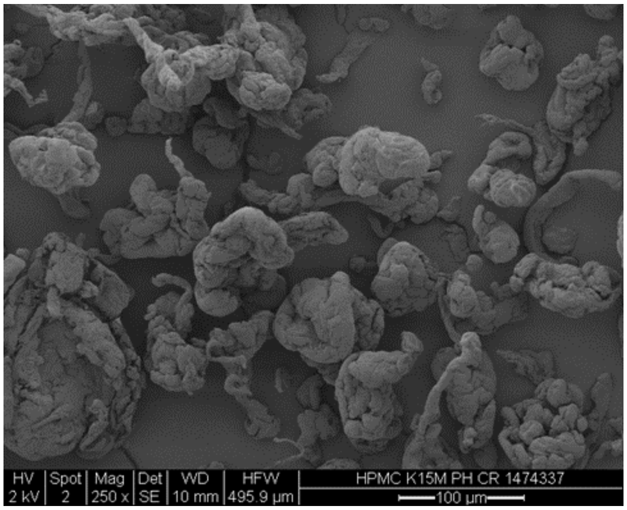
HV 2 kV
Spot 2
Mag 250 x
Det SE
WD 10 mm
HFW 495.9 µm
HPMC K15M PH CR 1474337
100 µm

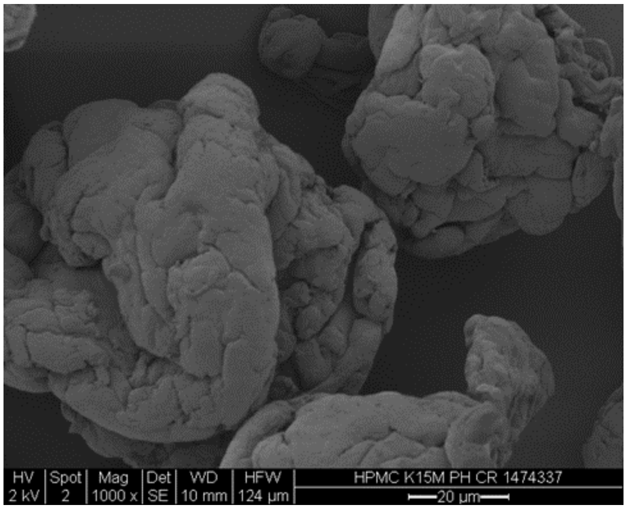
HV 2 kV
Spot 2
Mag 1000 x
Det SE
WD 10 mm
HFW 124 µm
HPMC K15M PH CR 1474337
20 µm

HPMC K15M DC

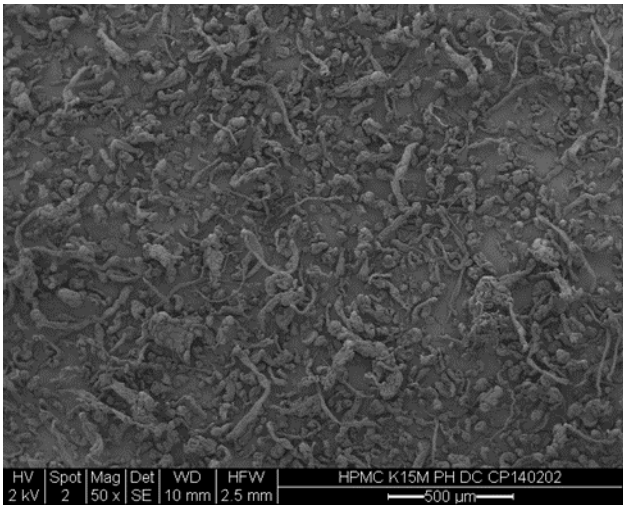
HV | Spot | Mag | Det | WD | HFW
2 kV | 2 | 50 x | SE | 10 mm | 2.5 mm
HPMC K15M PH DC CP140202
500 µm

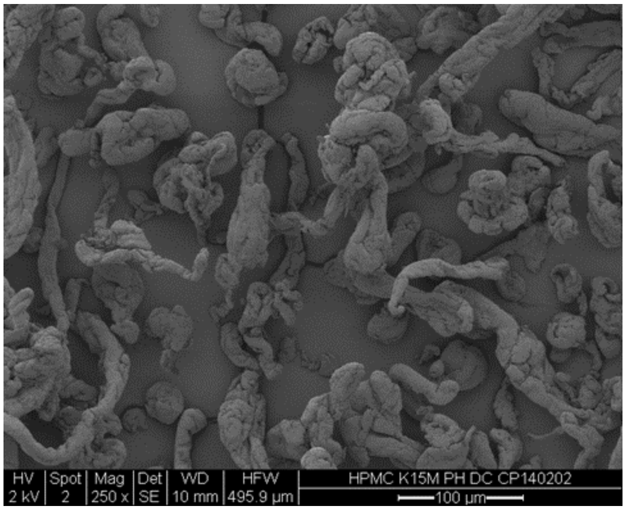
HV | Spot | Mag | Det | WD | HFW
2 kV | 2 | 250 x | SE | 10 mm | 495.9 µm
HPMC K15M PH DC CP140202
100 µm

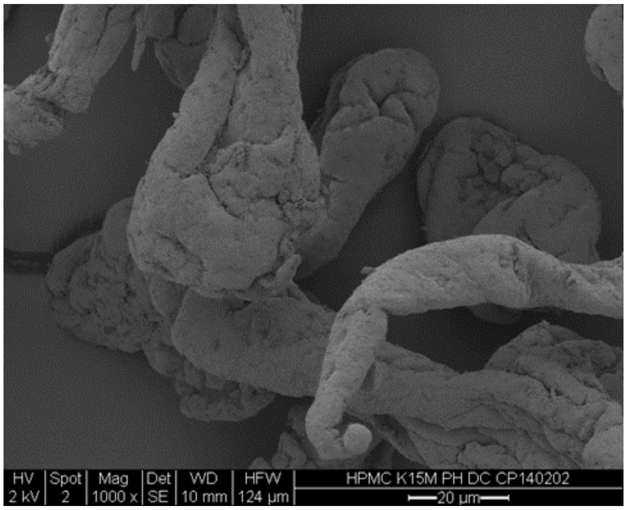
HV | Spot | Mag | Det | WD | HFW
2 kV | 2 | 1000 x | SE | 10 mm | 124 µm
HPMC K15M PH DC CP140202
20 µm

HPMC K4M CR

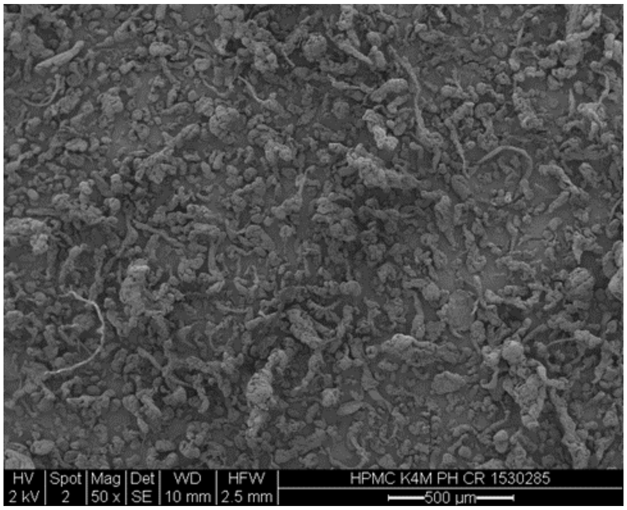
HV | Spot | Mag | Det | WD | HFW
2 kV | 2 | 50 x | SE | 10 mm | 2.5 mm
HPMC K4M PH CR 1530285
500 µm

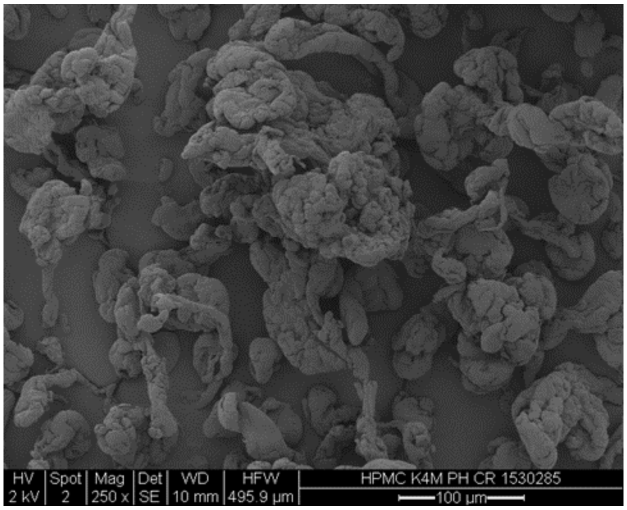
HV | Spot | Mag | Det | WD | HFW
2 kV | 2 | 250 x | SE | 10 mm | 495.9 µm
HPMC K4M PH CR 1530285
100 µm

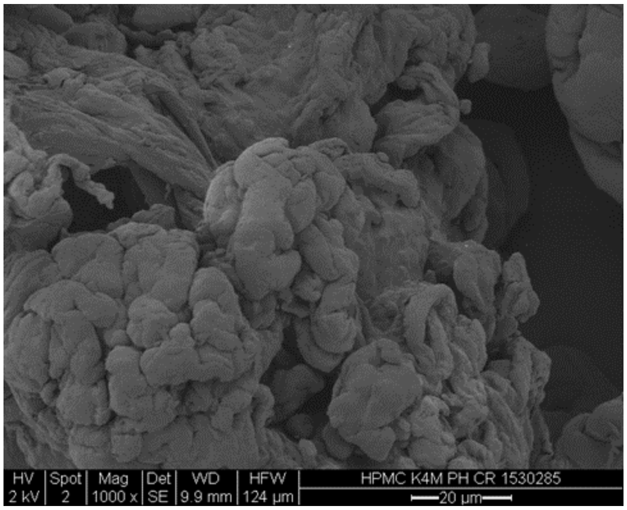
HV | Spot | Mag | Det | WD | HFW
2 kV | 2 | 1000 x | SE | 9.9 mm | 124 µm
HPMC K4M PH CR 1530285
20 µm

HPMC K4M DC

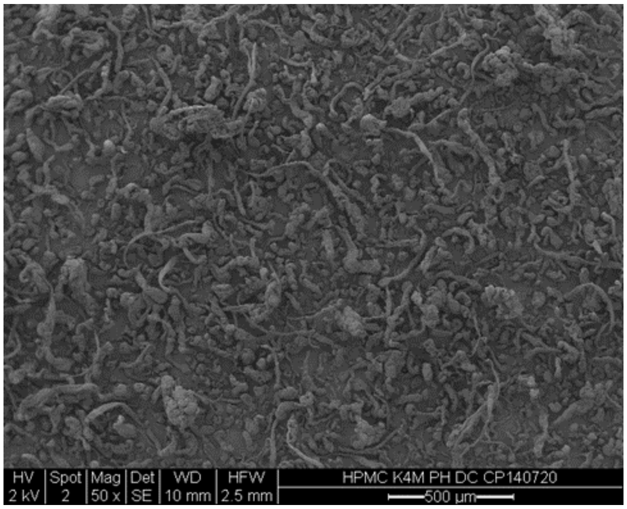
HV 2 kV
Spot 2
Mag 50 x
Det SE
WD 10 mm
HFW 2.5 mm
HPMC K4M PH DC CP140720
500 µm

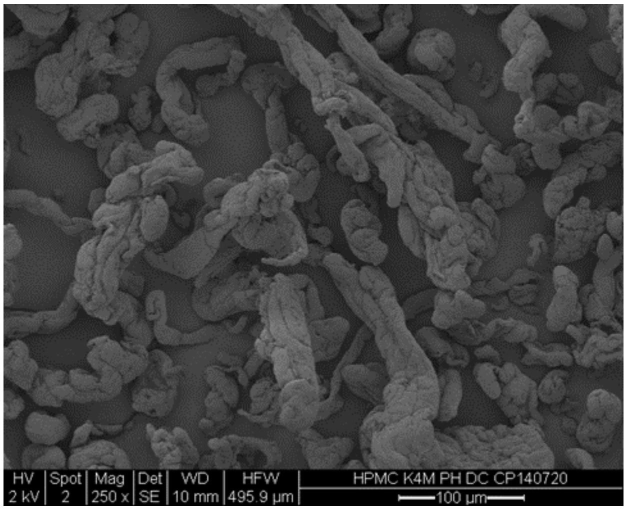
HV 2 kV
Spot 2
Mag 250 x
Det SE
WD 10 mm
HFW 495.9 µm
HPMC K4M PH DC CP140720
100 µm

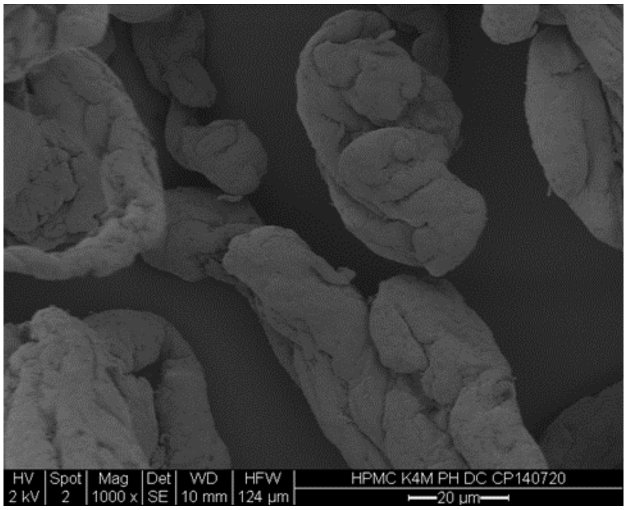
HV 2 kV
Spot 2
Mag 1000 x
Det SE
WD 10 mm
HFW 124 µm
HPMC K4M PH DC CP140720
20 µm

REFERENCES

All references are included in the text.

ACKNOWLEDGMENT OF PREVIOUS PUBLICATIONS

The introduction included some aspects from the following book chapter:

Peter Timmins and Carl Allenspach. "Particle Properties: Impact on the Processing and Performance of Oral Extended-Release Hydrophilic Matrix Tablets." In Particles and Nanoparticles in Pharmaceutical Products, pp. 347-372. Springer, Cham, 2018.

Chapter 1 was composed mainly from the publication, except the tablet compaction work in sections 2.3, 3.6 and 3.7 of Chapter 1.

Carl Allenspach, Peter Timmins, Shasad Sharif, and Tamara Minko. "Characterization of a novel hydroxypropyl methylcellulose (HPMC) direct compression grade excipient for pharmaceutical tablets." International Journal of Pharmaceutics (2020): 119343.

Chapter 2 was composed from the publication which has been submitted:

Carl Allenspach, Peter Timmins, Geoffroy Lumay, James Holman, Tamara Minko. "Loss in Weight Feeding, Powder Flow and Electrostatic Evaluation for Direct Compression Hydroxypropyl methylcellulose (HPMC) to Support Continuous Manufacturing." International Journal of Pharmaceutics (2020), Submitted.

Chapter 3 is in preparation for publication under:

Carl Allenspach, Peter Timmins, Anton Kulchitsky, Jerome Johnson, Dmytro Cherepakha, Tamara Minko. "DEM Modeling of a Loss in Weight Feeder with Elongated Particles to Support Continuous Manufacturing" International Journal of Pharmaceutics, In preparation.

BIBLIOGRAPHY

1. Timmins P, Pygall SR, Melia CD. Hydrophilic matrix tablets for oral controlled release: Springer; 2014.

2. Timmins P, Desai D, Chen W, Wray P, Brown J, Hanley S. Advances in mechanistic understanding of release rate control mechanisms of extended-release hydrophilic matrix tablets. Therapeutic delivery. 2016;7(8):553-72.

3. Alderman D. A review of cellulose ethers in hydrophilic matrices for oral controlled-release dosage forms. Int J Pharm Tech Prod Mfr. 1984;5(3):1-9.

4. Li CL, Martini LG, Ford JL, Roberts M. The use of hypromellose in oral drug delivery. J Pharm Pharmacol. 2005;57(5):533-46. doi: 10.1211/0022357055957.

5. Brown J, Chien C, Timmins P, Dennis A, Doll W, Sandefer E, et al. Compartmental absorption modeling and site of absorption studies to determine feasibility of an extended-release formulation of an HIV-1 attachment inhibitor phosphate ester prodrug. Journal of pharmaceutical sciences. 2013;102(6):1742-51.

6. Timmins P, Brown J, Meanwell NA, Hanna GJ, Zhu L, Kadow JF. Enabled clinical use of an HIV-1 attachment inhibitor through drug delivery. Drug Discovery Today. 2014;19(9):1288-93.

7. Good DJ, Hartley R, Mathias N, Crison J, Tirucherai G, Timmins P, et al. Mitigation of adverse clinical events of a narrow target therapeutic index compound through modified release formulation design: an in vitro, in vivo, in silico, and clinical pharmacokinetic analysis. Molecular pharmaceutics. 2015;12(12):4434-44.

8. Christenson GL. Sustained release tablet. In: Dale LB, editor.: US Patents; 1962.

9. Higuchi T. Mechanism of sustained-action medication. Theoretical analysis of rate of release of solid drugs dispersed in solid matrices. Journal of pharmaceutical sciences. 1963;52(12):1145-9.

10. Huber H, Dale L, Christenson G. Utilization of hydrophilic gums for the control of drug release from tablet formulations I. Disintegration and dissolution behavior. Journal of Pharmaceutical Sciences. 1966;55(9):974-6.

11. Lapidus H, Lordi NG. Some factors affecting the release of a water-soluble drug from a compressed hydrophilic matrix. Journal of pharmaceutical sciences. 1966;55(8):840-3.

12. Timmins P, Allenspach C. Particle Properties: Impact on the Processing and Performance of Oral Extended-Release Hydrophilic Matrix Tablets. Particles and Nanoparticles in Pharmaceutical Products: Springer; 2018. p. 347-72.

13. Nagy ZK, El Hagrasy A, Litster J. Continuous Pharmaceutical Processing. Springer; 2020.

14. Kleinebudde P, Khinast J, Rantanen J. Continuous manufacturing of pharmaceuticals: John Wiley & Sons; 2017.

15. Muzzio F, Oka S. How to Design and Implement Powder-to-Tablet Continuous Manufacturing Systems: Elsevier Science; 2021.

16. National Academies of Sciences EM, Studies DEL, Technology BCS, Alper J. Continuous Manufacturing for the Modernization of Pharmaceutical Production: Proceedings of a Workshop: National Academies Press; 2019.

17. Food U, Administration D. Quality considerations for continuous manufacturing–Guidance for industry–draft guidance. 2019.

18. Food U, Administration D. Advancement of emerging technology applications for pharmaceutical innovation and modernization: guidance for industry. 2017.

19. Lee SL, O'Connor TF, Yang X, Cruz CN, Chatterjee S, Madurawe RD, et al. Modernizing Pharmaceutical Manufacturing: from Batch to Continuous Production. Journal of Pharmaceutical Innovation. 2015;10(3):191-9. doi: 10.1007/s12247-015-9215-8.

20. Vargas JM, Nielsen S, Cárdenas V, Gonzalez A, Aymat EY, Almodovar E, et al. Process analytical technology in continuous manufacturing of a commercial pharmaceutical product. International journal of pharmaceutics. 2018;538(1-2):167-78.

21. Chatterjee S, editor. FDA perspective on continuous manufacturing. IFPAC Annual Meeting, Baltimore, MD; 2012.

22. Ierapetritou M, Muzzio F, Reklaitis G. Perspectives on the continuous manufacturing of powder-based pharmaceutical processes. AIChE Journal. 2016;62(6):1846-62.

23. Yeom SB, Ha E-S, Kim M-S, Jeong SH, Hwang S-J, Choi DH. Application of the discrete element method for manufacturing process simulation in the pharmaceutical industry. Pharmaceutics. 2019;11(8):414.

24. Wassgren C, Curtis JS. The application of computational modeling to pharmaceutical materials science. MRS bulletin. 2006;31(11):900-4.

25. Pandey P, Bharadwaj R. Predictive Modeling of Pharmaceutical Unit Operations: Woodhead Publishing; 2016.

26. Rogers AJ, Hashemi A, Ierapetritou MG. Modeling of particulate processes for the continuous manufacture of solid-based pharmaceutical dosage forms. Processes. 2013;1(2):67-127.

27. Cundall PA, Strack OD. A discrete numerical model for granular assemblies. geotechnique. 1979;29(1):47-65.

28. Jebahi M, André D, Terreros I, Iordanoff I. Discrete element method to model 3D continuous materials: John Wiley & Sons; 2015.

29. Munjiza AA. The combined finite-discrete element method: John Wiley & Sons; 2004.

30. Sarhosis V, Bagi K, Lemos JV, Milani G. Computational modeling of masonry structures using the discrete element method: IGI Global; 2016.

31. Jing L, Stephansson O. Fundamentals of discrete element methods for rock engineering: theory and applications: Elsevier; 2007.

32. Radjaï F, Dubois F. Discrete-element modeling of granular materials2011.

33. Matuttis H-G, Chen J. Understanding the discrete element method: simulation of non-spherical particles for granular and multi-body systems: John Wiley & Sons; 2014.

34. Gelnar D, Zegzulka J. Discrete Element Method in the Design of Transport Systems: Verification and Validation of 3D Models: Springer; 2019.

35. Radeke CA, Glasser BJ, Khinast JG. Large-scale powder mixer simulations using massively parallel GPUarchitectures. Chemical Engineering Science. 2010;65(24):6435-42. doi: https://doi.org/10.1016/j.ces.2010.09.035.

36. Orefice L, Khinast JG. A novel framework for a rational, fully-automatised calibration routine for DEM models of cohesive powders. Powder Technology. 2020;361:687-703.

37. Amidon GE, Anderson BD, Balthasar JP, Bergstrom CA, Huang S-M, Kasting G, et al. Fifty-eight years and counting: high-impact publishing in computational pharmaceutical sciences and mechanism-based modeling. Journal of pharmaceutical sciences. 2019;108(1):2-7.

38. Kremer DM, Hancock BC. Process Simulation in the Pharmaceutical Industry: A Review of Some Basic Physical Models. Journal of Pharmaceutical Sciences. 2006;95(3):517-29. doi: https://doi.org/10.1002/jps.20583.

39. Lu G, Third J, Müller C. Discrete element models for non-spherical particle systems: From theoretical developments to applications. Chemical Engineering Science. 2015;127:425-65.

40. Simonaho S-P, Ketolainen J, Ervasti T, Toiviainen M, Korhonen O. Continuous manufacturing of tablets with PROMIS-line—Introduction and case studies from continuous feeding, blending and tableting. European Journal of Pharmaceutical Sciences. 2016;90:38-46.

41. Pernenkil L, Cooney CL. A review on the continuous blending of powders. Chemical Engineering Science. 2006;61(2):720-42.

42. Byrn S, Futran M, Thomas H, Jayjock E, Maron N, Meyer RF, et al. Achieving continuous manufacturing for final dosage formation: challenges and how to meet them. May 20–21, 2014 continuous manufacturing symposium. Journal of pharmaceutical sciences. 2015;104(3):792-802.

43. Cramer MP, Saks SR. Translating safety, efficacy and compliance into economic value for controlled release dosage forms. Pharmacoeconomics. 1994;5(6):482-504.

44. Rogers T, Hewlett K, Theuerkauf J, Balwinski K. Assessing how the physical properties and enhanced powder flow of HPMC affect process control during direct compression of matrix tablets. Tablets Capsules. 2013;(October):14-22.

45. Maderuelo C, Zarzuelo A, Lanao JM. Critical factors in the release of drugs from sustained release hydrophilic matrices. J Control Release. 2011;154(1):2-19. doi: 10.1016/j.jconrel.2011.04.002.

46. Doelker E. Swelling Behavior of Water-Soluble Cellulose Derivatives. In: Brannon-Peppas L, Harland RS, editors. Studies in Polymer Science: Elsevier; 1990. p. 125-45.

47. Eyjolfsson R. Chapter Three - Slow-Release (SR) Tablets. In: Eyjolfsson R, editor. Design and Manufacture of Pharmaceutical Tablets. Boston: Academic Press; 2015. p. 43-50.

48. Kaur G, Grewal J, Jyoti K, Jain UK, Chandra R, Madan J. Chapter 15 - Oral controlled and sustained drug delivery systems: Concepts, advances, preclinical, and clinical status. In: Grumezescu AM, editor. Drug Targeting and Stimuli Sensitive Drug Delivery Systems: William Andrew Publishing; 2018. p. 567-626.

49. Pandey SP, Shukla T, Dhote VK, K. Mishra D, Maheshwari R, Tekade RK. Chapter 4 - Use of Polymers in Controlled Release of Active Agents. In: Tekade RK, editor. Basic Fundamentals of Drug Delivery: Academic Press; 2019. p. 113-72.

50. Wypych G. HPMC hydroxypropyl methylcellulose. In: Wypych G, editor. Handbook of Polymers (Second Edition): ChemTec Publishing; 2016. p. 166-7.

51. Hogan JE. Hydroxypropylmethylcellulose sustained release technology. Drug Development and Industrial Pharmacy. 1989;15(6-7):975-99. doi: 10.3109/03639048909043660.

52. Tiwari SB, Rajabi-Siahboomi AR. Modulation of drug release from hydrophilic matrices. 2008.

53. Tiwari G, Tiwari R, Sriwastawa B, Bhati L, Pandey S, Pandey P, et al. Drug delivery systems: An updated review. Int J Pharm Investig. 2012;2(1):2-11. doi: 10.4103/2230-973X.96920.

54. Lapidus H, Lordi NG. Drug release from compressed hydrophilic matrices. Journal of Pharmaceutical Sciences. 1968;57(8):1292-301. doi: 10.1002/jps.2600570803.

55. Herder J, Adolfsson Å, Larsson A. Initial studies of water granulation of eight grades of hypromellose (HPMC). International Journal of Pharmaceutics. 2006;313(1):57-65. doi: https://doi.org/10.1016/j.ijpharm.2006.01.024.

56. Nellore RV, Singh Rekhi G, Hussain AS, Tillman LG, Augsburger LL. Development of metoprolol tartrate extended-release matrix tablet formulations for regulatory policy consideration. Journal of Controlled Release. 1998;50(1):247-56. doi: https://doi.org/10.1016/S0168-3659(97)00141-7.

57. Teng Y, Qiu Z, Wen H. Systematical approach of formulation and process development using roller compaction. European Journal of Pharmaceutics and Biopharmaceutics. 2009;73(2):219-29. doi: https://doi.org/10.1016/j.ejpb.2009.04.008.

58. Ervasti T, Simonaho SP, Ketolainen J, Forsberg P, Fransson M, Wikstrom H, et al. Continuous manufacturing of extended release tablets via powder mixing and direct compression. Int J Pharm. 2015;495(1):290-301. doi: 10.1016/j.ijpharm.2015.08.077.

59. Burcham CL, Florence AJ, Johnson MD. Continuous Manufacturing in Pharmaceutical Process Development and Manufacturing. Annual Review of Chemical and Biomolecular Engineering. 2018;9(1):253-81. doi: 10.1146/annurev-chembioeng-060817-084355.

60. 6 - Drug delivery systems. In: Bruschi ML, editor. Strategies to Modify the Drug Release from Pharmaceutical Systems: Woodhead Publishing; 2015. p. 87-194.

61. Leuenberger H. New trends in the production of pharmaceutical granules: batch versus continuous processing. Eur J Pharm Biopharm. 2001;52(3):289-96.

62. Oka S, Sahay A, Meng W, Muzzio F. Diminished segregation in continuous powder mixing. Powder Technology. 2017;309:79-88. doi: https://doi.org/10.1016/j.powtec.2016.11.038.

63. Dow Chemical Company T. Using Dow Excipients for Controlled Release of Drugs in Hydrophilic Matrix Systems. U.S.A.: The Dow Chemical Company; 2006. p. 36.

64. Venables HJ, Wells JI. Powder sampling. Drug Dev Ind Pharm. 2002;28(2):107-17. doi: 10.1081/DDC-120002443.

65. Charlier R, Goossens W. Sampling a heterogeneous powder using a spinning riffler. Powder Technology. 1971;4(6):351-9.

66. Crosby NT, Patel I. General principles of good sampling practice: Royal Society of Chemistry; 1995.

67. United States Pharmacopeia. General Chapters: <616> BULK DENSITY AND TAPPED DENSITY OF POWDERS2018. p. 1.

68. Viana M, Jouannin P, Pontier C, Chulia D. About pycnometric density measurements. Talanta. 2002;57(3):583-93. doi: 10.1016/S0039-9140(02)00058-9.

69. Köhler U, List J, Witt W. Comparison of laser diffraction and image analysis under identical dispersing conditions. Partec, Nürnberg. 2007.

70. Yu W, Hancock BC. Evaluation of dynamic image analysis for characterizing pharmaceutical excipient particles. International journal of pharmaceutics. 2008;361(1):150-7.

71. McClellan AL, Harnsberger H. Cross-sectional areas of molecules adsorbed on solid surfaces. Journal of Colloid and Interface Science. 1967;23(4):577-99.

72. Abdullah E, Geldart D. The use of bulk density measurements as flowability indicators. Powder Technology. 1999;102(2):151-65.

73. Lavoie F, Cartilier L, Thibert R. New methods characterizing avalanche behavior to determine powder flow. Pharmaceutical research. 2002;19(6):887-93.

74. Freeman R. Measuring the flow properties of consolidated, conditioned and aerated powders — A comparative study using a powder rheometer and a rotational shear cell. Powder Technology. 2007;174(1):25-33. doi: http://dx.doi.org/10.1016/j.powtec.2006.10.016.

75. Bordawekar M. An investigation of the physico-mechanical properties of pharmaceutical compounds by compaction simulator and nano-indentation2012.

76. Ruegger CE. Advanced compaction research equipment: Compaction simulators. Pharmaceutical Powder Compaction Technology, Second Edition: CRC Press; 2016. p. 112-41.

77. Sinka I, Cocks A. Modelling die compaction in the pharmaceutical industry. Modelling of Powder Die Compaction: Springer; 2008. p. 223-42.

78. Tarlier N, Soulairol I, Bataille B, Baylac G, Ravel P, Nofrerias I, et al. Compaction behavior and deformation mechanism of directly compressible textured mannitol in a rotary tablet press simulator. International journal of pharmaceutics. 2015;495(1):410-9.

79. Hancock BC, Colvin JT, Mullarney MP, Zinchuk AV. The relative densities of pharmaceutical powders, blends, dry granulations, and immediate-release tablets. Pharmaceutical technology. 2003;27(4):64-.

80. Kushner IV J, Moore F. Scale-up model describing the impact of lubrication on tablet tensile strength. International journal of pharmaceutics. 2010;399(1-2):19-30.

81. Faqih AMN, Mehrotra A, Hammond SV, Muzzio FJ. Effect of moisture and magnesium stearate concentration on flow properties of cohesive granular materials. International journal of pharmaceutics. 2007;336(2):338-45.

82. Amidon GE, Houghton ME. The effect of moisture on the mechanical and powder flow properties of microcrystalline cellulose. Pharmaceutical research. 1995;12(6):923-9.

83. Sun CC. Mechanism of moisture induced variations in true density and compaction properties of microcrystalline cellulose. International journal of pharmaceutics. 2008;346(1-2):93-101.

84. Crouter A, Briens L. The effect of moisture on the flowability of pharmaceutical excipients. AAPS PharmSciTech. 2014;15(1):65-74. doi: 10.1208/s12249-013-0036-0.

85. Nokhodchi A. Effect of moisture on compaction and compression. Pharm Tech. 2005;6:46-66.

86. Shukla AJ, Price JC. Effect of moisture content on compression properties of directly compressible high beta-content anhydrous lactose. Drug development and industrial pharmacy. 1991;17(15):2067-81.

87. Sangekar S, Sarli M, Sheth P. Effect of moisture on physical characteristics of tablets prepared from direct compression excipients. Journal of Pharmaceutical Sciences. 1972;61(6):939-44.

88. Dawoodbhai S, Rhodes CT. The Effect of Moisture on Powder Flow and on Compaction and Physical Stability of Tablets. Drug development and industrial pharmacy. 2008;15(10):1577-600. doi: 10.3109/03639048909052504.

89. Liu LX, Marziano I, Bentham AC, Litster JD, E.T.White, Howes T. Effect of particle properties on the flowability of ibuprofen powders. International Journal of Pharmaceutics. 2008;362(1):109-17. doi: https://doi.org/10.1016/j.ijpharm.2008.06.023.

90. Jonat S, Hasenzahl S, Drechsler M, Albers P, Wagner KG, Schmidt PC. Investigation of compacted hydrophilic and hydrophobic colloidal silicon dioxides as glidants for pharmaceutical excipients. Powder Technology. 2004;141(1):31-43. doi: https://doi.org/10.1016/j.powtec.2004.01.020.

91. Fraser Steele D, Tobyn M, Edge S, Chen A, Staniforth JN. Physicochemical and Mechanical Evaluation of a Novel High Density Grade of Silicified Microcrystalline Cellulose. Drug Development and Industrial Pharmacy. 2004;30(1):103-9. doi: 10.1081/DDC-120027517.

92. Rojas J, Kumar V. Comparative evaluation of silicified microcrystalline cellulose II as a direct compression vehicle. International Journal of Pharmaceutics. 2011;416(1):120-8. doi: https://doi.org/10.1016/j.ijpharm.2011.06.017.

93. Carr RL. Classifying Flow Properties of Solids. Chem Eng. 1965;1:69-72.

94. Chi-Ying Wong A. Characterisation of the flowability of glass beads by bulk densities ratio. Chemical Engineering Science. 2000;55(18):3855-9. doi: https://doi.org/10.1016/S0009-2509(00)00048-8.

95. Schulze D. Powders and Bulk Solids Behavior, Characterization, Storage and Flow. 1st ed. 2008. ed. Berlin, Heidelberg: Springer Berlin Heidelberg; 2008.

96. Emery E, Oliver J, Pugsley T, Sharma J, Zhou J. Flowability of moist pharmaceutical powders. Powder Technology. 2009;189(3):409-15. doi: 10.1016/j.powtec.2008.06.017.

97. Nokhodchi A, Ford JL, Rubinstein MH. Studies on the interaction between water and (hydroxypropyl) methylcellulose. Journal of pharmaceutical sciences. 1997;86(5):608-15.

98. Campos-Aldrete ME, Villafuerte-Robles L. Influence of the viscosity grade and the particle size of HPMC on metronidazole release from matrix tablets. European journal of pharmaceutics and biopharmaceutics. 1997;43(2):173-8.

99. Goncalves-Araujo T, Rajabi-Siahboomi AR, Caraballo I. Polymer percolation threshold in HPMC extended release formulation of carbamazepine and verapamil HCl. AAPS PharmSciTech. 2010;11(2):558-62. doi: 10.1208/s12249-010-9408-x.

100. Handbook of pharmaceutical excipients. Eighth edition. ed. London: Pharmaceutical Press; 2017.

101. Sun CC. Materials Science Tetrahedron—A Useful Tool for Pharmaceutical Research and Development. Journal of Pharmaceutical Sciences. 2009;98(5):1671-87. doi: https://doi.org/10.1002/jps.21552.

102. Huoyang Lian AB, Divya Tewari, Thomas Dürig. Evaluation of Directly Compressible Hypromellose in Commercial Scale Manufactuing of a Modified Release Matrix Tablet. In: Ingredients AS, editor. AAPS Annual Meeting2017.

103. Grdešič P, Vrečer F, Ilić I. Flow and compaction properties of hypromellose: new directly compressible versus the established grades. Drug Development and Industrial Pharmacy. 2016;42(11):1877-86.

104. Van Snick B, Holman J, Cunningham C, Kumar A, Vercruysse J, De Beer T, et al. Continuous direct compression as manufacturing platform for sustained release tablets. International journal of pharmaceutics. 2017;519(1-2):390-407.

105. Schaber SD, Gerogiorgis DI, Ramachandran R, Evans JM, Barton PI, Trout BL. Economic analysis of integrated continuous and batch pharmaceutical manufacturing: a case study. Industrial & Engineering Chemistry Research. 2011;50(17):10083-92.

106. Leane M, Pitt K, Reynolds G. A proposal for a drug product Manufacturing Classification System (MCS) for oral solid dosage forms. Pharmaceutical Development and Technology. 2015;20(1):12-21. doi: 10.3109/10837450.2014.954728.

107. Qiu Y, Chen Y, Zhang GG, Yu L, Mantri RV. Developing solid oral dosage forms: pharmaceutical theory and practice: Academic press; 2016.

108. Van Snick B, Holman J, Vanhoorne V, Kumar A, De Beer T, Remon J, et al. Development of a continuous direct compression platform for low-dose drug products. International journal of pharmaceutics. 2017;529(1-2):329-46.

109. Nachaegari SK, Bansal AK. Coprocessed excipients for solid dosage forms. Pharmaceutical technology. 2004;28(1):52-65.

110. Tomar M, Sinha AR, Singh AK. Process and development of co-processed excipient silicified microcrystalline cellulose and manufacture paracetamol tablet by direct compression. Int J Pharm Sci Rev Res. 2017;42(1):191-6.

111. Wang S, Li J, Lin X, Feng Y, Kou X, Babu S, et al. Novel coprocessed excipients composed of lactose, HPMC, and PVPP for tableting and its application. International journal of pharmaceutics. 2015;486(1-2):370-9.

112. Gohel M, Jogani PD. A review of co-processed directly compressible excipients. J Pharm Pharm Sci. 2005;8(1):76-93.

113. Rojas J, Buckner I, Kumar V. Co-proccessed excipients with enhanced direct compression functionality for improved tableting performance. Drug development and industrial pharmacy. 2012;38(10):1159-70.

114. Saha S, Shahiwala AF. Multifunctional coprocessed excipients for improved tabletting performance. Expert opinion on drug delivery. 2009;6(2):197-208.

115. Engisch WE, Muzzio FJ. Loss-in-weight feeding trials case study: pharmaceutical formulation. Journal of Pharmaceutical Innovation. 2015;10(1):56-75.

116. O'Connor T, editor. FDA perspective on continuous manufacturing Journey: Past, Present, and Future. AAPS PharmSci 360; 2019; San Antonio, TX.

117. Weinekötter R, Reh L. Continuous mixing of fine particles. Particle & particle systems characterization. 1995;12(1):46-53.

118. Palmer J, Reynolds GK, Tahir F, Yadav IK, Meehan E, Holman J, et al. Mapping key process parameters to the performance of a continuous dry powder blender in a continuous direct compression system. Powder Technology. 2020;362:659-70.

119. Rescaglio A, De Smet F, Aerts L, Lumay G. Tribo-electrification of pharmaceutical powder blends. Particulate Science and Technology. 2019:1-8.

120. Šupuk E, Zarrebini A, Reddy JP, Hughes H, Leane MM, Tobyn MJ, et al. Tribo-electrification of active pharmaceutical ingredients and excipients. Powder technology. 2012;217:427-34.

121. Wong J, Kwok PCL, Chan H-K. Electrostatics in pharmaceutical solids. Chemical Engineering Science. 2015;125:225-37.

122. Mukherjee R, Gupta V, Naik S, Sarkar S, Sharma V, Peri P, et al. Effects of particle size on the triboelectrification phenomenon in pharmaceutical excipients: Experiments and multi-scale modeling. asian journal of pharmaceutical sciences. 2016;11(5):603-17.

123. Naik S, Mukherjee R, Chaudhuri B. Triboelectrification: A review of experimental and mechanistic modeling approaches with a special focus on pharmaceutical powders. International journal of pharmaceutics. 2016;510(1):375-85.

124. Ceresiat L, Grosshans H, Papalexandris MV. Powder electrification during pneumatic transport: The role of the particle properties and flow rates. Journal of Loss Prevention in the Process Industries. 2019;58:60-9.

125. Ireland PM. Triboelectrification of particulate flows on surfaces: Part I—Experiments. Powder Technology. 2010;198(2):189-98.

126. Ireland PM. Triboelectrification of particulate flows on surfaces: Part II—Mechanisms and models. Powder Technology. 2010;198(2):199-210.

127. Kaialy W. A review of factors affecting electrostatic charging of pharmaceuticals and adhesive mixtures for inhalation. International journal of pharmaceutics. 2016;503(1-2):262-76.

128. Pingali KC, Chatarla SK, Tracy BA, Byrnes BA. Sensing Electrostatic Charge Generation During Granular Flow of Pharmaceutical Powders in a Flow Tester. Journal of Pharmaceutical Innovation. 2016;11(3):179-88.

129. Watanabe H, Ghadiri M, Matsuyama T, Ding YL, Pitt KG, Maruyama H, et al. Triboelectrification of pharmaceutical powders by particle impact. International journal of pharmaceutics. 2007;334(1-2):149-55.

130. Bailey A. Electrostatic phenomena during powder handling. Powder Technology. 1984;37(1):71-85.

131. Matsusaka S, Maruyama H, Matsuyama T, Ghadiri M. Triboelectric charging of powders: A review. Chemical Engineering Science. 2010;65(22):5781-807.

132. Carter PA, Rowley G, Fletcher EJ, Stylianopoulos V. Measurement of Electrostatic Charge Decay in Pharmaceutical Powders and Polymer Materials Used in Dry Powder Inhaler Devices. Drug Development and Industrial Pharmacy. 1998;24(11):1083-8. doi: 10.3109/03639049809089953.

133. DesRosiers Lachiver E, Abatzoglou N, Cartilier L, Simard J-S. Insights into the Role of Electrostatic Forces on the Behavior of Dry Pharmaceutical Particulate Systems. Pharmaceutical Research. 2006;23(5):997-1007. doi: 10.1007/s11095-006-9934-0.

134. Peart J. Powder Electrostatics: Theory, Techniques and Applications. KONA Powder and Particle Journal. 2001;19:34-45. doi: 10.14356/kona.2001009.

135. Mäki R, Suihko E, Rost S, Heiskanen M, Murtomaa M, Lehto VP, et al. Modifying drug release and tablet properties of starch acetate tablets by dry powder agglomeration. Journal of pharmaceutical sciences. 2007;96(2):438-47.

136. Naik S, Sarkar S, Hancock B, Rowland M, Abramov Y, Yu W, et al. An experimental and numerical modeling study of tribocharging in pharmaceutical granular mixtures. Powder technology. 2016;297:211-9.

137. Staniforth J, Rees J. Electrostatic charge interactions in ordered powder mixes. Journal of Pharmacy and Pharmacology. 1982;34(2):69-76.

138. Staniforth J, Rees JE. Powder mixing by triboelectrification. Powder Technology. 1981;30(2):255-6.

139. Andreou J, Stewart P, Morton D. Short-term changes in drug agglomeration within interactive mixtures following blending. International journal of pharmaceutics. 2009;372(1-2):1-11.

140. Beeckmans J, Inculet I, Dumas G. Enhancement in segregation of a mixed powder in a fluidized bed in the presence of an electrostatic field. Powder Technology. 1979;24(2):267-9.

141. Hao T, Tukianen J, Nivorozhkin A, Landrau N. Probing pharmaceutical powder blending uniformity with electrostatic charge measurements. Powder technology. 2013;245:64-9.

142. Naik S, Sarkar S, Gupta V, Hancock BC, Abramov Y, Yu W, et al. A combined experimental and numerical approach to explore tribocharging of pharmaceutical excipients in a hopper chute assembly. International journal of pharmaceutics. 2015;491(1-2):58-68.

143. Pu Y, Mazumder M, Cooney C. Effects of electrostatic charging on pharmaceutical powder blending homogeneity. Journal of pharmaceutical sciences. 2009;98(7):2412-21.

144. Samiei L, Kelly K, Taylor L, Forbes B, Collins E, Rowland M. The influence of electrostatic properties on the punch sticking propensity of pharmaceutical blends. Powder Technology. 2017;305:509-17.

145. Nwose EN, Pei C, Wu C-Y. Modelling die filling with charged particles using DEM/CFD. Particuology. 2012;10(2):229-35. doi: https://doi.org/10.1016/j.partic.2011.11.010.

146. Ghori MU, Šupuk E, Conway BR. Tribo-electric charging and adhesion of cellulose ethers and their mixtures with flurbiprofen. European Journal of Pharmaceutical Sciences. 2014;65:1-8.

147. Ghori M, Šupuk E, Conway B. Tribo-electrification and powder adhesion studies in the development of polymeric hydrophilic drug matrices. Materials. 2015;8(4):1482-98.

148. Harwood CF, Walanski K, Luebcke E, Swanstrom C. The performance of continuous mixers for dry powders. Powder Technology. 1975;11(3):289-96.

149. Van Snick B, Holman J, Cunningham C, Kumar A, Vercruysse J, De Beer T, et al. Continuous direct compression as manufacturing platform for sustained release tablets. Int J Pharm. 2017;519(1-2):390-407. doi: 10.1016/j.ijpharm.2017.01.010.

150. Williams J. Continuous mixing of solids. A review. Powder Technology. 1976;15(2):237-43.

151. Tewari D, TITOVA YA, BEISSNER B, Durig T. Coprocessed silica coated polymer composition. ISP Investments LLC, Hercules LLC; 2019.

152. Lumay G, Boschini F, Traina K, Bontempi S, Remy J-C, Cloots R, et al. Measuring the flowing properties of powders and grains. Powder technology. 2012;224:19-27.

153. Beakawi Al-Hashemi HM, Baghabra Al-Amoudi OS. A review on the angle of repose of granular materials. Powder Technology. 2018;330:397-417. doi: 10.1016/j.powtec.2018.02.003.

154. Boschini F, Delaval V, Traina K, Vandewalle N, Lumay G. Linking flowability and granulometry of lactose powders. International journal of pharmaceutics. 2015;494(1):312-20.

155. Schella A, Herminghaus S, Schröter M. Influence of humidity on tribo-electric charging and segregation in shaken granular media. Soft Matter. 2017;13(2):394-401.

156. Berthiaux H, Marikh K, Gatumel C. Continuous mixing of powder mixtures with pharmaceutical process constraints. Chemical Engineering and Processing: Process Intensification. 2008;47(12):2315-22.

157. Engisch WE, Muzzio FJ. Feedrate deviations caused by hopper refill of loss-in-weight feeders. Powder Technology. 2015;283:389-400.

158. Bhaskar A, Singh R. Residence time distribution (RTD)-based control system for continuous pharmaceutical manufacturing process. Journal of Pharmaceutical Innovation. 2019;14(4):316-31.

159. Escotet Espinoza M. Phenomenological and residence time distribution models for unit operations in a continuous pharmaceutical manufacturing process: Rutgers University-School of Graduate Studies; 2018.

160. Gao Y, Vanarase A, Muzzio F, Ierapetritou M. Characterizing continuous powder mixing using residence time distribution. Chemical Engineering Science. 2011;66(3):417-25.

161. Karttunen A-P, Hörmann TR, De Leersnyder F, Ketolainen J, De Beer T, Hsiao W-K, et al. Measurement of residence time distributions and material tracking on three continuous manufacturing lines. International journal of pharmaceutics. 2019;563:184-97.

162. Vanarase AU, Osorio JG, Muzzio FJ. Effects of powder flow properties and shear environment on the performance of continuous mixing of pharmaceutical powders. Powder Technology. 2013;246:63-72. doi: 10.1016/j.powtec.2013.05.002.

163. Van Snick B, Kumar A, Verstraeten M, Pandelaere K, Dhondt J, Di Pretoro G, et al. Impact of material properties and process variables on the residence time distribution in twin screw feeding equipment. International journal of pharmaceutics. 2019;556:200-16.

164. Pharmacopeia US. Powder Flow. Issue 44 Number 6: The U.S. Pharmacopeial Convention; 2018.

165. Grey R, Beddow J. On the Hausner ratio and its relationship to some properties of metal powders. Powder Technology. 1969;2(6):323-6.

166. Lumay G, Pillitteri S, Marck M, Monsuur F, Pauly T, Ribeyre Q, et al. Influence of mesoporous silica on powder flow and electrostatic properties on short and long term. Journal of Drug Delivery Science and Technology. 2019;53:101192.

167. Engisch WE, Muzzio FJ. Method for characterization of loss-in-weight feeder equipment. Powder Technology. 2012;228:395-403. doi: 10.1016/j.powtec.2012.05.058.

168. Ramirez-Dorronsoro J-C, Jacko RB, Kildsig DO. Chargeability measurements of selected pharmaceutical dry powders to assess their electrostatic charge control capabilities. AAPS PharmSciTech. 2006;7(4):E133-E40.

169. Naik S, Hancock B, Abramov Y, Yu W, Rowland M, Huang Z, et al. Quantification of tribocharging of pharmaceutical powders in V-blenders: experiments, multiscale modeling, and simulations. Journal of pharmaceutical sciences. 2016;105(4):1467-77.

170. Blackshields CA, Crean AM. Continuous powder feeding for pharmaceutical solid dosage form manufacture: a short review. Pharmaceutical Development and Technology. 2018;23(6):554-60.

171. Li P. Effect of powder flow properties on the process performance of loss-in-weight feeders: Rutgers, The State University of New Jersey-New Brunswick; 2015.

172. Hanson J. Control of a system of loss-in-weight feeders for drug product continuous manufacturing. Powder Technology. 2018;331:236-43. doi: https://doi.org/10.1016/j.powtec.2018.03.027.

173. Cartwright JJ, Robertson J, D'Haene D, Burke MD, Hennenkamp JR. Twin screw wet granulation: Loss in weight feeding of a poorly flowing active pharmaceutical ingredient. Powder technology. 2013;238:116-21.

174. Santos B, Carmo F, Schlindwein W, Muirhead G, Rodrigues C, Cabral L, et al. Pharmaceutical excipients properties and screw feeder performance in continuous processing lines: a

Quality by Design (QbD) approach. Drug development and industrial pharmacy. 2018;44(12):2089-97.

175. Coetzee C. Calibration of the discrete element method. Powder Technology. 2017;310:104-42.

176. Kruggel-Emden H, Rickelt S, Wirtz S, Scherer V. A study on the validity of the multi-sphere Discrete Element Method. Powder Technology. 2008;188(2):153-65.

177. Behjani MA, Hassanpour A, Ghadiri M, Bayly A, editors. Numerical analysis of the effect of particle shape and adhesion on the segregation of powder mixtures. EPJ Web of Conferences; 2017: EDP Sciences.

178. Nye B, Kulchitsky AV, Johnson JB. Intersecting dilated convex polyhedra method for modeling complex particles in discrete element method. International journal for numerical and analytical methods in geomechanics. 2014;38(9):978-90.

179. Hogue C. Shape representation and contact detection for discrete element simulations of arbitrary geometries. Engineering Computations. 1998.

180. Garcia X, Latham J-P, XIANG J-s, Harrison J. A clustered overlapping sphere algorithm to represent real particles in discrete element modelling. Geotechnique. 2009;59(9):779-84.

181. Gravish N, Franklin SV, Hu DL, Goldman DI. Entangled granular media. Physical review letters. 2012;108(20):208001.

182. Abbaspour-Fard MH. Theoretical validation of a multi-sphere, discrete element model suitable for biomaterials handling simulation. Biosystems engineering. 2004;88(2):153-61.

183. Favier J, Fard M, Kremmer M, Raji A. Shape representation of axi-symmetrical, non-spherical particles in discrete element simulation using multi-element model particles. Engineering Computations: Int J for Computer-Aided Engineering. 1999;16(4):467-80.

184. Rougier E, Munjiza A, Latham J. Shape selection menu for grand scale discontinua systems. Engineering Computations. 2004.

185. Kulchitsky AV, Johnson JB, Reeves DM. Resistance forces during boulder extraction from an asteroid. Acta Astronautica. 2016;127:424-37.

186. Johnson JB, Duvoy PX, Kulchitsky AV, Creager C, Moore J. Analysis of Mars Exploration Rover wheel mobility processes and the limitations of classical terramechanics models using discrete element method simulations. Journal of Terramechanics. 2017;73:61-71.

187. Johnson JB, Kulchitsky AV, Duvoy P, Iagnemma K, Senatore C, Arvidson RE, et al. Discrete element method simulations of Mars Exploration Rover wheel performance. Journal of Terramechanics. 2015;62:31-40.

188. Kulchitsky AV, Hurley DM, Johnson JB, Duvoy PX, Zimmerman M. Solar wind access to grains in the upper layer of regolith. Journal of Geophysical Research: Planets. 2018;123(4):972-81.

189. Kulchitsky A, Johnson J, Wilkinson A, DeGennaro A, Duvoy P. Discrete Element Method (DEM) Application to The Cone Penetration Test Using COUPi Model. AGUFM. 2011;2011:P13D-1723.

190. Kulchitsky A, Kasper J, Johnson J, Duvoy P. Discrete Element Method Simulations of the Interactions of Woody Debris with Hydrokinetic Energy Infrastructure. AGUFM. 2016;2016:GC54B-04.

191. Johnson KL, Kendall K, Roberts a. Surface energy and the contact of elastic solids. Proceedings of the royal society of London A mathematical and physical sciences. 1971;324(1558):301-13.

192. Johnson KL, Johnson KL. Contact mechanics: Cambridge university press; 1987.

193. Boehling P, Toschkoff G, Knop K, Kleinebudde P, Just S, Funke A, et al. Analysis of large-scale tablet coating: Modeling, simulation and experiments. European Journal of Pharmaceutical Sciences. 2016;90:14-24.

194. Govender N, Wilke DN, Wu C-Y, Khinast J, Pizette P, Xu W. Hopper flow of irregularly shaped particles (non-convex polyhedra): GPU-based DEM simulation and experimental validation. Chemical Engineering Science. 2018;188:34-51.

195. Campbell CS. Rapid Granular Flows. Annual Review of Fluid Mechanics. 1990;22(1):57-90. doi: 10.1146/annurev.fl.22.010190.000421.

196. Tahir F, Palmer J, Khoo J, Holman J, Yadav IK, Reynolds G, et al. Development of feed factor prediction models for loss-in-weight powder feeders. Powder Technology. 2020;364:1025-38.

197. Simons TA, Weiler R, Strege S, Bensmann S, Schilling M, Kwade A. A ring shear tester as calibration experiment for DEM simulations in agitated mixers—a sensitivity study. Procedia engineering. 2015;102(1):741-8.

198. Roessler T, Katterfeld A. Scaling of the angle of repose test and its influence on the calibration of DEM parameters using upscaled particles. Powder technology. 2018;330:58-66.

199. Roessler T, Richter C, Katterfeld A, Will F. Development of a standard calibration procedure for the DEM parameters of cohesionless bulk materials–part I: Solving the problem of ambiguous parameter combinations. Powder Technology. 2019;343:803-12.

200. Coetzee C. Particle upscaling: Calibration and validation of the discrete element method. Powder technology. 2019;344:487-503.

201. Rackl M, Hanley KJ. A methodical calibration procedure for discrete element models. Powder technology. 2017;307:73-83.

202. Ye F, Wheeler C, Chen B, Hu J, Chen K, Chen W. Calibration and verification of DEM parameters for dynamic particle flow conditions using a backpropagation neural network. Advanced Powder Technology. 2019;30(2):292-301.

203. Johnstone MW. Calibration of DEM models for granular materials using bulk physical tests. 2010.

204. Hlosta J, Žurovec D, Rozbroj J, Ramírez-Gómez Á, Nečas J, Zegzulka J. Experimental determination of particle–particle restitution coefficient via double pendulum method. Chemical Engineering Research and Design. 2018;135:222-33.

205. WHO. Bulk density and tapped density of powders. WHO Drug Information. 2011;25(4):374-9.

206. LaPlace P. Memoires de mathematique et de physique presentés a l'Academie Royale des Sciences, par divers sçavans, et lûs dans ses assemblées. Memoires de mathematique et de physique presentés a l'Academie Royale des Sciences, par divers sçavans, et lûs dans ses assemblées. 1776.

207. Castellanos A. The relationship between attractive interparticle forces and bulk behaviour in dry and uncharged fine powders. Advances in physics. 2005;54(4):263-376.

208. Zhu H, Zhou Z, Yang R, Yu A. Discrete particle simulation of particulate systems: a review of major applications and findings. Chemical Engineering Science. 2008;63(23):5728-70.

209. Buckingham E. On physically similar systems; illustrations of the use of dimensional equations. Physical review. 1914;4(4):345.

210. Kretz D, Callau-Monje S, Hitschler M, Hien A, Raedle M, Hesser J. Discrete element method (DEM) simulation and validation of a screw feeder system. Powder Technology. 2016;287:131-8.

211. Behjani MA, Motlagh YG, Bayly AE, Hassanpour A. Assessment of blending performance of pharmaceutical powder mixtures in a continuous mixer using Discrete Element Method (DEM). Powder Technology. 2020;366:73-81.

212. Paulick M, Morgeneyer M, Kwade A. Review on the influence of elastic particle properties on DEM simulation results. Powder Technology. 2015;283:66-76.

213. Lommen S, Schott D, Lodewijks G. DEM speedup: Stiffness effects on behavior of bulk material. Particuology. 2014;12:107-12.

214. Anand A, Curtis JS, Wassgren CR, Hancock BC, Ketterhagen WR. Predicting discharge dynamics from a rectangular hopper using the discrete element method (DEM). Chemical Engineering Science. 2008;63(24):5821-30.

215. Ristow GH. Outflow rate and wall stress for two-dimensional hoppers. Physica A: Statistical Mechanics and its Applications. 1997;235(3-4):319-26.